

Charge Transfer in Organic Semiconductor Systems Probed by Photoemission Spectroscopy

DISSERTATION

zur Erlangung des akademischen Grades
Doctor rerum naturalium
(Dr. rer. nat.)

vorgelegt der
Fakultät Mathematik und Naturwissenschaften
der Technischen Universität Dresden

von
ROBERT KUHRT
geboren am 10.03.1991 in Erlangen

Dresden, 2022

Diese Dissertation wurde in der Zeit von September 2018 bis März 2022 in der Arbeitsgruppe von Prof. Martin Knupfer am Leibniz-Institut für Festkörper- und Werkstoffforschung (IFW) in Dresden angefertigt.

1. Gutachter: Prof. Dr. Bernd Büchner
2. Gutachter: Prof. Dr. Georgeta Salvan

Eingereicht am 3. März 2022

Verteidigt am 16. September 2022

Abstract

In the present work, charge transfer in organic semiconductors is investigated by means of photoemission spectroscopy. Organic charge transfer systems consist of electron donors and acceptors and in some cases exhibit new electronic properties that are not observed in the individual constituents. Examples are metallic conductivity and changed optical or transport gaps.

The main focus were interfaces between donor and acceptor molecules that were prepared as thin films by thermal evaporation in ultra-high vacuum. In particular, the strong electron acceptor F_6TCNNQ was combined with several scientifically relevant donors with the aim of achieving a large charge transfer. As reference systems, potassium doped F_6TCNNQ and the interface between F_6TCNNQ and gold were studied. In both systems, a large electron transfer to F_6TCNNQ with similar spectroscopic signatures was observed. The investigated organic interfaces all showed charge transfer that manifested itself in form of changes in the core levels of F_6TCNNQ that were similar for each system. Also, new occupied states in the former gaps of the molecules were found. For every investigated interface the Fermi energy was pinned above the respective highest occupied molecular orbitals which entails semiconducting behaviour and no metal-like delocalised charge carriers. For the combination of F_6TCNNQ and dibenzopentacene, a blended film was prepared by co-deposition and compared with the corresponding interface. It was found that the electronic properties of the blend are initially determined by electrostatic interactions, whereas annealing leads to a large charge transfer due to a temperature induced change of molecular orientation.

Moreover, the acceptors F_2TCNQ and $F_{16}CoPc$ were used in order to compare systems with the same donor and different acceptors. Differences in the degree of charge transfer and interface morphology were observed.

The last part of this work addresses the electronic properties of an organic rectifier that was fabricated by collaboration partners. It is built up of an organic heterojunction of two phtalocyanines ($CuPc$ and $F_{16}CoPc$) between two gold contacts. The energy level alignment across the device and the charge transfer reactions at the different interfaces are discussed with regard to the functionality of the device.

Zusammenfassung

Die vorliegende Arbeit beschäftigt sich mit der Untersuchung von Ladungstransfer in organischen Halbleitern mittels Photoemissionsspektroskopie. Organische Ladungstransfersysteme, die aus Elektronendonatoren und -akzeptoren bestehen, können in manchen Fällen elektronische Eigenschaften aufweisen, die sich von denen der Einzelmaterialien unterscheiden. Beispiele hierfür sind ein metallisches Leitfähigkeitsverhalten oder veränderte Energielücken.

Im Fokus lagen dabei vorwiegend Grenzflächen zwischen Donator- und Akzeptormolekülen, die durch thermisches Verdampfen als Dünnschichten im Ultrahochvakuum hergestellt wurden. Ein Großteil der Arbeit behandelt den stark elektronenziehenden Akzeptor F_6TCNNQ , der mit verschiedenen aktuell wissenschaftlich relevanten Donatoren kombiniert wurde mit dem Ziel einen möglichst großen Ladungstransfer zu erreichen. Das Ladungstransfersalz aus Kalium und F_6TCNNQ sowie die Grenzfläche zwischen Gold und F_6TCNNQ , bei denen ein großer Ladungstransfer beobachtet wurde, werden zu Beginn der Arbeit diskutiert und dienen im Folgenden als Referenzsysteme. Bei jedem der untersuchten organischen Grenzflächen zeigte sich ein Ladungstransfer in den Rumpfniveauspektren, im Fall von F_6TCNNQ in Form von ähnlichen Änderungen im Stickstoff 1s Niveau, und neuen besetzten Zuständen in der ursprünglichen Energielücke der Moleküle. Die Fermienergie wurde dabei für jedes untersuchte System deutlich oberhalb der jeweiligen höchsten besetzten Molekülorbitale gepinnt, was zur Folge hatte, dass alle untersuchten Grenzflächen halbleitend blieben und keine delokalisierten Ladungsträger aufwiesen. Zudem wurde ein Mischfilm aus F_6TCNNQ und dem Donator Dibenzopentacen durch Co-Verdampfen hergestellt und hinsichtlich des Ladungstransfers mit der entsprechenden Grenzfläche verglichen. Dabei zeigte sich, dass die elektronischen Eigenschaften des Mischfilms zunächst hauptsächlich von elektrostatischen Wechselwirkungen bestimmt wurden und das Tempern des Filmes zu einem stark ausgeprägten Ladungstransfer führte, was durch eine Umorientierung der Moleküle erklärt wird.

Auch die Akzeptoren F_2TCNQ und $F_{16}CoPc$ wurden verwendet, um Vergleiche zwischen Systemen mit gleichem Donator aber unterschiedlichen Akzeptoren zu ziehen. Dabei zeigten sich Unterschiede hinsichtlich des Ladungstransfergrades und der Morphologie der Grenzflächen.

Der letzte Teil der Arbeit beschäftigt sich mit den elektronischen Eigenschaften eines organischen Gleichrichters der von Kollaborationspartnern hergestellt wurde. Dieser besteht aus einer organischen Heterostruktur aus zwei Phtalocyaninen ($CuPc$ und $F_{16}CoPc$) zwischen zwei Goldkontakten. Der Verlauf der Energieniveaus innerhalb der Heterostruktur sowie der Ladungstransfer an den verschiedenen Grenzflächen und deren Einfluss auf die Funktion des Gleichrichters werden diskutiert.

Contents

1	Introduction	1
2	Organic Semiconductors	5
2.1	Electronic structure	5
2.2	Charge transfer	10
2.3	Interfaces involving organic semiconductors	14
2.4	Materials	21
3	Photoemission Spectroscopy	27
3.1	Theoretical background	27
3.2	Data analysis	30
3.2.1	General line shape and secondary electron background	30
3.2.2	UPS analysis	31
3.2.3	XPS analysis	33
3.3	Instrumental aspects	37
3.3.1	Energy reference	37
3.3.2	Light sources	37
3.3.3	Analyser and detector	38
3.4	Experimental setup and sample preparation	40
4	Results and discussion	45
4.1	The acceptor F ₆ TCNNQ	45
4.1.1	Potassium doping	45
4.1.2	Interface to polycrystalline gold	48
4.2	F ₆ TCNNQ based organic heterostructures	52
4.2.1	Polycyclic hydrocarbons	52
4.2.2	Ruthenium-acetylide complex	64
4.2.3	F ₆ TCNNQ/ET and F ₂ TCNNQ/ET interfaces: a comparison	73
4.2.4	Summary of F ₆ TCNNQ based interfaces	80
4.3	F ₁₆ CoPc based organic heterostructures	84
4.3.1	Interface to dibenzopentacene	84
4.3.2	Phtalocyanine heterojunction in an integrated molecular diode	87
5	Conclusion and Outlook	97
	Bibliography	99
	Publication list	111

List of Figures

2.1	Electronic configuration of carbon	6
2.2	Hybrid orbitals of carbon	6
2.3	Schematic illustration and energy level diagram of molecular orbital formation	7
2.4	Scheme of electronic structure of an isolated molecule and molecules in a solid.	8
2.5	Optical gaps of acenes in dependence of number of benzene rings	9
2.6	Frontier orbitals in dependence of fluorination for copper phtalicyanines . .	10
2.7	Two scenarios for charge transfer	11
2.8	Frontier orbital shifts due to polaron formation	12
2.9	Energy level diagram of organic semiconductor/metal interface considering only van-der-Waals interactions	15
2.10	Energy level diagram of organic semiconductor/metal interface considering charge transfer	16
2.11	Dependence of hole and electron injection barriers on substrate work function	17
2.12	Energy level diagram of organic/organic interface with charge transfer . . .	19
2.13	Structure of Buckminster fullerene C_{60}	25
3.1	Energy levels and photoelectron spectra of a solid	28
3.2	"Universal curve" of mean free path of electrons in dependence of kinetic energy	29
3.3	Background correction of an Au4f XPS spectrum	32
3.4	UPS spectrum of a C_{60} film evaporated on a gold foil	33
3.5	Satellite correction of a UPS spectrum of C_{60}	34
3.6	Examples for chemical shift of core level spectra	35
3.7	Scheme of final state effects in photoemission	36
3.8	Relevant energies of a sample in contact with a spectrometer	38
3.9	Determination of experimental resolution	39
3.10	Scheme of the SPECS spectrometer setup	41
4.1	XPS spectra of pristine and potassium doped F_6TCNNQ	46
4.2	UPS spectra of prisitne and potassium doped F_6TCNNQ	47
4.3	XPS spectra of F_6TCNNQ /gold interface	48
4.4	UPS spectra and work functions of F_6TCNNQ /gold interface	50
4.5	Energy level alignment at the F_6TCNNQ /gold interface	51
4.6	C1s spectra of F_6TCNNQ /polycyclic hydrocarbons interfaces	53
4.7	F1s spectra of F_6TCNNQ /polycyclic hydrocarbons interfaces	55
4.8	Qualitative analysis of C1s spectra of F_6TCNNQ /polycyclic hydrocarbons interfaces	56
4.9	Comparison of C1s spectra of F_6TCNNQ in pristine form and at interfaces to polycyclic hydrocarbons	56

4.10	N1s spectra of F ₆ TCNNQ/polycyclic hydrocarbons interfaces	57
4.11	UPS spectra of F ₆ TCNNQ/polycyclic hydrocarbons interfaces	58
4.12	XPS spectra of pristine materials and blend of F ₆ TCNNQ and dibenzopentacene	61
4.13	UPS spectra of pristine materials and blend of F ₆ TCNNQ and dibenzopentacene	62
4.14	UPS spectra of blend of F ₆ TCNNQ and dibenzopentacene before and after annealing	63
4.15	Molecular structure of Ru-complex from XRD	64
4.16	Optical absorption of Ru-complex as thin film and in solution	65
4.17	XPS spectra of pristine Ru-complex	66
4.18	Energy level diagram of Ru-complex	66
4.19	Ru3d _{5/2} spectra of Ru-complex/F ₆ TCNNQ interface	67
4.20	P2p and S2p spectra of Ru-complex deposited stepwise on F ₆ TCNNQ	68
4.21	N1s spectra of F ₆ TCNNQ/Ru-complex interface	69
4.22	Optical absorption spectra of Ru-complex, F ₆ TCNNQ and a mixture of both in solution	70
4.23	UPS spectra of F ₆ TCNNQ/Ru-complex interfaces	70
4.24	UPS spectra of F ₆ TCNNQ/Ru-complex interface with subtraction of Ru-complex spectrum	71
4.25	N1s spectra of F ₆ TCNNQ/ET and F ₂ TCNQ/ET interfaces	73
4.26	S2p spectra of thin layers of ET on F ₆ TCNNQ and F ₂ TCNQ	74
4.27	S2p spectra of ET/F ₆ TCNNQ and ET/F ₂ TCNQ interfaces	75
4.28	UPS spectra of F ₆ TCNNQ/ET and F ₂ TCNQ/ET interfaces	77
4.29	UPS spectra of Et/F ₆ TCNNQ and ET/F ₂ TCNQ interfaces	78
4.30	Work function evolution at F ₆ TCNNQ/ET and F ₂ TCNQ/ET interfaces and opposite sequences	79
4.31	Comparison of N1s core level spectra of F ₆ TCNNQ at different organic donors	80
4.32	Comparison of work function progression of F ₆ TCNNQ at different organic donors	81
4.33	Comparison of energy level alignment of F ₆ TCNNQ at different organic donors	82
4.34	C1s, N1s and F1s spectra of F ₁₆ CoPc/dibenzopentacene interface	85
4.35	Co2p _{3/2} and UPS spectra of F ₁₆ CoPc/dibenzopentacene interface	86
4.36	Overview of rectifier device setup and fabrication	89
4.37	Co2p _{3/2} and Cu2p _{3/2} spectra of CuPc/F ₁₆ CoPc interface	90
4.38	UPS spectra and work function progression of CuPc/F ₁₆ CoPc interface	91
4.39	I-V curves of organic rectifiers	93
4.40	Photoemission spectra of mimicked top electrode of organic rectifier	94

List of Tables

2.1	Overview of used molecular acceptors	21
2.2	Overview of used molecular donors	22
3.1	Satellite excitations of He gas discharge lamps	33
3.2	Area ratios of spin orbit split doublets	35
3.3	Evaporation temperatures and pressures of used organic materials	42
4.1	Energy differences and area ratios of different N1s and S2p components at ET/F ₆ TCNNQ and ET/F ₂ TCNQ interfaces	76

1 Introduction

Humans today are surrounded by semiconductor devices in their daily lives. They are present in computers, consumer electronics, cars, industrial production and many more areas. The most used semiconductor materials are inorganic ones, such as silicon, germanium and gallium arsenide. However, in the last three decades another class of semiconductors built up of organic molecules has been gaining increasing scientific and technological attention. In some areas, these organic semiconductors have already entered the market, most prominently in organic light-emitting diodes (OLEDs) in display applications of different kinds.

While first investigations of fluorescence and conductivity of organic solids were performed at the beginning of the 20th century [1, 2], the term "organic semiconductor" first emerged in the 1950s after systematic studies of Hiroo Inokuchi [3] and others. Another important milestone in the field was the discovery of conducting polymers in the 1970s [4], for which Heeger, MacDiarmid and Shirakawa received the nobel price in chemistry in 2000. The first application of organic semiconductors in a photovoltaic cell (OPVC) and an OLED was achieved by Ching Wan Tang and Steven Van Slyke at the Eastman Kodak Company in the mid 1980s [5, 6] and at the same time, the first organic field-effect transistor (OFET) was fabricated by Tsumura et al. [7]. These successes marked the beginning to large scientific and technological efforts which led to first commercially available OLED devices in the late 1990s. Today, the OLED market is worth tens of billions of dollars with increasing tendency [8]. While organic semiconductors have advantageous properties that make them suitable to replace or complement inorganic semiconductors in some areas, they also exhibit problems that have prevented the large-scale fabrication of competitive OFETs and OPVC's so far.

Organic materials are lighter than inorganic semiconductors and can be deposited on plastic substrates, which enables new applications such as flexible displays, biocompatible electronics or OPVCs on foils that could possibly be incorporated into roofing materials. Moreover, due to the low melting point ($<500\text{ }^{\circ}\text{C}$) of organic materials, their processing by thermal evaporation requires less energy than fabricating inorganic semiconductor crystals. New solution processing methods such as ink-jet printing could further lower costs and energy consumption in the future. Another advantage is the ability to modify electronic and photophysical properties of molecules by means of organic chemistry. However, there are also significant disadvantages. Devices made of organic semiconductors often have shorter lifetimes than their inorganic counterparts because of degradation due to heat, UV-radiation and exposure to oxygen and moisture. The main drawback, though, is the low carrier mobility (typically about 1 vs. $1000\text{ cm}^2\text{ V}^{-1}\text{ s}^{-1}$) which (so far) prevents applications that require high-frequency operation. The reason for this is that organic semiconductors are built up of molecules held together by weak van-der-Waals forces instead of covalently bound atoms. This entails a small orbital overlap and hence a charge transport by hopping between localised states rather than a band charge transport.

Similar as in conventional semiconductors, conductivity and Fermi level position of organic semiconductors can be influenced by a controlled introduction of electrons or holes into initially unoccupied states (doping) [9–12]. This is achieved by the addition of molecules with electron withdrawing (acceptors) or electron donating (donors) character. Charge is then either removed from the highest occupied molecular orbital (HOMO) or added to the lowest unoccupied molecular orbital (LUMO) of the organic semiconductor, leading to an increase of hole or electron concentration and a shift of the Fermi level.

Beyond that, there are other routes of using charge transfer to change the electronic properties of organic materials. Instead of mixing a small amount of molecular dopants into the host material, combining donor and acceptor molecules in a stoichiometric ratio can lead to the formation of so called charge transfer complexes. These binary crystals sometimes exhibit entirely new properties that are not present in their individual constituents, such as metal-like transport behaviour or even highly correlated states such as superconductivity or Mott-insulation [13, 14]. These characteristics however, are strongly anisotropic and depend on the arrangement of donors and acceptors which is mostly in separate or mixed stacks. The interplay between the degree of charge transfer and the molecular arrangement that leads to these phenomena is not clear [13].

Besides binary crystals, also interfaces between donors and acceptors are reported to show metal-like conductivity [15–19], which suggests analogies to the formation of 2-dimensional electron gases at inorganic semiconductor interfaces [20]. An improved understanding of the underlying mechanisms and the fabrication of such charge transfer interfaces could lead to interesting new applications, for example in OFETs or as electrodes in purely organic devices.

The purpose of this work is the investigation of various donor-acceptor systems with regard to a possible charge transfer and its effects on the materials' electronic properties. The predominantly used method is photoemission spectroscopy, which allows the measurement of occupied states in both the valence region and the core levels. The investigated systems include donor-acceptor interfaces and blends in form of thermally evaporated thin films. Particular emphasis was on the study of the molecular acceptor F_6TCNNQ which exhibits one of the highest known electron affinities and therefore promises a high charge transfer potential.

The thesis is started with an introduction to the topic of organic semiconductors and to organic charge transfer systems. The primarily used method photoemission spectroscopy is then addressed in particular with regard to probing charge transfer between organic molecules. This is followed by the results which are divided into three parts.

In the first part, a film of F_6TCNNQ was intercalated with potassium with the aim of creating a charge transfer complex where F_6TCNNQ is completely reduced. This is intended to serve as a reference system to the other F_6TCNNQ containing systems. Also, the interface between F_6TCNNQ and polycrystalline gold, which was mostly used as substrate throughout this work, was investigated.

In the second part, various donor type molecules were paired with F_6TCNNQ to study the charge transfer reactions at interfaces and in mixed films. The donors were chosen due to their relevance in different areas of potential application: Pentacene and dibenzopentacene as prototypical aromatic hydrocarbons that are candidates for an application in OFETs, a ruthenium acetylide complex as a potential building block of a functional polymer and BEDT-TTF, an organosulfur molecule which gained a lot of interest as a

cation for superconducting charge transfer salts.

The third part is dedicated to $F_{16}CoPc$, another acceptor which was investigated in the past and showed reliable charge transfer ability and processing stability. First, its charge transfer characteristics at an interface to dibenzopentacene are explored. Lastly, the electronic structure of a rectifier diode, based on an organic heterojunction between two gold electrodes is discussed with regards to its different interfaces. The thesis is concluded with a summary of the findings obtained in this work and an outlook for potential future research.

2 Organic Semiconductors

Organic semiconductors are materials that are built up of molecules that contain predominantly carbon and hydrogen. They display physical properties that are associated with semiconducting materials, such as an optical gap of 1.5 to 3 eV and a conductivity that enables an application in devices such as light emitting diodes (LEDs), photovoltaic cells and field-effect-transistors. Despite these similarities, organic semiconductors and their inorganic counterparts differ significantly from each other regarding the physical mechanisms that lead to their semiconducting behaviour.

In this chapter, an introduction to the electronic properties of organic semiconductors will be given. This is followed by an overview of the different aspects of charge transfer between organic semiconductors. Finally the materials that were investigated as part of this thesis are introduced.

2.1 Electronic structure

Molecular orbitals

The origin of the semiconducting electronic properties of certain molecules lies in the bonding behaviour of carbon atoms. Carbon in its ground state has an electron configuration of $1s^2 2s^2 2p^2$. In an excited state, one of the electrons in the 2s shell is transferred to the 2p shell resulting in a configuration of $1s^2 2s^1 2p^3$ with four unpaired valence electrons. When forming a bond to another atom, a mixing of the 2s orbital with one, two or three 2p orbitals occurs. This combination of orbitals is called hybridisation and the resulting hybrid orbitals are referred to as sp, sp^2 and sp^3 orbitals. The superscript number denotes the number of orbitals taking part in the hybridisation, thus the 2s and 2p electrons can form two sp, three sp^2 or four sp^3 hybrid orbitals (see Fig. 2.1). The sp hybrid orbitals form an angle of 180° between them, the sp^2 orbitals lie in a plane separated by equal angles of 120° and the sp^3 orbitals form a tetrahedron with an angle of 109.5° measured from the centre (see Fig. 2.2).

When multiple carbon atoms form a molecule, two or more atomic orbitals combine to molecular orbitals. The first approximation for calculating molecular orbitals was published by John Lennard-Jones in 1929 as the linear combination of atomic orbitals (LCAO) method [21]. If one considers two atomic orbitals ϕ_a and ϕ_b , the resulting molecular orbitals can be expressed by the linear combinations: $\Psi_+ = c_1\phi_a + c_2\phi_b$ and $\Psi_- = c_1\phi_a - c_2\phi_b$ with c_1 and c_2 being positive numbers. Ψ_+ can be interpreted as constructive interference of the two electron wave functions leading to an enhanced charge density between the atomic nuclei, which results in a bonding character of the orbital. Ψ_- on the other hand represents destructive interference leading to an anti-bonding molecular orbital because the reduced electron density between the nuclei leads to a diminished screening of the nuclei's repulsion. Two different types of molecular

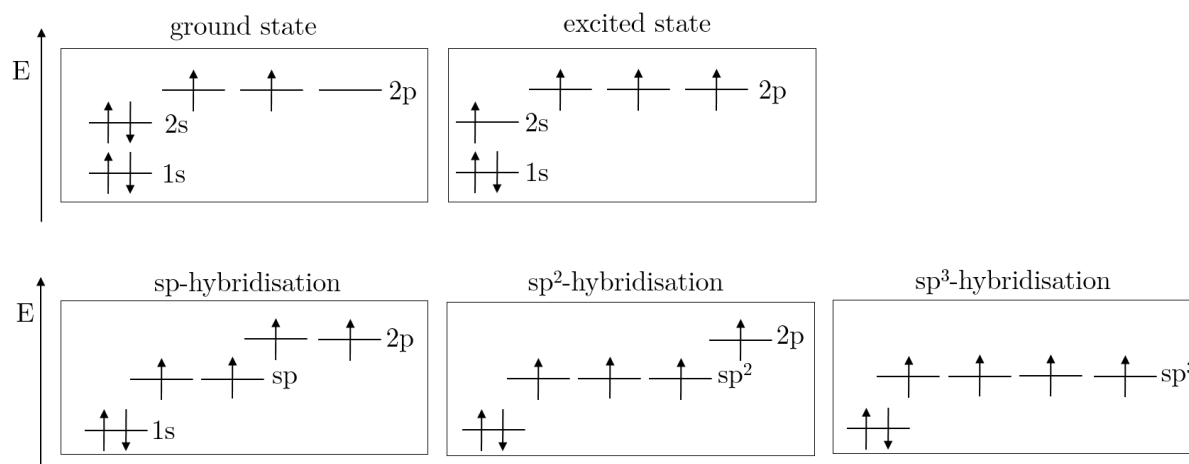


Figure 2.1: Schematic representation of the electronic configuration of carbon in its ground state, excited state and hybridised states.

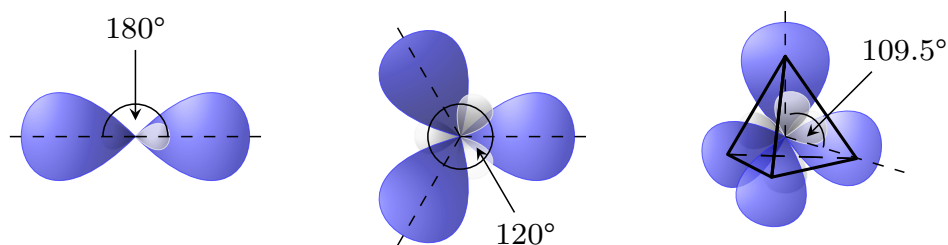


Figure 2.2: Hybrid orbitals of carbon. left: sp hybrids at an angle of 180° from each other centre: sp^2 hybrids in xy -plane with 109° between them and right: sp^3 hybrids that span a tetrahedron with an angle of 109.5° .

orbitals can be distinguished: σ -orbitals are formed by combining two s , one s and one p , two p or two hybridised orbitals and exhibit a charge distribution that is rotationally symmetric around the bond axis between the two respective atoms. π -orbitals instead, are formed by the overlapping of two non-hybridised p or d orbitals that stand vertically on the molecular axis. In first approximation, the binding strength (binding energy) and the splitting of bonding and anti-bonding orbitals depend on the overlap of the partaking atomic orbitals. Consequently, the σ -orbitals reside at a higher binding energy, mainly responsible for holding the molecule together, with a splitting of bonding σ and anti-bonding σ^* well beyond the visible spectrum ($>5\text{eV}$). The semiconducting properties of organic semiconductors are based on the π -orbitals that constitute the highest lying molecular orbitals with a π - π^* splitting within the visible range ($<3\text{eV}$). The formation of π - and σ -orbitals is depicted in Fig. 2.3.

In general, the highest molecular orbital that contains electrons is referred to "highest occupied molecular orbitals" or HOMO. The next higher orbital is called "lowest unoccupied molecular orbital", LUMO. Position and energetic difference of these so called frontier orbitals mainly determine the optical and electronic properties of the molecule. In order for a molecular solid to have semiconducting properties, i.e. an optical gap in the visible range and the possibility of charge injection from metal electrodes, the HOMO

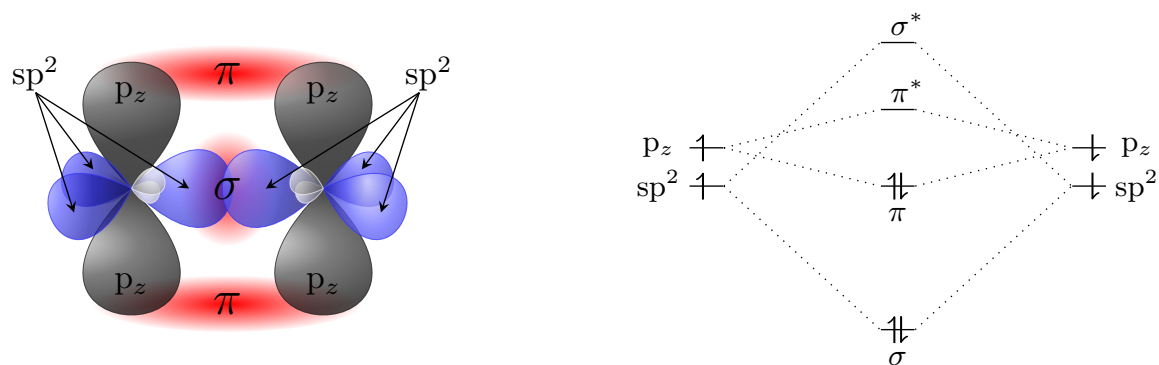


Figure 2.3: Left: Schematic representation of covalent double bond of two sp^2 hybridised carbon atoms. σ -bond forms along the bond axis by combining two sp^2 hybrid orbitals, π -bond forms by combining two p_z -orbitals. Right: energy level diagram of molecular orbital formation in the case of ethene. σ (π) denotes bonding, σ^* (π^*) anti-bonding linear combination. Due to higher overlap of involved atomic orbitals, σ - σ^* splitting larger compared to π - π^* splitting.

and LUMO should be formed by π and π^* orbitals.

When several carbon atoms form a molecule with alternating double and single bonds, typically in form of connected benzene rings, this constitutes a so called conjugated system. These systems can be described by a more than one electron structure formula (Lewis structure [22]), because the order of single and double bonds is commutable. This phenomenon is called mesomerism and manifests itself for example in X-ray diffraction experiments that showed that benzene comprises of equally bonds of equal length (139 pm) instead of the expected alternation of single (147 pm) and double (135 pm) bonds. This effect is explained by a delocalisation of the π electron system resulting in a probability density for the six valence electrons that is spread out above and below the molecular plane. In molecules with $4n+1$ π -electrons, with n being an integer number, the structure of the molecule is stabilised which is described by the term aromaticity.

From molecule to solid

An inorganic semiconductor consists of covalently bound atoms that form collective energy bands due to the interaction of the periodic potential of the ions with the wave functions of the electrons. By contrast, when organic molecules condensate to form a molecular solid, they are bound together by the relatively weak van-der-Waals forces that result from dipole interactions due to charge fluctuations in neighbouring (neutral) molecules. This results in a larger distance between the molecules and a weaker interaction between the respective π -orbitals. Hence, electronic bands are only observed in well ordered organic single crystals at low temperatures. In all other systems, charge carriers are rather localised at their respective molecules and the electronic transport can be described by hopping models [23].

Fig. 2.4 shows schematically the formation of a solid from isolated molecules [24]. The potential landscape of an isolated molecule (Fig. 2.4, left) is built up from the coulomb potential wells of the atomic nuclei that combine to an effective potential for the electrons. The vacuum level (E_V) refers to the energy of an electron at rest outside of the

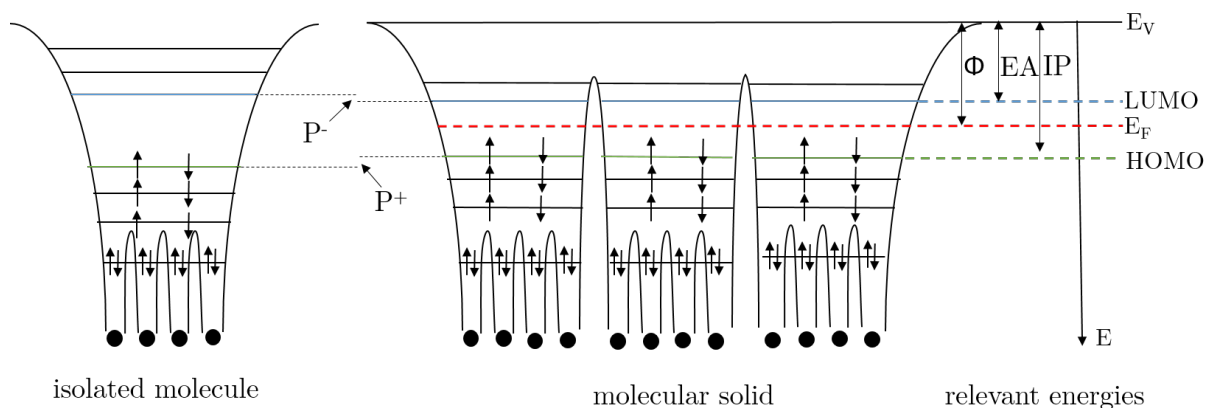


Figure 2.4: left: Electronic structure of an isolated molecule. Nuclei (shown as black circles) induce potential wells in which the electrons in deep lying atomic orbitals are localised. Atomic orbitals closer to the vacuum level are merged to molecular orbitals that are delocalised over the molecule. middle: Electronic structure of molecular solid without band formation (not monocrystalline). Potential wells join but HOMO and LUMO are usually still localised on each molecule. HOMO-LUMO gap is reduced due to polarisation of neighbouring molecules. right: relevant energies that govern electronic processes in organic semiconductors: E_V : vacuum energy, EA: electron affinity, IE: ionisation potential, $P^{+(-)}$: polarisation energy for holes (electrons). Adapted from [24].

solid [25]. The deep lying atomic orbitals are localised near the nuclei while the orbitals closer to E_V delocalise across the molecule (π -orbitals). When molecules condensate to form a solid state, the potential wells join and a Fermi E_F in the middle of the HOMO-LUMO gap can be defined, where the occupation probability is 0.5, in analogy to an inorganic semiconductor. In Fig. 2.4, E_F is placed in the middle of the gap as it is the case for an intrinsic (organic) semiconductor, this might not be the case at interfaces or in doped systems. The energy of E_F with respect to E_V is defined as the work function Φ . The energetic difference between LUMO and E_V is named electron affinity (EA) and the difference between HOMO and E_V ionisation potential (IP). In a molecular solid, the electrons in HOMO and LUMO are still localised on their respective molecules due to the weak intermolecular interaction. However, the HOMO-LUMO gap is decreased compared to a molecule in the gas phase by the polarisation energy (P^- for electrons and P^+ for holes). This effect can be rationalised by considering the ionisation of a molecule in a solid. The surrounding molecules get polarised and thereby screen the additional charge, which leads to a decrease of the ionisation potential and an increase of the electron affinity compared to a single molecule in the gas phase [26]. The magnitude of the polarisation energy depends on the polarisability and the spatial orientation of the molecules in the solid and can be as high as 2 eV [27]. It has been shown recently, that long-range electrostatic interactions that strongly depend on the molecule's quadrupol moments have a large influence on the EA and IP of organic semiconductor films [28–30]. This can be utilised to tune the energetic position of the frontier orbitals in blended films of two different organic semiconductor by varying the mixing ratio of the two constituents [28, 31]

Besides the virtual absence of an electronic band structure for most systems, another

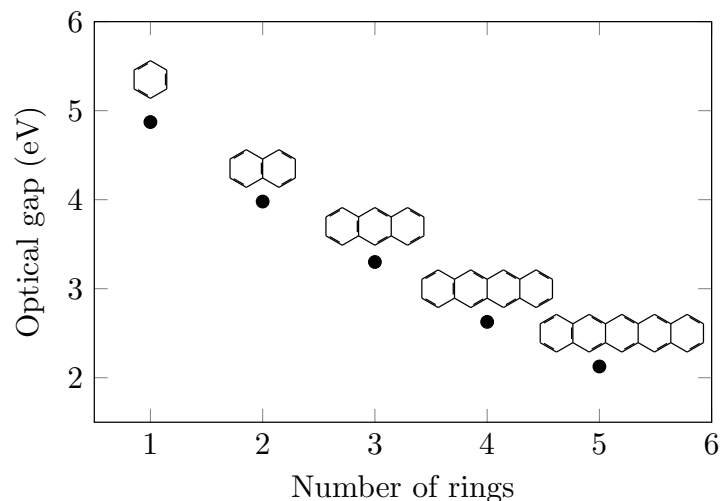


Figure 2.5: Optical gap of several members of the acene family in dependence of the number of benzene rings. Increasing the size of the π -system decreases the gap. Data taken from [34].

important difference to inorganic semiconductors concerns the character of electronic excitations. When an electron in an inorganic semiconductor is excited from the valence band to the conduction band, a hole is created in the valence band. This electron hole pair can be described as a quasi particle named exciton. Due to the large dielectric constant of inorganic semiconductors (typically in the order of 10), the two charges are screened from each other by charge carriers in the vicinity, which leads to a small exciton binding energy (in the order of 0.1 to 10 meV). By contrast, organic semiconductors have small dielectric constants (around 4), yielding exciton binding energies of 0.1 to 1 eV [32]. When electron and hole are to be completely separated, e.g. in a photovoltaic cell, the exciton binding energy needs to be invested in addition to the energy required for promoting the electron from the HOMO to the LUMO. Thus, in the case of organic semiconductors, it is differentiated between the optical gap, which is the energy required to promote an electron from the HOMO to the LUMO and the transport gap which includes also the separation of the excited electron from the created hole.

The energetic positions of HOMO and LUMO play a crucial role for optical and electronic processes in organic semiconductors. Molecular design by means of organic chemistry offers the possibility to tailor the electronic structure of molecules towards application-specific demands. For example, increasing the size of the π -system leads to a decrease of the π - π^* splitting resulting in a smaller gap. Fig. 2.5 shows the optical gap for some molecules of the acene class that consist of linearly fused benzene rings. Another route to modifying the electronic properties is the addition of functional groups with electron donating or withdrawing character [33]. For example, attaching fluorine atoms to a molecule leads to a lowering of the HOMO and LUMO energies and consequently increasing EA and IP. Fig. 2.6 shows this effect for the example of copper phthalocyanines (CuPc) and two of its fluorinated derivatives.

The next section outlines how the electronic properties of organic semiconductors can be manipulated by the use of charge transfer.

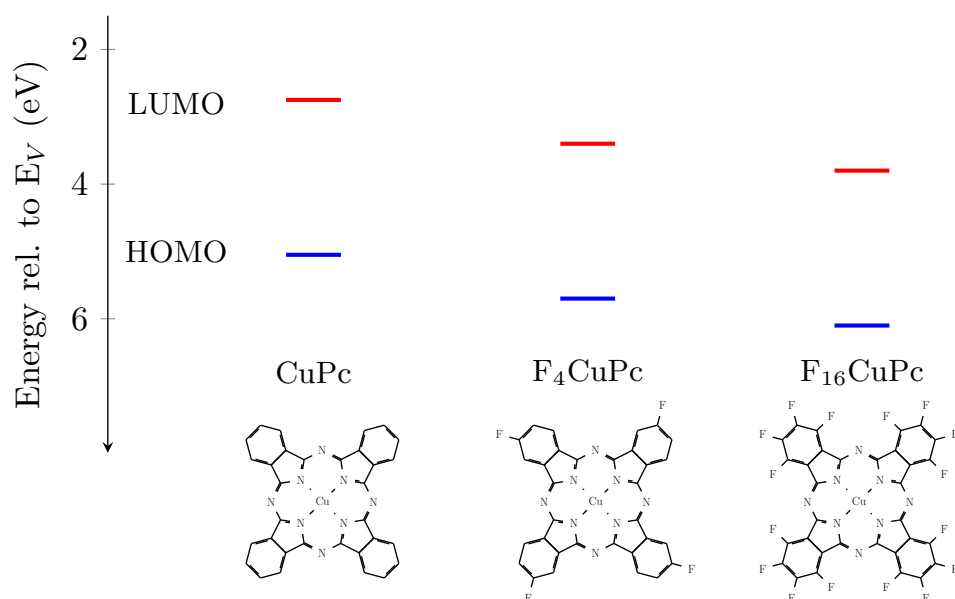


Figure 2.6: Energies of HOMO and LUMO of copper phthalocyanine (CuPc) and its fluorinated derivatives $F_4\text{CuPc}$ and $F_{16}\text{CuPc}$. Increasing fluorination leads to a shift to higher energies relative to the vacuum level, while the HOMO-LUMO gap remains virtually unchanged. Data taken from [35].

2.2 Charge transfer

In the field of organic semiconductors, charge transfer is utilised for altering the electronic properties with regard to the desired application. The underlying mechanisms of charge transfer are discussed in this section, followed by an introduction of the most important charge transfer based applications and material classes.

A ground state charge transfer from one molecule (donor) to another (acceptor) can be described by the reaction



with the donor D, the acceptor A and the degree of charge transfer $\delta \leq 1$. The term ground state charge transfer refers to the fact that the charge transfer occurs just by placing donor and acceptor close to each other without prior excitation by light or charge injection. Generally, two mechanisms can be distinguished that are depicted in Fig. 2.7: Ion pair (IPA) formation and charge transfer complex (CPX) formation. In order for IPA formation to occur, the frontier orbitals of donor and acceptor need to fulfil the condition

$$IP_{\text{donor}} < EA_{\text{acceptor}}. \quad (2.2)$$

In this process, one electron is transferred from the HOMO of the donor to the LUMO of the acceptor, corresponding to a degree of charge transfer $\delta=1$. This so called integer charge transfer leaves behind an ion pair, the donor cation and the acceptor anion just as in ordinary salts. For CPX formation on the other hand, condition 2.2 does not have to be fulfilled and δ can be smaller than one. In this scenario, the HOMO of the donor and the LUMO of the acceptor hybridise to form a supra-molecular complex with a new set

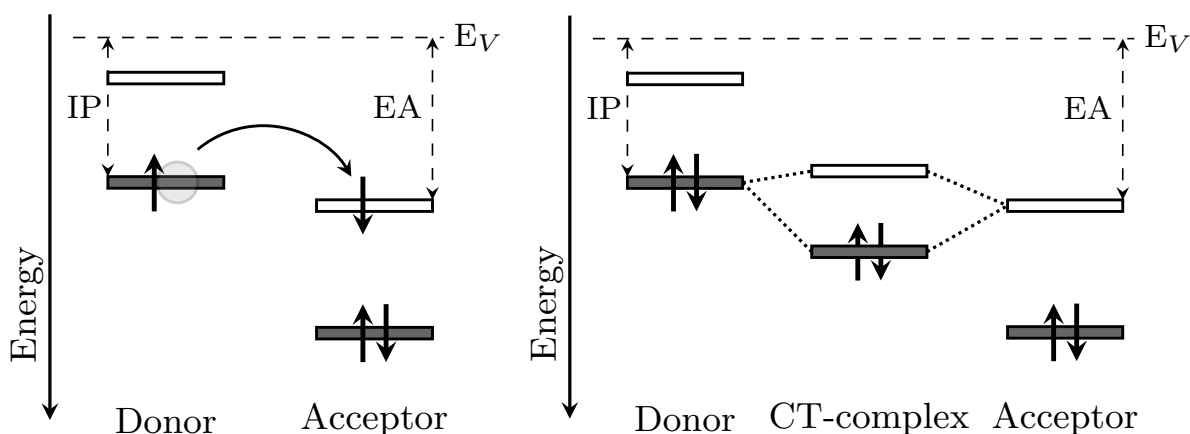


Figure 2.7: Two scenarios for charge transfer between donor and acceptor. Left: Ion pair formation where an electron is transferred from the HOMO of the donor to the LUMO of the acceptor. Right: Ground state charge transfer complex formation due to hybridisation of the donor HOMO and the acceptor LUMO.

of frontier orbitals. It is not trivial to predict which of the two mechanisms will occur for a given donor-acceptor combination, because apart from the position of the respective frontier orbitals, also the spatial orientation and distance of the two molecules as well as the overlap of the π orbital wave functions determine the charge transfer reaction. These factors and the great variety of organic molecules make the systematic investigation of charge transfer systems a very complex task.

When an additional charge is placed on a neutral molecule, it changes its geometry (bond lengths, angles) as well as the energies of its frontier orbitals. This additional charge together with the molecule deformation is often referred to as positive or negative polaron, a quasiparticle concept known from inorganic solid state physics, describing the lattice deformations caused by positive or negative charges in a crystal [36]. In the case of (often amorphous) molecular films, the term "polaronic effect" describes the additional charge in combination with a distortion of the molecule itself, dismissing the idea of a moving lattice distortion [37]. In the standard polaron model [38], which still has been used recently [39], positive ionisation leads to a half filled HOMO which is shifted upwards in energy compared to its initial position due to the geometric distortion of the molecule and the LUMO is shifted downwards symmetrically. These two polaronic states of which the lower is partially occupied give rise to the shift of the Fermi level upon doping. Recently, a revised polaron model has been proposed [11, 40–42], which is shown schematically in Fig. 2.8. In this model, the on-site Coulomb interaction, often called Hubbard U in literature, is taken into account. This interaction leads to a splitting of the former LUMO (for negative polarons) or the former HOMO (for positive polarons) into two levels ($EA^{-(+)}$ and $IP^{-(+)}$ in Fig. 2.8) of which the lower one is singly occupied. This on-site interaction can be rationalised by considering the addition of a second electron from the vacuum level to an already singly reduced molecule. The energy gained in this process is smaller than IP^- because of the Coulomb repulsion between the two electrons [41].

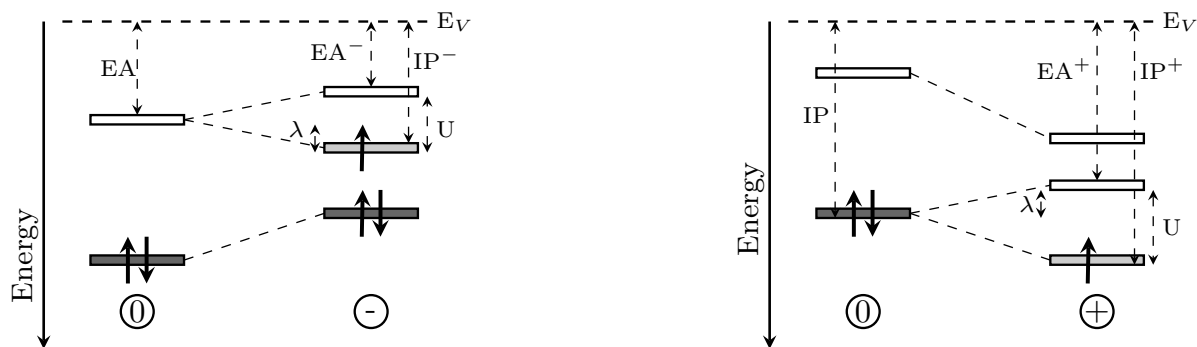


Figure 2.8: Left: change of frontier orbital energies of an organic semiconductor upon reduction which leads to a negative polaron on the molecule. The reorganisation energy λ denotes the difference between the electron affinity before charge transfer EA and the ionisation potential after charge transfer IP^- . On site Coulomb energy U causes splitting of LUMO derived sublevels IP^- and EA^- . Right: same scheme for positive polaron. Inspired by [40].

One very common application of charge transfer is the controlled doping of organic semiconductor films. Based on some recently published review articles about this topic [9–12], an introduction to this subject will be given in the following. The aim of doping semiconductors is to increase the intrinsically low concentration of free charge carriers and thereby alter the position of the Fermi level and increase the materials conductivity. In inorganic semiconductors, impurity atoms with a valence that is higher (n-doping) or lower (p-doping) than the valence of the semiconductor are incorporated into the crystal lattice. These dopant atoms bond covalently to the semiconductor, creating additional charge carriers. By combining layers of different doping regimes, complex semiconductor devices can be realised. For organic semiconductors, the idea is similar, but the mechanism is different. Electron donors or acceptors are added that donate electrons to the LUMO or extract electrons from the HOMO of the molecules in the organic semiconductor host matrix. The first materials that were used as dopants were strongly oxidising gases like iodine or bromine [43, 44]. More recently, alkali metal atoms [45, 46] as well as small molecules like Lewis acids were used [47]. However, since these dopants are relatively small in size and not covalently bound to the host material, they tend to diffuse into the organic matrix which complicates the manufacturing of stable doped films and devices. This problem is avoided by the use of larger, more stable molecular dopants, that are co-evaporated with the host material. The implementation of molecular doping enables the reduction of ohmic losses in transport layers and the lowering of the injection barriers at interfaces to electrodes which has led to the fabrication of more efficient OLED's and organic photovoltaic cells in the recent years. Despite this progress, the doping efficiency in molecularly doped organic semiconductors is much lower than in their inorganic counterparts, which requires dopant concentrations in the order of percent. The reason for this is still under scientific debate.

In most models, the doping process is described in two steps. First, an electron or hole is (completely or partially) transferred from the dopant to a host molecule, resulting in the formation of an IPA or a CPX. In the second step, the IPA or CPX need to be dissociated in order to generate a free charge carrier. It is mostly believed that a CPX formation

is not desired because the the energy difference between the occupied hybridised state and the transport state of the host material can be significant and thereby reduce the doping efficiency [48]. But even when IPA formation is considered, the low dielectric constant of organic semiconductors leads to a significant Coulomb binding energy of 10 to 20 times the thermal energy $k_B T$ at room temperature between charge carrier and parental dopant. The mechanism responsible for subsequent charge carrier release is still under debate, several studies argue that the binding energy is lowered at higher dopant concentrations by energetic disorder induced by neighbouring dopant molecules [49–51].

Another class of charge transfer based materials are the organic charge transfer salts [13, 52–54]. This term refers to donor-acceptor complexes that form due to integer or partial charge transfer. Unlike doped organic semiconductors that consist of a (often amorphous) host matrix mixed with a dopant in concentrations of maximal 10%, these materials are made up of donors and acceptors in stoichiometric composition that form binary crystals. The most famous and most extensively studied charge transfer salt is TTF-TCNQ which was discovered in 1973 [55]. TTF-TCNQ is often called an "organic metal" because it exhibits metal like conductivity of $1 \cdot 10^4 \Omega \text{ cm}^{-1}$ down to 54 K where the conductivity drops to $500 \Omega \text{ cm}^{-1}$. This property stems from the crystal structure that consists of separate stacks of electron donating tetrathiafulvalene (TTF) and electron accepting tetracyanoquinodimethane (TCNQ) molecules with a degree of charge transfer of $\delta=0.59$ [56]. As a result, the HOMOs of TTF form a valence band and the LUMOs of TCNQ form a conduction band, both of which are partially filled due to the charge transfer and contribute to the metallic conductivity. This high conductivity is highly anisotropic, only occurring parallel to the stacks of the respective molecules. Below 54 K, the molecular chains exhibit a Peierls distortion [57] which leads to a localisation of the electrons and thus to an insulating phase.

Based on the same principle of separately arranged stacks or layers of anions and cations, more charge transfer compounds with interesting properties were discovered in the following years. One remarkable material class are the so called Bechgaard salts, the first organic superconductors, discovered in the 1980's, with transition temperatures around 1 K [58]. This was followed by the finding of quasi two-dimensional charge transfer compounds based on the donor type molecule bisethylenedithio-tetrathiafulvalene (BEDT-TTF or ET). More than 50 members of this material class were found to show superconductivity, the highest critical temperature achieved was 11.5 K for κ -(ET)₂Cu[N(CN)₂]Cl [59]. Worth mentioning are also the group of alkali metal intercalated fullerenes, some of which also showing superconductivity up to temperatures of 18 K (K₃C₆₀ [60]) and 38 K (Cs₃C₆₀ [61]).

While it was believed that these interesting properties of enhanced conductivity and superconductivity only occur in binary crystals, a report of Alves et al. [15] caused interest in another class of charge transfer systems. This study reported metallic conduction at the interface of a TTF and a TCNQ single crystal that were laminated onto each other. Other than in TTF-TCNQ binary crystals, no drop in conductivity due to a Peierls transition was measured, which suggests that the mechanism accounting for the metallic conductivity is different. Charge transfer driven properties that significantly differ from those of the individual constituting semiconductors were also found for other

donor-acceptor interfaces [16–19]. All of these systems consist of at least one single crystal component. The purpose of this work is to investigate donor-acceptor interfaces of vacuum evaporated thin films in order to gain more insight into the underlying physical processes and to evaluate whether properties like band-like transport also occur in such systems. In the next section, the physical processes and energy level alignment mechanisms at metal/organic and organic/organic interfaces are discussed.

2.3 Interfaces involving organic semiconductors

Most organic electronic devices comprise interfaces between different organic semiconductors and/or metal electrodes. Understanding and controlling how energy levels align at such interfaces is crucial for improving their performance and lifetime or even find new application possibilities. For example charge injection from an electrode into the emitter material in an organic LED is governed by the the alignment of the organic’s frontier orbitals and the metal’s Fermi level and by the width and height of the potential barrier that forms at the interface. In organic photovoltaic cells on the other hand, efficient charge separation depends on the energy level alignment at the interface between absorber and acceptor molecules. While this issue in inorganic semiconductors is well understood, it is still a matter of scientific research in the field of organics. In the next section, an overview of the energetics and relevant processes that occur at metal/organic and organic/organic interfaces is given. This issue has been addressed by some excellent review articles that served as basis for the following [62–66].

Organic / metal interfaces

Charge injection and extraction barriers at metal-semiconductor interfaces are important parameters for the performance of devices. In the field of classical semiconductor physics, early investigations led to the formulation of the Schottky-Mott rule in the 1930s. It neglects all possible interactions at the interface and assumes a simple vacuum level alignment. It was also one of the first models to predict the energy level alignment at metal/organic interfaces. Using the electron affinity (EA) and the ionisation potential (IP) of the organic semiconductor molecules, two intrinsic parameters which can be determined by gas phase measurements, the hole injection barrier (HIB) and electron injection barrier (EIB) are related to the metal’s workfunction Φ_{metal} by

$$\text{HIB} = \text{IP} - \Phi \quad (2.3)$$

$$\text{EIB} = \Phi - \text{EA} \quad (2.4)$$

However, these relations are almost never observed in real systems, because some interactions that prevent vacuum level alignment are often present.

Fig. 2.9 shows a schematic energy level diagram of a metal/organic interface where the metal’s Fermi level lies well between HOMO and LUMO of the organic. Upon contact, thermodynamic equilibrium is established and hence a common Fermi level. In the case of physisorption, only van-der-Waals forces are present and no chemical hybridisation of the frontier orbitals is taking place. Hence, no charges are transferred and vacuum level alignment (Schottky-Mott limit) would be expected. However, often a vacuum level shift

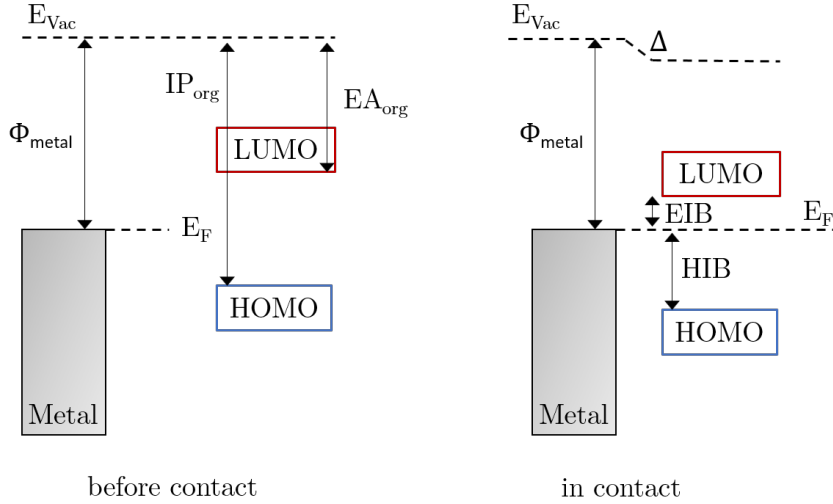


Figure 2.9: Simplified energy level diagram of a organic semiconductor/metal interface before and after contact. With only van-der-Waals interactions present, the pushing back of the metal's spilled out electron density can lead to an interface dipole Δ which reduces the electron injection barrier (EIB) and increases the hole injection barrier (HIB) compared to a vacuum level alignment scenario.

is measured which is referred to as interface dipole Δ . This is related to the nature of the metal's work function which is made up of two contributions: The bulk chemical potential and the electrostatic potential drop across the surface. At an atomically clean metal surface, there is no sharp cut-off of the electron cloud but a spill-out of electron density across the surface into the vacuum, known as dangling bonds [67]. This results in an electrostatic dipolar layer, also referred to as surface dipole, which depends on the surface crystal orientation. When a molecule is adsorbed at such a surface, the spilled out electron density is pushed back by Pauli repulsion leading to a decrease of the surface dipole and thus a measured interface dipole, the magnitude of which mainly depending on the adsorption distance. This effects is called "pillow-effect" or "push-back effect" in literature and can reach a magnitude of up to 0.7 eV [66]. It leads to a change of the HIB and EIB, compared to the vacuum level alignment scenario as shown in Fig. 2.9 according to:

$$\text{HIB} = \text{IP} - \Phi + \Delta \quad (2.5)$$

$$\text{EIB} = \Phi - \text{EA} + \Delta \quad (2.6)$$

There are several molecule-substrate interactions that may lead to a deviation from the physisorption regime and thus alter the magnitude and direction of the interface dipole. For non-inert metals, a hybridisation of molecular orbitals or a bond formation between the metal and specific sites of the molecule might occur [68–70]. This may lead to a distortion of the molecule and in some cases to a formation of intra-molecular dipoles [71].

The other extreme case can occur at interfaces between an inert metal and an organic semiconductor with an EA larger than Φ_{metal} or an IP smaller than Φ_{metal} . The former case is depicted in Fig. 2.10.

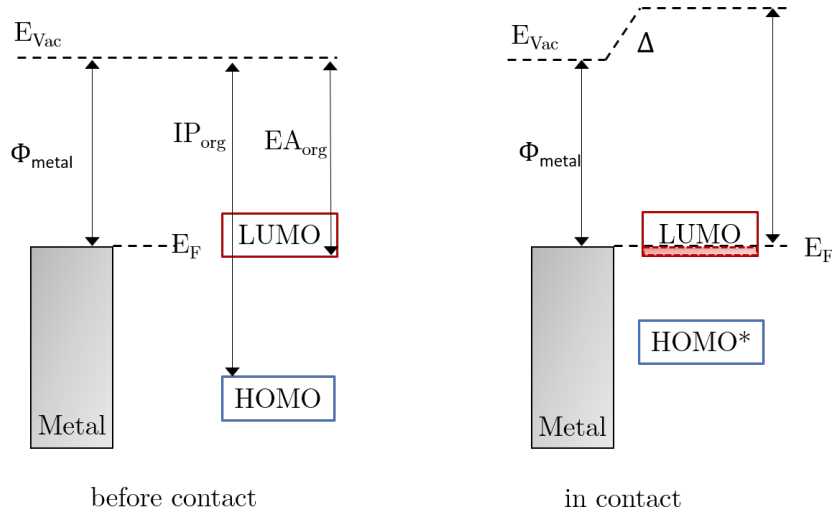


Figure 2.10: Simplified energy level diagram of an organic semiconductor/metal interface where the electron affinity of the organic is larger than the metal's work function. Charge is transferred into the organic's LUMO until thermodynamic equilibrium is reached. The polaronic relaxation of the molecule leads to a reduction of the gap between former HOMO (HOMO*) and now partially filled LUMO. The resulting space charge region induces an interface dipole Δ .

Here, the metal's Fermi level would lie within the LUMO of the organic semiconductor which leads to a charge transfer from the metal to the molecule until thermodynamic equilibrium is reached. This creates a narrow space charge region which leads to shift of the vacuum level, an interface dipole as shown in Fig 2.10. Assuming no hybridisation between molecular and metal orbitals, an integer charge transfer by tunnelling or hopping may occur. The additional charge on the molecule leads to a polaronic relaxation of the frontier orbitals, as discussed in section 2.2. The injection barriers in such systems can no longer be calculated using Eq. 2.3 - 2.6 but instead become largely independent of Φ_{metal} . The relation between Φ_{metal} and the work function of the organic semiconductor deposited on top Φ_{org} can be rationalised by introducing a slope parameter S , defined by

$$S = \frac{d\Phi_{org}}{d\Phi_{metal}}. \quad (2.7)$$

Its progression for an inert interface is shown in Fig. 2.11. For metal substrates with work functions below $\Phi_{crit,low}$, E_F falls into the LUMO of the organic, leading to a charge transfer from the metal to the organic semiconductor and a Φ_{org} which is independent of Φ_{metal} . For metal work functions between $\Phi_{crit,low}$ and $\Phi_{crit,high}$ no charges are exchanged and a linear relationship between Φ_{metal} and Φ_{org} can be observed. Without the push-back effect, S is unity, with push-back, S is smaller than 1. For metal work functions larger than $\Phi_{crit,high}$, the metal's Fermi level falls below the HOMO and charge is transferred from the organic semiconductor's HOMO to the metal, resulting in $S=0$. In analogy to the classical semiconductor physics, the regimes where $S=0$ are called Bardeen limit or Fermi level pinning. $S=1$ is expected when neglecting any interface interactions such as the push-back effect and assuming sharply defined HOMO and LUMO levels. Taking into account push-back and intra-gap states arising from disorder, defects or impurities, S takes values

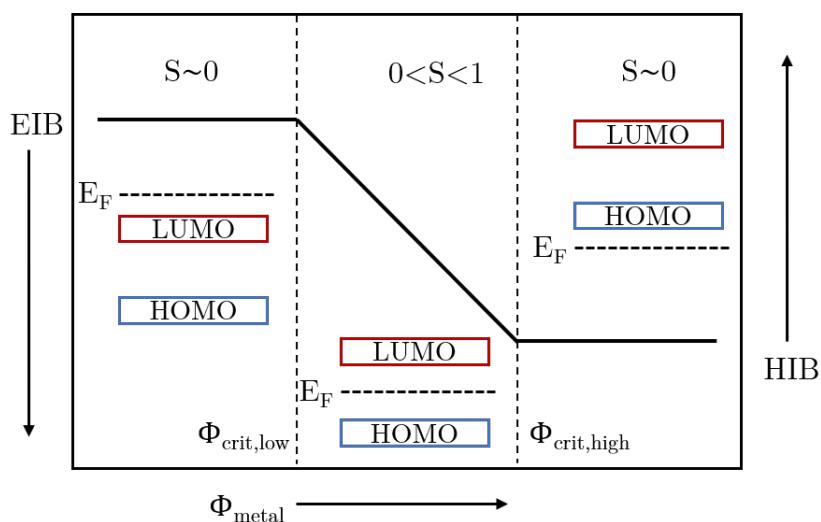


Figure 2.11: Scheme of the dependence of electron and hole injection barrier (EIB, HIB) of an organic semiconductor on the work function of the metal it is adsorbed on (Φ_{metal}) for an inert interface (no hybridisation, only integer charge transfer). At $\Phi_{\text{metal}} < \Phi_{\text{crit,low}}$ a charge transfer from the metal to the LUMO of the organic occurs, at $\Phi_{\text{metal}} > \Phi_{\text{crit,high}}$ vice versa. At these regimes the injection barriers are independent of Φ_{metal} yielding a slope parameter $S=0$. With the metal's Fermi level in between the organic's frontier orbitals, EIB and HIB depend linearly on Φ_{metal} yielding $0 < S < 1$. Without any interface effects, such as push-back or intra-gap states S equals 1, otherwise S is reduced to smaller values. Adapted from [63, 73, 74].

below 1 and the transition between Fermi level pinning regime and the Schottky-Mott regime is less abrupt. When a chemisorption with hybridisation or formation of covalent bonds is considered, the interface energetics become more complex, with entirely new states arising, and the relation shown in Fig. 2.11 is not valid any more. Since this scenario is beyond the scope of this work, the interested reader is referred to Refs. [63, 72].

Naturally, the question arises where the Fermi level gets pinned, or in other words how large Φ_{org} will be for a given system. In Fig. 2.10, Φ_{org} equals EA of the adsorbed molecule which would entail a vanishing EIB. However, with few exceptions [75], non-vanishing injection barriers of several hundred meV are observed in most systems. The reason for this is still under debate. Several models were developed to predict the energy level alignment at metal/organic interfaces, such as the induced density of states model (IDIS) [76] (for partial charge transfer), the integer charge transfer (ICT) model [63] and an iterative electrostatic model [74]. The models suggest that the Fermi level is not pinned inside the HOMO or LUMO of the neutral molecule but at other states that extend into the gap. Depending on the model, polaron states (ICT model [63, 66], cf. Fig. 2.8 and Sec. 2.2), surface states (IDIS model) or defect or impurity induced states are suggested [74, 77].

Organic / organic interfaces

At organic/organic interfaces, the concepts of vacuum level alignment (without charge transfer) and Fermi level pinning (with charge transfer) are also applied. Due to the much lower amount of free moving charge carriers, the push-back effect is not observed at organic/organic interfaces. Therefore, vacuum level alignment is more frequent than at metal/organic interfaces. In analogy to metal/organic interfaces, the charge transfer can be integer or partial. The IDIS model [78] for partial charge transfer and the ICT model [63, 66] for integer charge transfer were also applied to organic/organic interfaces and showed good agreement in certain systems. However, they could not explain why the energy level alignment depended on the deposition sequence in some cases. This issue was addressed by Oehzelt et al., who developed an electrostatic model [64, 74] which takes the Fermi level position of the underlying substrate into account and will be briefly introduced in the following.

Since interfaces can only be studied by photoemission if sample charging is avoided, they need to be prepared on conducting substrates and consequently electronic equilibrium across the hole heterojunction is achieved, which entails the formation of a common Fermi level. Thus, when analysing organic/organic interfaces, the interaction of the bottom organic with the substrate influences charge transfer and energy level alignment in the whole structure. The model discretises the organics into homogeneous sheets with material specific molecular area density, dielectric constant and density of states (DOS) and approximates HOMO and LUMO by Gaussians. After initially occupying the DOS of the first organic up to the Fermi level of the substrate, a lateral charge density profile is obtained which is used to calculate the electrostatic potential by numerically solving the Poisson equation. After shifting the DOS by the amount of the electrostatic potential, the DOS is again occupied up to the Fermi energy and the whole process is repeated iteratively until convergence is reached [74]. An energy level diagram deduced from this model is shown in Fig. 2.12. It comprises donor type material on a metallic substrate and an acceptor that fulfils the condition of $EA_{Acc} > IP_{Don}$ which is deposited on top. Here, the Fermi level would lie above the LUMO of the acceptor which leads to a charge transfer from the donor to the acceptor and thus a narrow space charge region. This leads to a potential step across the interface that is reflected in a bending of the vacuum level (interface dipole) and the associated frontier orbitals.

The model showed good agreement with experiments on several organic heterostructures. Moreover, it pointed out that the energy level alignment deduced by UPS measurements of stepwise deposited films does not reflect the real potential evolution in the final heterostructure because the local DOS and potential do not remain constant upon subsequent deposition of material. This entails that a potential shift measured by UPS is not necessarily an interface dipole due to a charge transfer between the two organic materials but can also be a result of charge diffusion from the metal substrate to the top organic layer. This leads to a capacitor-like potential progression across the heterostructure that might be misinterpreted as an interface dipole stemming from charge transfer between the two organics.

In analogy to metal/organic semiconductors, the Fermi level pinning position at organic/organic interfaces is still a topic of scientific discussion. Disorder induced gap states, interface states and polaronic states are discussed as pinning positions [79]. The charge transfer and thus the energy level alignment at molecular interfaces can be altered

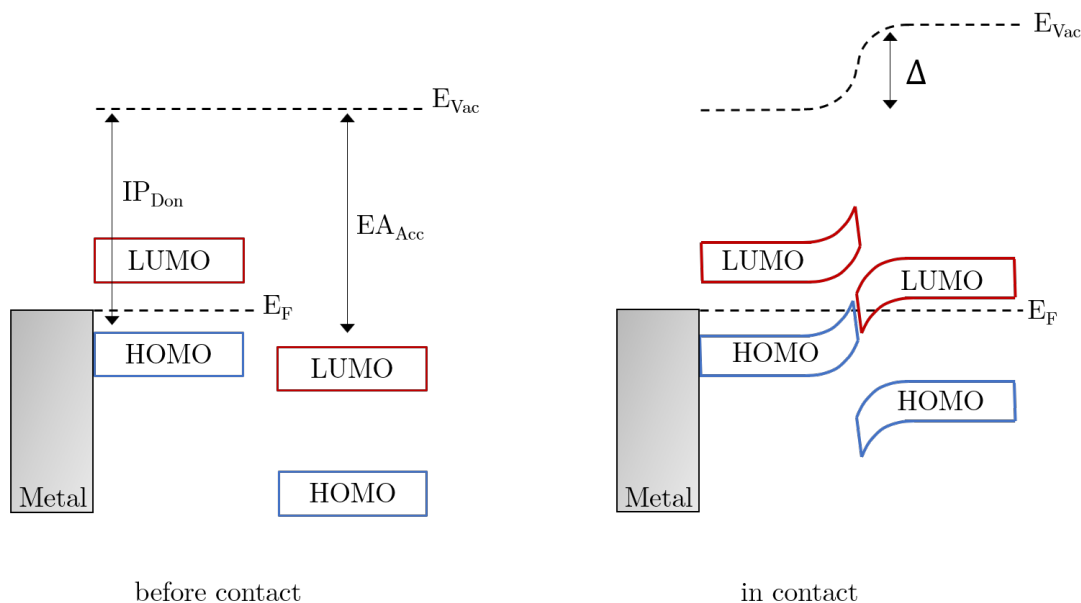


Figure 2.12: Simplified energy level diagram of two organic semiconductors that fulfil the condition of $IP_{Don} < EA_{Acc}$ before (left) and after contact (right). Charge transfer from the donor's HOMO to the acceptors LUMO leads to an interface dipole Δ that shifts the vacuum level and the frontier orbitals of the organics. This scheme is based on a purely electrostatic model [64] which assumes molecularly sharp interfaces and dismisses charge transfer induced disordering and polaronic relaxation of the molecules at the interface. Adapted from [64].

by several local effects. EA and IP of an organic semiconductor can differ depending on the morphology of the film [80]. This means that the same material pair could lead to different charge transfer properties depending on the orientation of the molecules to each other. Also, contact induced reorientation of molecules at interfaces is frequently reported in literature [77, 81, 82]. Moreover, an interdiffusion of molecules at the interface could lead to different electronic properties than expected for a molecularly sharp interface.

As elaborated in Sec. 2.2, interesting new effects, such as metallic conduction [15], superconductivity [59] and Mott insulation [83] were reported at single crystalline donor/acceptor interfaces and within single crystals that comprise separate stacks of donors and acceptors. In all of these systems, a charge transfer is present, which leads to a partial filling of initially unoccupied states. For example for the TTF/TCNQ combination, a degree of charge transfer of $\rho=0.59$ is reported for the binary crystal [56, 84], whereas for the interface this parameter is not yet determined experimentally. The exact mechanisms that determine whether a donor/acceptor interface becomes metallic are not clear yet. For example in the case of the TTF/TCNQ interface, no consensus has yet been reached in literature whether the metallic state results from a sharp interface or from a thin layer of a TTF/TCNQ charge transfer salt formed by interdiffusion [85–87]. However, some requirements seem to be necessary to achieve a delocalisation of charge carriers. After a charge transfer, the additional electron on the acceptor and hole on the donor are bound by a Coulomb binding energy which needs to be overcome for the charges to become delocalised. This can be achieved by a polarisation of neighbouring

molecules that screen the respective charges [87]. Further reduction of the binding energy could be achieved by a large spatial separation of the exchanged charges on their respective molecules. Moreover, a large frontier orbital overlap of neighbouring molecules is required to ensure a high hopping rate or even the formation of bands. Whether these requirements can be fulfilled also in thin films or only in highly ordered systems is not clear. In this thesis, several donor/acceptor interfaces will be investigated with regard to new charge transfer induced electronic properties.

2.4 Materials

The materials, investigated in this work were chosen based on their scientific or application related relevance. As outlined in Section 2.2, the electron affinity (EA) of the acceptor and the ionisation potential (IP) of the donor play an important role in evaluating the charge transfer potential. The used acceptors are listed in Table 2.1, together with their EA values, reported in literature, and the donors in Table 2.2 with their IP, determined by UPS measurements of our group. As outlined in Sec. 2.1, even though EA and IE are intrinsic properties of single molecules, their values in thin films depends on the molecules' mutual interaction and therefore on the spatial orientation, which is why varying values are found in literature. In the following, the respective molecules and their relevance are introduced in detail.

Table 2.1: Overview of the molecular acceptors used in this work and their electron affinity in solid state, reported in literature.

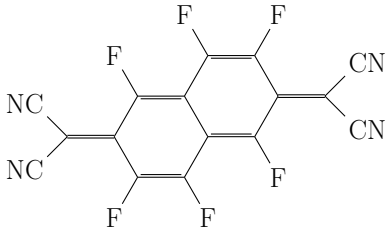
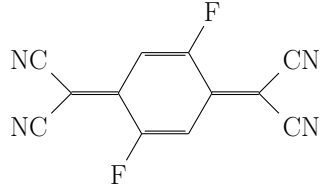
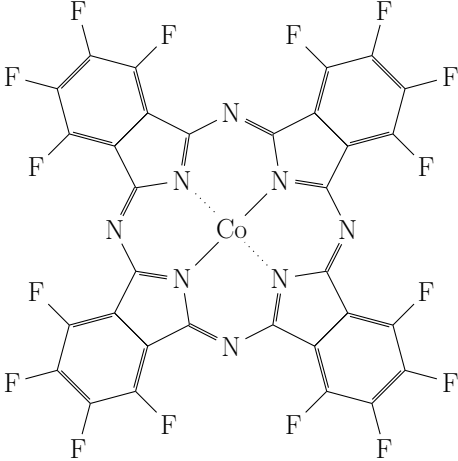
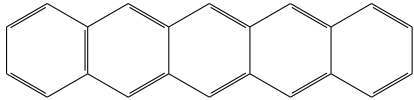
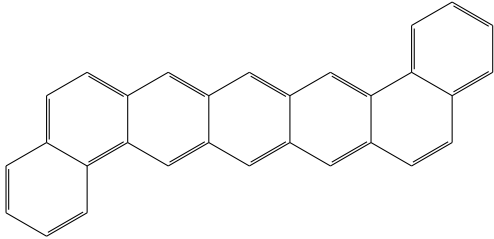
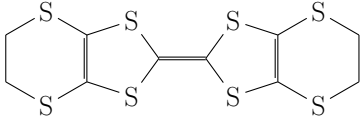
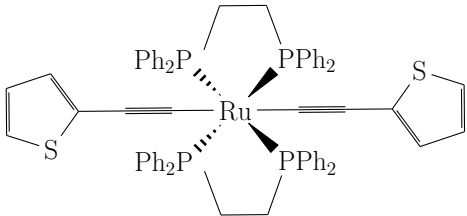
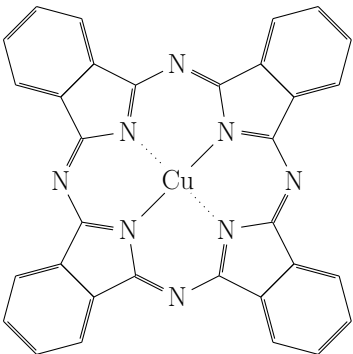
Structure	Name	Electron affinity
	F_6TCNNQ $(F_6C_{16}N_4)$	5.0-5.6 eV [88, 89]
	F_2TCNQ $(F_2C_{12}N_4)$	4.6-5.4 eV [90-92]
	$F_{16}CoPc$ $(F_{16}CoC_{32}N_8)$	4.5 eV [93]

Table 2.2: Overview of the used molecular donors and their ionisation potentials in thin films measured by UPS in this work.

Structure	Name	Ionisation potential
	Pentacene (C ₂₂ H ₁₄)	5.1 eV
	1,2:8,9-dibenzopentacene (C ₃₀ H ₁₈)	5.0 eV
	ET (C ₁₀ H ₈ S ₈)	5.1 eV
	<i>trans</i> -[Ru(dppe) ₂ (T) ₂] (C ₆₄ H ₅₄ P ₄ S ₂ Ru)	5.0 eV
	CuPc (H ₁₆ CuC ₃₂ N ₈)	4.8 eV

F_2 TCNQ and F_6 TCNNQ

Frequently used electron acceptors in the field of organic semiconductors are molecules of the tetracyanoquinodimethane (TCNQ) family. They are planar molecules that consist of an aromatic core with cyanide functional groups at both sides and have a length of about 8 Å. TCNQ gained attention as anionic constituent of the charge transfer salt with metal-like conductivity TTF-TCNQ [55]. The electron affinity of TCNQ, determined by inverse photoemission spectroscopy is around 4.2 eV [90]. It can be increased by fluorination, yielding the related molecules F_2 TNCQ (EA=4.6 to 5.4 eV) and F_4 TCNQ (EA=5.1 to 5.2 eV). F_4 TCNQ is a widely used p-dopant in organic electronics [94–96]. F_2 TNCQ ($C_{12}F_2N_4$) on the other hand exhibits interesting transport properties in single-crystalline form, [18, 97] e.g. a band-like mobility that increases with decreasing temperature which differs from TCNQ and F_4 TCNQ that do not show signs of band-like transport. Furthermore, it forms a binary crystal with BEDT-TTF that is a Mott insulator [83, 98] and the interface between single-crystalline F_2 TNCQ and BEDT-TTF is reported to show metallic conductivity [19].

1,3,4,5,7,8-Hexafluorotetracyanonaphthoquinodimethane (F_6 -TNAP or F_6 TCNNQ) [99] with the chemical composition $C_{16}F_6N_4$ is a close relative to the TCNQs. It has an additional carbon ring and is therefore larger (around 11 Å) and has higher sublimation temperatures which makes it easier to handle in ultra-high vacuum. F_6 TCNNQ has a reported EA of 5.0 to 5.6 eV [88, 89] which is higher than that of the TCNQs due to the additional two fluorine atoms. It is frequently used for doping organic thin films [88, 100] in transistors [101] and OLEDs [102]. Also its use for tuning the electronic structure of inorganic materials, such as perovskite films [103], graphene [104] or transition metal dichalcogenides [105] is reported.

Polycyclic aromatic hydrocarbons

Polycyclic aromatic hydrocarbons (PAHs) are planar molecules containing only hydrogen and carbon that consist of multiple aromatic rings. They occur after incomplete combustion of organic material and present a health risk to humans because they have been linked to various types of cancer. The rings can be arranged in different ways yielding a great variety of molecules. The reported discovery of superconductivity in alkali metal doped PAHs, such as picene [106], phenanthrene [107] and 1,2:8,9-dibenzopentacene [108] at relatively high temperatures ($T_c=33$ K for potassium doped dibenzopentacene) lead to increased scientific interest in the electronic properties of this class of compounds. However, these findings were hardly reproducible which lead to an ongoing debate about the responsible mechanism and the stability of the reported superconducting phases [109]. Due to its high hole mobility and its ability to undergo singlet fission, pentacene is frequently investigated as material for organic field effect transistors or organic photovoltaics [110, 111]. The two PAH's that were investigated in this work, pentacene ($C_{22}H_{14}$) and 1,2:8,9-dibenzopentacene ($C_{30}H_{18}$, DBP) are shown in Table 2.2. Pentacene comprises five linearly fused benzene rings and is a member of the [n]-acene family. DBP has the same structure but with two additional benzene rings at the 1,2 and 8,9 positions.

Transition metal phthalocyanines

Transition metal phthalocyanines (TM Pc's) comprise a π conjugated planar macrocyclic ring (ligand) with a transition metal atom in the centre (see Tables 2.12.2). The ligand consists of the so called phthalocyanato ion ($C_{32}H_4N_8^{2-}$) which leaves the metal centre (e.g. Mn, Fe, Co, Ni, Cu or Zn) in the formal oxidation state II. Due to their high symmetry, TMPc films grown by vacuum sublimation exhibit a relatively high order without island formation. Moreover, they are chemically stable, easy to process and producible in large amounts. This makes them attractive for an application in organic electronic devices [112, 113].

BEDT-TTF

Bis(ethylenedithio)tetrathiafulvalene (BEDT-TTF or ET) with the chemical formula $C_{10}H_8S_8$ is an organosulfur molecule. Its molecular structure is shown in Table 2.2. It gained a lot of interests because it serves as donor cation for a large family of organic superconductors [114]. The highest transition temperature at ambient pressure was found for the compound κ -(ET) $_2$ Cu[N(CN) $_2$]Br at 11.6 K [115]. The purely organic combination of F $_2$ TCNQ and ET on the other hand, is reported to form a charge transfer crystal that is a Mott insulator [83, 98]. Of particular interest in light of the present work is the reported band-like transport at the interface between single crystals of ET and F $_2$ TCNQ [19]. The ionisation potential of an ET film on polycrystalline gold was determined to be 5.1 eV which makes it an interesting donor candidate for a charge transfer interface with the acceptor F $_6$ TCNNQ.

trans-[Ru(dppe) $_2$ (T) $_2$]

The Ruthenium-acetylide complex *trans*-[Ru(dppe) $_2$ (T) $_2$] was synthesised by Po Yuen Ho, from Franziska Lissel's group at the Leibniz institute for polymer research Dresden. Its structural formula is shown in Table 2.2 and its spatial structure from single crystal X-ray diffraction (by Olivier Blacque, University of Zurich) is shown in Fig. 4.15. It comprises a Ru centre surrounded by a phosphine ligand and end-capped with thiophene. Metal-acetylide complexes are potential building blocks for molecular wires due to the interaction of the metal's d_{xz} and d_{yz} orbitals with the π -orbitals of the polyynic units ($-C\equiv C-$). This interaction may lead to the possibility of switching the conductance of the polymer by charge-state alternation of the metal centre [116]. The ionisation potential of *trans*-[Ru(dppe) $_2$ (T) $_2$] in solid form was determined to be 5 eV. In this work, the electronic properties of a pristine film and the charge transfer characteristics to the acceptor F $_6$ TCNNQ were investigated.

Buckminster fullerene C $_{60}$

Buckminster fullerenes are hollow molecules that consist of exclusively pentagonal and hexagonal carbon rings. Its structure is shown in Fig. 2.13. Due to its electron affinity of about 4.5 eV [90], it serves as electron acceptor in solar cell applications [117]. Moreover it is gained a lot of scientific attention in the 1990s when superconductivity in alkali metal doped fullerenes was discovered [60]. The possibility of using C $_{60}$ as a container for other species such as metal atoms has led to the emergence of another interesting research field

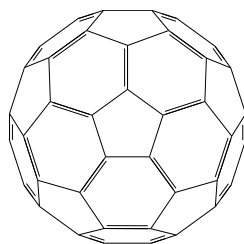


Figure 2.13: Structure of Buckminster fullerene C₆₀.

which studies such so called endohedral fullerenes [118]. In this work, C₆₀ is only used for calibrating the satellite correction for UPS measurement due to its well separated and well defined frontier orbitals (cf. Fig. 3.5).

3 Photoemission Spectroscopy

3.1 Theoretical background

Photoemission spectroscopy (PES) is a widely used experimental technique to investigate the chemical composition and the electronic structure of solids, gases or liquids. It is based on the photoelectric effect which was discovered experimentally by Hertz [119] and Hallwachs [120] in 1887 and theoretically explained by Einstein in 1921 [121]. The development of PES to one of the most important techniques for surface and solid state physics was pushed significantly by Siegbahn who received the Nobel Prize in physics for those achievements in 1981 [122].

The term photoelectric effect means the emission of electrons due to the exposure of a solid to electromagnetic radiation. The product of the Planck constant h and the frequency of the electromagnetic wave yields the photon energy $h\nu$. For photoionisation to happen, the incoming photon needs to transfer all its energy to an electron. The kinetic energy E_{kin} of the emitted photoelectron is then given by

$$E_{kin} = h\nu - E_B - \Phi \quad (3.1)$$

with Φ being the work function of the solid and E_B the binding energy of the electron relative to the Fermi energy. Other photoionisation processes like the Compton effect where the photon only transfers part of its energy to an electron do not contribute significantly at photon energies below 500 keV [123]. In PES, the kinetic energy of the photoelectrons is measured by an analyser which gives a spectrum with peaks at certain energies that reflect the binding energies of the electrons in the solid. Taking into account the photoionisation cross sections for the respective orbitals at the given photon energy, the photoemission spectrum allows conclusions about the distribution of the density of states (DOS) in the sample. The core level electrons are excited by an X-ray source (XPS) while the valence levels are probed by ultra-violet light from a gas discharge lamp (UPS) because it offers a higher resolution. The relation between the electronic states in the solid and the PES spectrum is shown schematically in Fig. 3.1. In the following, the photoemission process is discussed in more detail on the basis of the articles [124–127].

Photoemission is a complex many body problem, because the coupling of the initial state of the N -electron system to the final state of the $(N-1)$ -electron system and the photon field needs to be taken into account. A complete theoretical quantum mechanical treatment of this is attempted by the so called one step model [129]. A more intuitive model that has proven useful for the understanding of PES in most cases is the three-step model [130] which artificially divides the photoemission process into the steps (i) photoexcitation, (ii) transport of the hot electron to the surface and (iii) transmission of the electron through the surface into the vacuum [127].

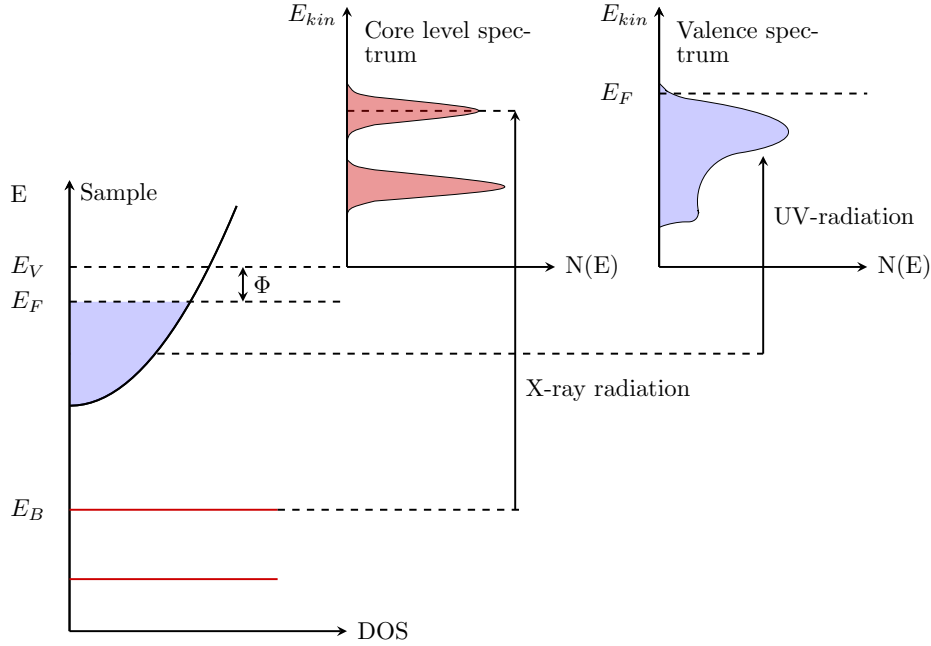


Figure 3.1: Schematic representation of the energy levels in a solid (metal) and the energy distribution of the photoelectrons excited by photons of energy $h\nu$. Based on [124, 128].

In step (i), an electron in the initial state Ψ_i with energy E_i absorbs the energy of an incoming photon leading to an optical excitation to the final state Ψ_f with the energy E_f . The probability P for such a transition is given by Fermi's Golden Rule:

$$P \propto \sum_{f,i} \frac{2\pi}{\hbar} |\langle \Psi_f | \mathcal{H}_{PE} | \Psi_i \rangle|^2 \cdot \delta(E_f - E_i - h\nu) \quad (3.2)$$

with the photoemission perturbation operator \mathcal{H}_{PE} describing the interaction between the electrons and the electromagnetic field and the delta distribution δ ensuring energy conservation. \mathcal{H} can be written in the single particle approximation as

$$\mathcal{H}_{PE} = \frac{e}{2m_e c} (\mathbf{A} \cdot \mathbf{p}) \quad (3.3)$$

with the electron mass m_e , the speed of light c , the vector potential \mathbf{A} and the momentum operator $\mathbf{p} = -i\hbar\nabla$. It is assumed that \mathbf{A} is constant over atomic dimensions (dipole approximation) and multi-electron processes are neglected.

In step (ii), the excited photoelectron propagates through the solid to the sample surface, undergoing elastic or inelastic scattering processes. Inelastic scattering on electrons or phonons leads to an energy loss and a change of the angular distribution of the photoelectron. Consequently, these electrons do not carry information about their initial state in the solid and form the so called secondary electron background in photoemission spectra (see Sec. 3.2.3). The effect of inelastic scattering can be quantified by introducing the mean free path λ_{in} which describes the average distance between two subsequent

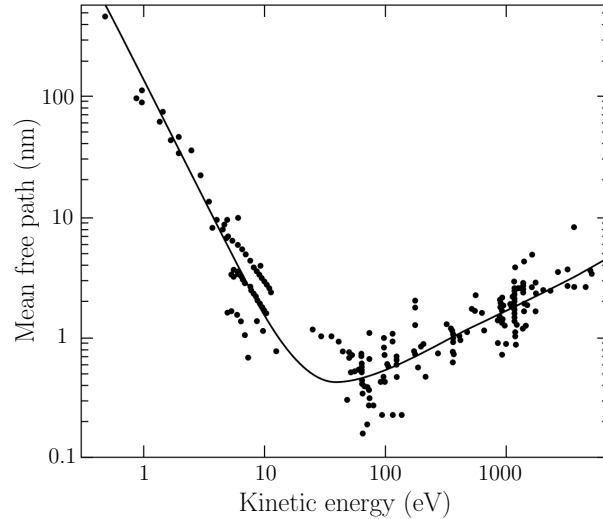


Figure 3.2: "Universal curve" that shows measured values of the mean free path for different organic materials in dependence of the kinetic energy for photoelectrons. Based on [131, 132].

scattering events. The current of photoelectrons in the sample along the path l follows an exponential damping law:

$$I(l) = I_0 \exp\left(-\frac{l}{\lambda_{in}}\right) \quad (3.4)$$

It was shown by Seah and Dench, that λ_{in} does not depend strongly on the element or material but rather on the kinetic energy of the photoelectrons [131]. Fig. 3.2 shows the so called universal curve with the experimentally determined λ_{in} of different materials. It becomes apparent that for the relevant energy range for PES experiments (10 to 1000 eV) λ_{in} is in the range of 1 to 10 nm which makes PES a very surface sensitive technique. This is also one of the reasons why PES experiments are carried out under ultra-high vacuum conditions to avoid surface contaminations.

In step (iii) the photoelectron leaves the sample and escapes into the vacuum. This only occurs if the electron has sufficient kinetic energy to overcome the work function of the sample (Eq. 3.1). Photoelectrons with a lower energy are reflected at the surface back into the solid and do not reach the detector. This leads to an abrupt cut-off of the photoemission spectrum at the respective kinetic energy, the so called secondary electron cut-off (SECO) or high binding energy cutoff (HBEC). Measuring the position of the SECO enables the determination of the sample's work function which will be discussed in more detail in Sec. 3.2.2. After escaping the sample, only the photoelectron's momentum component parallel to the surface $k_{||}$ is conserved, while the perpendicular component is not, due to the surface work function. By applying the dispersion relation of a free electron in vacuum, $k_{||}$ can be expressed in dependence of the emission angle θ :

$$|k_{||}| = \sqrt{\frac{2m_e E_{kin}}{\hbar^2}} \sin(\theta) \quad (3.5)$$

Thus, by using detectors that can measure θ , it is possible to map the electronic band structure of solids. This method is called angle-resolved photoelectron spectroscopy

(ARPES) [133] and requires samples of high crystallinity that are usually cleaved in-situ to ensure clean surfaces. Since this work focusses on organic thin films that are usually polycrystalline or amorphous, ARPES was not used.

The measured quantity in PES is the photocurrent $I(E_{kin})$ which is proportional to the probabilities of the steps (i),(ii) and (iii). The dependence of E_{kin} on steps (ii) and (iii) can be regarded as negligible [126] which yields

$$I(h\nu) \propto \sum_{i,f} |M_{fi}|^2 \delta(E_f - E_i - h\nu) \quad (3.6)$$

with the one-electron dipole matrix element $M_{fi} = \langle \Psi_f | \mathcal{H} | \Psi_i \rangle$.

3.2 Data analysis

The raw data sets obtained from UPS and XPS measurements consist of intensity values in form of counts, in dependence of the kinetic energy $E''_{kin} = E'_{kin} + \Phi_{spec}$ (cf. Eq. 3.15). The addition of the spectrometer's work function Φ_{spec} is done by the measurement software. Before analysing the spectra with regard to their physical meaning, they have to be pretreated. The first step is the conversion of the energy scale into binding energy with the following relation:

$$E_B = h\nu - E''_{kin} + \Delta E, \quad (3.7)$$

with ΔE being a possible energy offset due to small instrumental errors. In the case of XPS measurements, ΔE is the difference to the substrate peak which is used for energy scale calibration (mostly $\text{Au}4f_{7/2}$ at 84.0 eV or the $\text{Ag}d_{5/2}$ at 368.2 eV). This offset normally lies between 0 and 0.5 eV and the spectrum is shifted accordingly. For UPS spectra, the substrate Fermi edge is used for calibration, hence ΔE is the difference of the Fermi edge position to 0 eV binding energy. Additional steps in data treatment of PES spectra are explained in the following section. Furthermore, physical effects that determine the shape of PES spectra and the determination of important physical quantities from those spectra are discussed.

3.2.1 General line shape and secondary electron background

The shape of photoemission peaks is determined by the instrumental resolution (extrinsic) and the photoemission process itself (intrinsic). The instrumental resolution depends on the line shape of the incoming X-rays and the limited resolution and response function of the detector. These lead to a broadening of the photoemission lines which is usually assumed to be Gaussian. An important intrinsic effect which sets a lower limit to the peak width of PES features is the finite lifetime of the excited state created by photoionisation. According to Heisenberg's uncertainty relation, this leads to an energy uncertainty and hence a broadening of the photoemission line. This natural broadening due to lifetime effects is usually described by Lorentz type contributions. The peak shape is also influenced by other mechanisms that induce binding energy shifts that manifest themselves in an apparent peak broadening. Some of these effects, in particular those which are relevant for the interpretation of PES spectra of molecular films are introduced in the following

sections.

For the interpretation of PES experiments, spectra are often fitted by certain functions with adjustable parameters. Due to the great variety of observed peak shapes there are many synthetic line shapes used. One of the most popular ones which is also used in this work is the Voigt profile which consists of a convolution of a Gaussian and a Lorentzian function. The intensity in dependence of the energy is described by

$$I(E) = (G * L)(E) \propto \int_{-\infty}^{+\infty} G(E')L(E - E')dE', \quad (3.8)$$

with the Gauss function G and the Lorentz function L which are given by

$$G(E) = \frac{\exp(-\frac{E^2}{2\delta^2})}{\delta\sqrt{2\pi}} \quad (3.9)$$

$$L(E) = \frac{1}{\pi} \frac{\gamma}{(\epsilon^2 + \gamma^2)}.$$

with the instrumental and intrinsic line widths δ and γ .

As already discussed in Sec. 3.1, inelastically scattered photoelectrons form a so called secondary electron background which causes asymmetry in the measured PES spectra. In order to ensure comparability between different spectra and enable a reliable fitting procedure, the background is often subtracted. Fig. 3.3 shows the Au4f core level spectrum of a gold foil with the raw spectrum in black. The underlying energy loss mechanisms differ depending on the investigated materials and their prediction or modelling is a very complex task. There are several algorithms for approximating the background, the most common ones are a simple linear background, the Tougaard [134] and the Shirley algorithm [135]. Due to the large number of peaks in the UPS valence spectra, a background correction is very complex which is why UPS spectra shown in this work are not background corrected. For all XPS spectra shown in this thesis, the Shirley background was subtracted. It is calculated with the assumption that the intensity of inelastically scattered electrons is proportional to the number of photoelectrons with a higher kinetic energy. The subtraction of the background is an iterative process in i steps until the background intensity B_S converges. It is calculated by [136]

$$B_{S,i}(E) = k_n \int_E^{+\infty} (I(E') - I_{max} - B_{S,i-1}(E'))dE', \quad (3.10)$$

where I is the measured intensity at a given energy, I_{max} is the upper bound of the energy in the energy range and k_n is a scattering factor which is calculated iteratively by

$$k_i = \frac{I_{min} - I_{max}}{\int_{E_{min}}^{E_{max}} (I(E') - I_{max} - B_{i-1}(E'))dE'} \quad (3.11)$$

The calculated Shirley background is shown in blue in Fig. 3.3 in the corrected spectrum in red.

3.2.2 UPS analysis

Ultraviolet photoelectron spectroscopy (UPS) offers the possibility of probing occupied states in the valence region and gives access to important electronic parameters of the

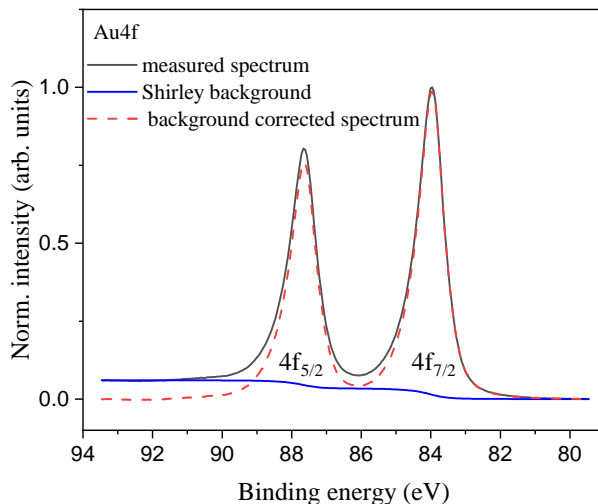


Figure 3.3: Au4f core level spectrum of a gold foil before and after the subtraction of the calculated Shirley background.

sample, such as the ionisation potential IP and the work function Φ . Fig. 3.4 shows the UPS spectrum of C₆₀, a prototypical organic semiconductor, deposited on a gold substrate. The spectrum is referenced to the binding energy with the zero point at the Fermi edge of the substrate. The valence spectrum of the substrate (blue) was measured prior to the deposition of C₆₀. The first peak around 1.2 eV reflects the occupied density of states of the HOMO level of C₆₀. It is common practise in PES to define the position of the HOMO as the low binding energy onset of the HOMO derived peak. The energy distance between HOMO leading edge and the substrate Fermi level is referred to as hole injection barrier (HIB). The HOMO is followed by the lower lying molecular orbitals until the spectrum shows a sharp cutoff around 16.7 eV. This so called high binding energy cutoff (HBEC) or secondary electron cutoff (SECO) stems from the slowest inelastically scattered electrons that have just enough kinetic energy to surpass the sample's work function and reach the detector. The binding energy position of the HBEC gives the width of the spectrum which allows the determination of the sample work function Φ according to the relation

$$\Phi = h\nu - \text{HBEC}. \quad (3.12)$$

From this, it is possible to deduce the ionisation potential (IP) which is given by

$$\text{IP} = \text{HIB} + \Phi. \quad (3.13)$$

As discussed in Sec. 2.2, the IP plays an important role for determining the charge transfer potential of a given donor/acceptor pair (Eq. 2.2). The other important material parameter, the electron affinity (EA), cannot be determined by UPS because it requires knowing the position of the LUMO which is only accessible by other methods, for example inverse photoemission spectroscopy (IPES).

UPS spectra, recorded with non monochromatised UV radiation show states at negative binding energy which does not make sense physically due to the electronic nature of the sample. These states stem from photoelectrons that are emitted by the small portions of HeI _{β} (23.09 eV) and HeI _{γ} (23.75 eV) radiation that are present in the UV lamp emission

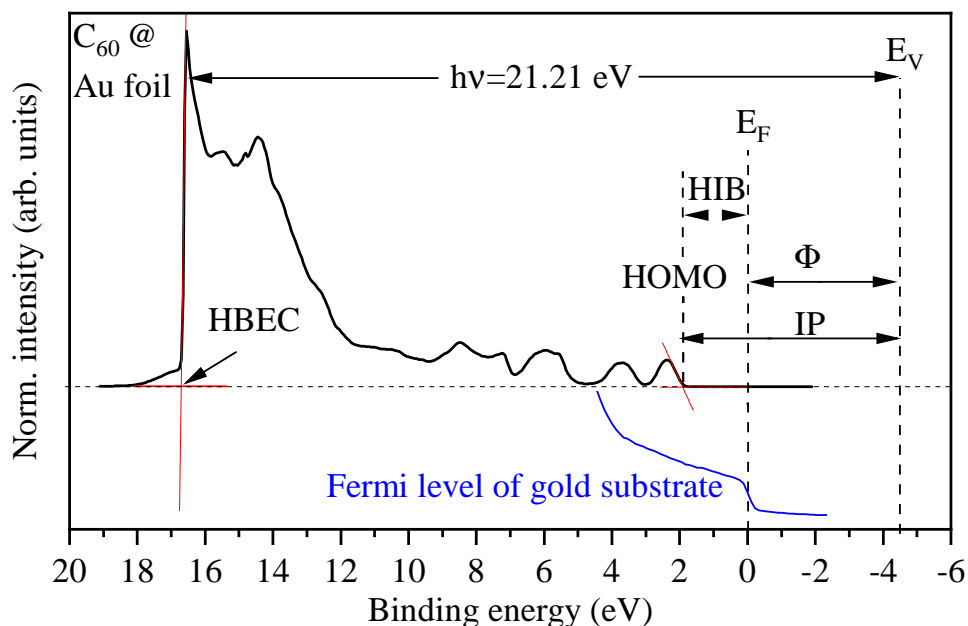


Figure 3.4: UPS spectrum of a C₆₀ film evaporated on a gold foil as substrate. Fermi edge of substrate is shown in blue and scaled up in intensity for clarity.

Table 3.1: Satellite excitations of the He gas discharge lamps HIS13 (PHI setup) and UVS300 (SPECS setup) and their respective percental intensities.

excitation	energy	energy difference	intensity UVS300	intensity HIS13
HeI _α	21.21 eV	-	≈ 100 %	≈ 100 %
HeI _β	23.06 eV	1.85 eV	4.0 %	1.56 %
HeI _γ	23.75 eV	2.53 eV	0.6 %	0.28 %

spectrum besides the desired HeI_α (21.21 eV) radiation. This so called satellite radiation leads to the emission of electrons with higher kinetic energies that appear at lower binding energies in the spectrum. Fig. 3.5 shows the raw UPS spectrum of C₆₀ in the low binding energy region together with the satellite spectra. The raw spectrum is corrected by subtracting the satellite spectra, which are assumed to be equal to the raw spectrum but shifted by the difference in photon energy and reduced in intensity by a certain factor. The energy shifts and intensity percentages were determined by measuring a C₆₀ film on gold and are given in Table 3.1.

3.2.3 XPS analysis

X-ray photoemission spectroscopy (XPS) is used for measuring atomic core levels. The core level binding energy is specific for each element and the peak area is proportional to the elemental concentration which makes XPS a useful tool for analysing the stoichiometric composition of a sample. Moreover, the binding energy of a core level is sensitive to the electronic environment of the atom. Thus, in the context of organic semiconductors, XPS allows the investigation of charge transfer between different molecules, because

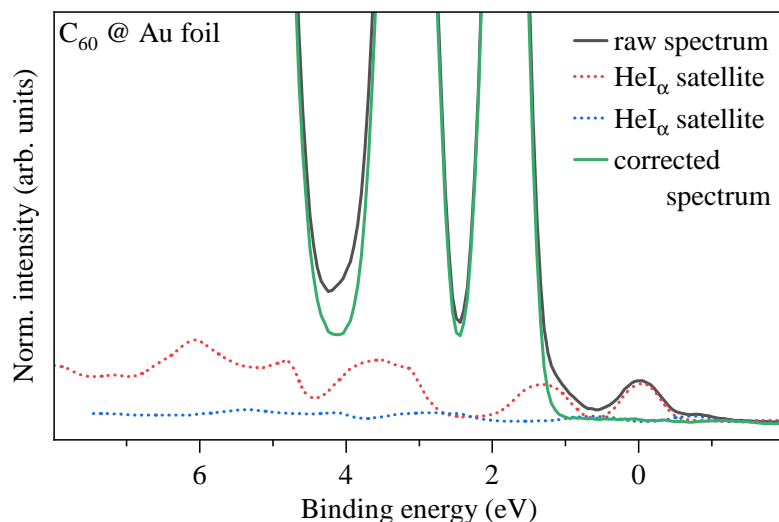


Figure 3.5: Raw UPS spectrum of a C_{60} film evaporated on a gold foil substrate (black) the two satellite derived spectra (blue and red) and the satellite corrected spectrum (green).

changes in the occupation of the valence orbitals lead to binding energy shifts in the core levels. In the following, important physical phenomena and their manifestation in XPS spectra are described in more detail.

Binding energy shifts

Binding energy shifts of the core levels can be attributed to initial state or final state effects. One important initial state effect is referring to the chemical environment of the photoelectron in the ground state which gives rise to the term "chemical shift". When an atom is bound to another atom, part of its valence electron density is withdrawn which leads to a decreased screening of the core hole and hence to a higher measured binding energy. An example for this effect is shown in Fig. 3.6 (left) for the Si2p core level which is shifted significantly to a higher binding energy for SiO_2 compared to pure Si. Chemical shifts also occur in molecules, a popular example is the C 1s spectrum of ethyltrifluoroacetate, shown in Fig. 3.6 (right), which exhibits four distinct peaks depending on the electronegativity (degree of charge withdrawal) of the carbon atoms' binding partners. This sensitivity of the core level binding energy to the chemical environment is used in this work to probe charge transfer to or between organic molecules. Since the binding energy shifts can be quite small in some cases and are often superimposed by non shifted peaks, they manifest themselves in asymmetries or shoulders in the core level spectra which have to be analysed by a suitable fitting procedure.

Another initial state effect is spin-orbit splitting, which occurs in all orbital levels with an angular momentum quantum number l larger than 0. For example the Au4f spectrum, shown in Fig. 3.3, comprises two peaks with a separation of 3.7 eV and an area ratio of 3:4. l and the spin quantum number s ($s = \pm\frac{1}{2}$) combine to the total angular momentum quantum number $j = l + s$. The degeneracy is $2j + 1$ which yields fixed area ratios between the two respective peaks. The area ratios for the different subshells are

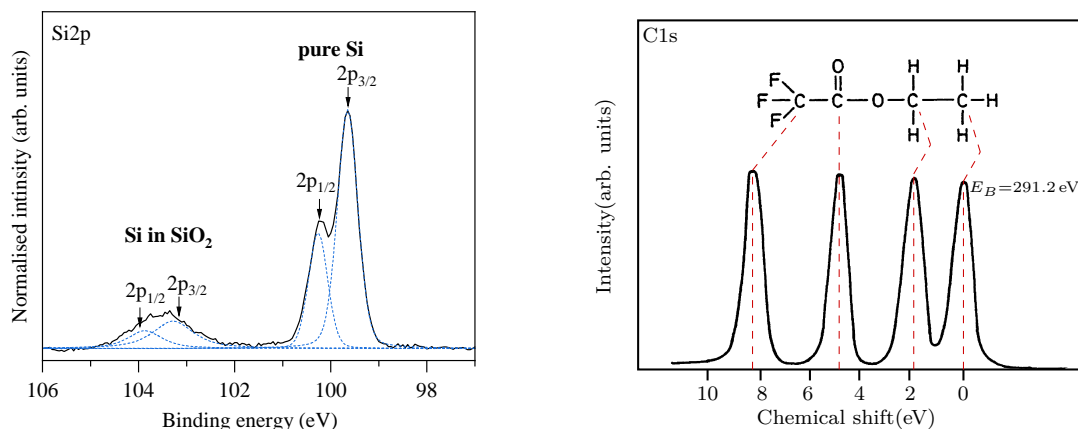


Figure 3.6: Examples for a chemical shift of core level spectra. Left: S 2p spectrum of a Si wafer covered with a 1-2 nm thin SiO₂ layer. Right: C 1s spectrum of ethyltrifluoroacetate in the gas phase. Taken from [137] which was originally adapted from [138].

Table 3.2: Area ratios of spin orbit-split doublets for the different subshells after [139].

subshell	angular momentum	spin	total angular momentum	area ratio
s	0	1/2	1/2	-
p	1	1/2	1/2 3/2	1:2
d	2	1/2	3/2 5/2	2:3
f	3	1/2	5/2 7/2	3:4

listed in table 3.2.

Final state effects are attributed to a violation of the Koopmans' theorem, thus stem from interactions between electrons after photoionisation. The escaping core level electron can interact with the remaining (N-1)-electron system in various ways (see Fig. 3.7). For example, it can transfer part of its energy to a valence electron, which is then excited to a former unoccupied state (shake-up process) or even completely emitted from the sample (shake-off process). This leads to a reduction of the kinetic energy of the photoelectron and hence to additional peaks at higher binding energies than the main core level peak, which are referred to as shake-up or shake-off satellites. Another example of a final state effect is the Auger process. Here, the core hole is filled by another electron from an outer shell, and the energy gained in this process is instantaneously transferred to another electron which is then emitted and detected. This is reflected in additional Auger lines that are independent from the exciting photon energy because the energy difference between orbitals is characteristic for each element. Auger lines are labelled by three letters denoting the initial core hole, the relaxing electrons initial state and the emitted electrons initial state.

Furthermore, the polarisability of the surrounding can lead to shifts in the binding energy. For example the core holes in molecules in direct contact with a metallic substrate are screened more efficiently than in molecules that are surrounded by other molecules [140].

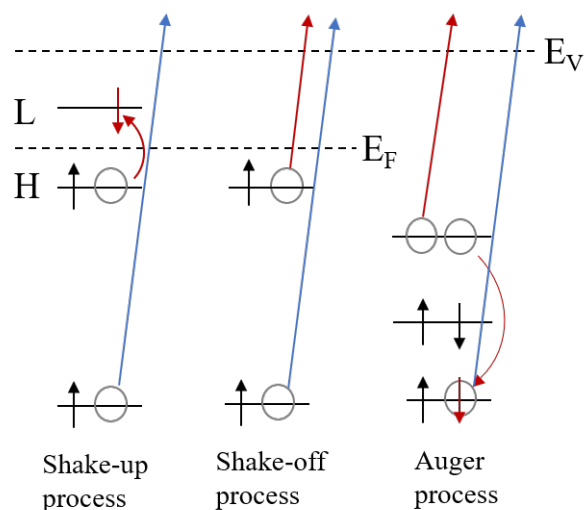


Figure 3.7: Interactions between photoelectron and (N-1)-electron system resulting in additional peaks in XPS spectra. In shake-up and shake-off process a valence electron is excited to an unoccupied state or emitted to the vacuum. In the Auger process an electron from an outer shell fills the core hole and transfers its gained energy to another electron which is emitted and detected as Auger electron.

Apart from the just described local effects, the measured binding energy of core (and valence) levels is also determined by changes in the global energetic landscape of the film. Analogous to inorganic semiconductors, the addition of electron acceptors or donors to an organic semiconductor film causes the Fermi level to shift towards the HOMO or LUMO level. This shift manifests itself in equal binding energy shifts of the core or valence levels.

Fermi level shift

Binding energy shifts do not always stem from local changes of the electronic environment around the molecule but also from shifts of the Fermi level. In analogy to the inorganic case, the addition of electrons to the LUMO or of holes to the HOMO of the organic semiconductor can lead to an immediate shift of the Fermi level even for relatively small concentrations of donors or acceptors. This manifests itself in equivalent binding energy shifts of core and valence levels. In some cases, it is useful to exclude the Fermi level shift from the analysis of photoemission spectra which can be achieved by plotting the spectra in dependence of the ionisation energy $IE = E_B + \Phi$ with the work function Φ determined from the HBEC position (see previous section).

Quantitative analysis of chemical composition

The peak area of a photoemission line is proportional to the amount of the respective atom in the sample. The peak area has to be weighted with the photoionisation cross section, a measure of the probability of photoionisation, which can differ significantly for different core level lines. Together with other factors that influence the intensity of detected photoelectrons, such as the angle between X-ray source and detector, the analyser's transmission function and the mean free path of photoelectrons in the sample a so called

atomic sensitivity factor (ASF) can be defined [139]. Obviously, ASF is specific for each element and photoemission setup. The numbers of atoms of two different elements, n_1 and n_2 , are then related to the peak areas of their respective core levels by the expression

$$\frac{n_1}{n_2} = \frac{A_1/ASF_1}{A_2/ASF_2} \quad (3.14)$$

n_1 and n_2 can also be two different species of the same elements that can be distinguished by different binding energies. To determine the ratio of two different molecules in a mixed film, numerator and denominator in eq. 3.2.3 need to be weighted by the number of respective atoms in the considered molecule. Due to the uncertainties from the fitting procedure and the preceding background subtraction the error of this procedure is estimated to be 20%.

3.3 Instrumental aspects

3.3.1 Energy reference

During a PES measurement, the sample is electrically connected to the spectrometer in order to avoid charging and the formation of a potential. As a result, the Fermi levels align. Since sample and spectrometer usually have different work functions, this leads to a step in the vacuum level, which is why the spectrometer detects the energy E'_{kin} instead of E_{kin} from Eq. 3.1. A diagram of the relevant energies for a PES measurement is shown in Fig. 3.8. The relation to the binding energy E_B of a photoelectron from a certain energy level in the material is given by

$$E'_{kin} = h\nu - E_B - \Phi_{spec} \quad (3.15)$$

From this it becomes clear that due to the alignment of the Fermi energies of sample and spectrometer, E_B relative to E_F is accessible without knowing the work function of the sample. By measuring a substance with a known binding energy, Φ_{spec} can be determined. For PES measurements it is advantageous to use metallic or highly doped semiconducting substrates, to avoid charging. For this reason and due to its inert chemical properties and easy handling, polycrystalline gold was mostly used as a substrate for the measurements that are presented in this work. For UPS, the spectra were shifted in such a way that the Fermi edge lies at $E_B=0$ eV. For XPS, the energy scale was calibrated by shifting the spectra so that the $Au4f_{7/2}$ is positioned at a $E_B=84.0$ eV [139].

3.3.2 Light sources

In PES, different photon sources are used depending on the requirements. To access the core level electrons, photon energies in the X-ray spectrum are necessary. For this, X-ray tubes with various anode materials that yield different emission lines are built into most PES setups. For the XPS measurements that are part of this thesis, exclusively AlK_α radiation was used with a photon energy of 1486.6 eV. In order to minimise the line width of the emitted radiation, a monochromator is integrated in the beam path which reduces the line width from about 0.9 eV to 0.3 eV.

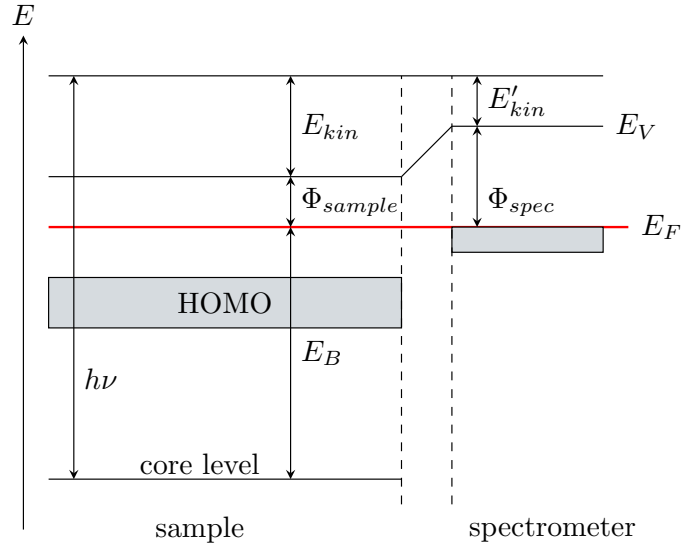


Figure 3.8: Scheme of the relevant energies of a (semiconducting) sample in contact with the spectrometer during a PES measurement. The detector measures E'_{kin} from which the binding Energy E_B relative to the Fermi level E_F can be determined taking into account the known work function of the spectrometer Φ_{spec} . Based on [137].

For measuring the electronic density of states in the valence region, smaller photon energies are sufficient. While this region is in principle also accessible with X-ray light, gas discharge lamps that emit in the UV region offer higher intensities and smaller line widths. The UPS spectra in this work were recorded using a He gas discharge lamp that emits photons of 21.21 eV due to a transition of the He($1s^1, 2p^1$) state to the ground state He($1s^2$). Besides this so called HeI $_{\alpha}$ transition, also HeI $_{\beta}$ (He($1s^1, 3p^1$) \rightarrow He($1s^2$)) and HeI $_{\gamma}$ (He($1s^1, 4p^1$) \rightarrow He($1s^2$)) transitions occur in the lamp but with much lower intensities. Since the UV photon source in the used setup does not comprise a monochromator, the UPS spectra need to be corrected for these so called satellite lines. This procedure is explained in more detail in Sec. 3.2.2.

3.3.3 Analyser and detector

In order to measure the intensity of photoelectrons with regard to their kinetic energy, an energy dispersive analyser and an electron detector are needed. The PES setups that were used in this work were equipped with hemispherical analysers with electron optical entrance lens systems and a multi channel plate. The electrostatic lens system decelerates the electrons and defines the acceptance angle from which the electrons are focussed onto the entrance slit. The analyser consists of two concentric half spheres with an adjustable electric potential between them, thus forming a capacitor. This serves as an energy filter since only electrons with a certain kinetic energy can pass the analyser to reach the detector without being deflected to the inner or outer hemisphere. In most PES systems, two measurement modes are available, the fixed retarding ratio (FRR) mode and the fixed analyser transmission (FAT) mode. In the FRR mode, the pass energy, which is defined by the potential between the inner and outer hemisphere, is scanned to obtain a spectrum. In the FAT mode, which was used for the spectra in this work, the electrostatic

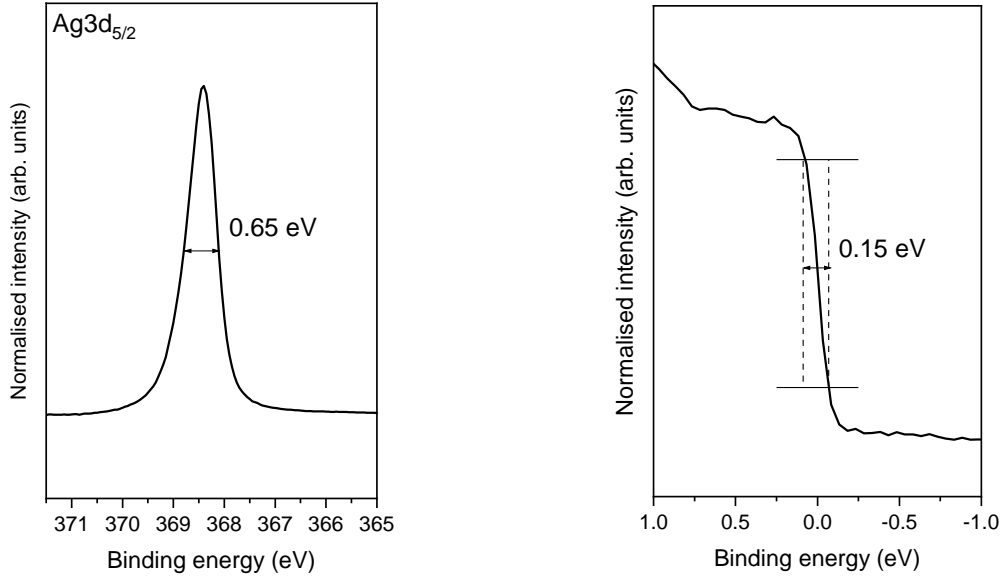


Figure 3.9: Left: XPS spectrum of the $\text{Ag}3d_{5/2}$ core level, measured with monochromatised $\text{AlK}\alpha$ radiation at a pass energy of 10 eV of a sputter cleaned silver sample. Right: UPS spectrum of the Fermi edge of a sputter cleaned silver sample, measured with 3 eV pass energy and a non-monochromatised He gas discharge lamp.

deceleration by the entrance lens is scanned over the desired energy range. The analyser transmission is fixed to a defined pass energy. This mode ensures a constant spectral resolution over the whole energy range. The energy resolution is given by

$$\frac{\Delta E}{E_{pass}} = \frac{S}{2r_0} + \frac{\alpha^2}{4}, \quad (3.16)$$

where S is the average slit width, α the acceptance angle of the electrons and r_0 the radius of the electrons trajectory. This illustrates, that for optimising the resolution, large radii, small slit widths and small pass energies are advantageous. For the spectra shown in this thesis, E_{pass} was chosen to be 3 eV for UPS and 10 eV for XPS measurements. The experimental energy resolution is determined by the analyser resolution and the photon source line width. The measured spectra can be described mathematically as a convolution of the real line shapes and a Gaussian which accounts for the experimental resolution. By convention, the width of the Fermi edge and the full width at half maximum (FWHM) of the $\text{Ag}3d_{5/2}$ peak, measured at a referential sputter cleaned silver sample is used as an estimation of the experimental resolution [141]. Fig. 3.9 shows an exemplary UPS spectrum of the low binding energy region of sputter cleaned silver (left) and the corresponding $\text{Ag}3d_{5/2}$ core level XPS spectrum (right), measured at room temperature and with pass energies and slit widths that were used for most spectra shown in this thesis.

As FWHM of the Fermi edge, the distance between the points in the spectrum where the intensity 14 % and 86 % of the total intensity is used. Accordingly, the energy resolution at the used experimental conditions is estimated to be about 0.65 eV for XPS and 0.15 eV for UPS.

The electrons are detected by the so called channeltrons, glass tubes, coated with a

secondary-emissive material with a high voltage (around 3 kV) applied along the long axis. When the photoelectrons hit the wall of the tubes, they create an avalanche of electrons which is then detected as an electric signal.

3.4 Experimental setup and sample preparation

All the spectra that are part of this work were recorded in two PES systems at the IFW Dresden. One is a spectrometer from the company SPECS GmbH, the other one from Physical Electronics. In both systems, the samples were prepared by thermal evaporation in ultra-high vacuum (UHV, base pressure about $2 \cdot 10^{-10}$ mbar) and could be transferred directly into a separate measurement chamber without breaking the vacuum. Despite differences in the geometric arrangement of the components, the working principle of both systems is very similar. In the following, only the SPECS setup will be described in more detail since it was the one where the majority of the data presented in this work was measured.

SPECS PES setup

The setup of the SPECS spectrometer system is shown in Fig. 3.10. It consists of two connected chambers at a base pressure of around $2 \cdot 10^{-10}$ mbar, a preparation chamber where the organic films are evaporated and a measurement chamber. The chambers are each evacuated by an own pump system and can be separated by a gate valve during evaporation to avoid contamination of the measurement chamber by organic materials. Samples can be transferred between both chambers by a transfer rod. A sample magazine allows the storage of five additional samples in the vacuum. The sample holders in both chambers can be heated by an electron beam heating up to 1000 °C. The sample manipulator in the measurement chamber additionally allows cooling of the sample with liquid helium as well as angle dependent measurements by rotating the sample with respect to the analyser. New samples are introduced via the fast entry chamber, which is evacuated to around $5 \cdot 10^{-8}$ mbar before the sample is transferred to the preparation chamber.

Before material evaporation, the substrate can be cleaned by Ar sputtering with a SPECS IQE 12/38 sputter gun which is installed at the measurement chamber. The organic materials are deposited on the substrate from Knudsen-type evaporators, up to three of which can be built into the preparation chamber. For subliming alkali metals, also the mounting of getter-type metal dispersers is possible. The film thickness is monitored during evaporation by a thickness monitor which is based on a quartz micro-balance. For PES measurements, a SPECS XR 50 M dual X-ray tube emitting AlK_α (1486.6 eV) and AgL_α (2984.3 eV) radiation and a SPECS UVS 300 He gas discharge lamp (HeI at 21.21 eV and HeII at 40.81 eV) are available. A monochromator is installed in the beam path of the X-ray source, while the UV lamp is not monochromated. For structural analysis a low-energy electron diffraction (LEED) system is also installed. The electrons are detected with a PHOIBOS 150 hemispherical analyser and a 9 channel channeltron detector.

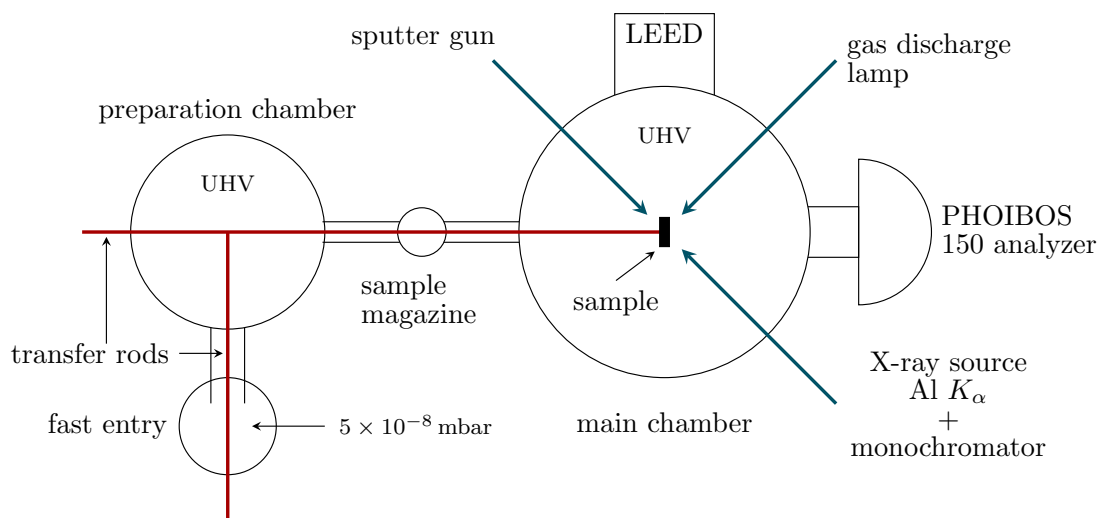


Figure 3.10: Scheme of the SPECS spectrometer system. Based on [137]

Sample preparation

For all analysed samples presented in this work, polycrystalline gold or silver foils were used as substrates. The preparation procedure was the same for both and will be described in the following.

Substrate cleaning

A suitable rectangular piece is cut from a metal foil and glued onto a stainless steel sample holder with a silver conductive adhesive. The sample is then loaded into the measurement chamber and sputtered for 10 to 30 min with Ar ions at an emission current of 7 to 10 mA. Subsequently, an XPS survey scan is recorded to ensure that the substrate is atomically clean. In addition, the $\text{Au}4f_{7/2}$ peak is measured as reference for the film thickness determination (cf. Sec. 3.2.3) and for the calibration of the XPS spectra to the $\text{Au}4f_{7/2}$ peak at 84.0 eV. A UPS spectrum is measured as well in order to calibrate the following valence spectra to the substrate Fermi edge at 0 eV binding energy (cf. Fig. 3.4).

Film evaporation

The organic materials used in this work were available in form of powder or flakes. For evaporation, the material was filled into ceramic crucibles and then mounted in the evaporator head. Prior to the film deposition, the material was heated up slowly in steps of around 10 K to evaporate any residual contamination. The crucible temperature was measured with a K-type thermocouple and regulated by a PID-controllers that were attached to the evaporator. After reaching the sublimation temperature of the material, the deposition rate and chamber pressure was monitored carefully for several minutes before placing the sample into the vapour cone in order to ensure a constant evaporation rate. The nominal rates for the films prepared for this work ranged between 0.2 and 0.5 nm min^{-1} . The samples were then placed in distances between 5 and 10 cm in front of the evaporator. The used crucible temperatures to achieve nominal evaporation rates of 0.2 to 0.5 nm min^{-1} and the respective pressures during the evaporation for each material

Table 3.3: Evaporation temperatures and pressures during evaporation of the used materials. The pressure in the preparation chamber before evaporation was around $2 \cdot 10^{-10}$ mbar when no evaporation was conducted for several days and could be up to $2 \cdot 10^{-9}$ mbar during a measurement series when two or more evaporation steps were done during one day.

material	evap. temperature range (°C)	pressure range during evap. (mbar)
F ₆ TCNNQ	210 - 270	$1 \cdot 10^{-8}$ - $8 \cdot 10^{-8}$
F ₂ TCNQ	150 - 170	$1 \cdot 10^{-8}$ - $1 \cdot 10^{-7}$
F ₁₆ CoPc	370 - 390	$1 \cdot 10^{-8}$ - $8 \cdot 10^{-8}$
DBP	270 - 300	$5 \cdot 10^{-9}$ - $5 \cdot 10^{-8}$
pentacene	210 - 240	$1 \cdot 10^{-8}$ - $1 \cdot 10^{-7}$
<i>trans</i> -[Ru(dppe) ₂ (T) ₂]	270 - 280	$4 \cdot 10^{-8}$ - $9 \cdot 10^{-8}$
ET	180 - 200	$8 \cdot 10^{-8}$ - $4 \cdot 10^{-7}$
CuPc	360 - 370	$2 \cdot 10^{-8}$ - $5 \cdot 10^{-8}$
C ₆₀	380 - 400	$1 \cdot 10^{-8}$ - $4 \cdot 10^{-8}$

investigated in this work are shown in table 3.3.

When a crucible was freshly filled with material, the evaporation temperature was often lower than after several evaporation cycles, which is why ranges of temperatures are given. Also the pressure did not stay constant during an evaporation or during several cycles which is why also here, rough ranges are given. The deposited film thicknesses were estimated after deposition by the attenuation of characteristic substrate core level peaks measured by XPS (see Sec. 3.2.3) and ranged, depending on the experiment, between 0.2 and 10 nm.

For the measurement of interfaces which were the main focus of this work, a thick film of the bottom material was deposited first. The aim was to achieve a film thickness thick enough so that no photoelectrons of the underlying metal substrate are detected in the UPS spectrum so that the spectrum only stems from the organic layer. This was usually the case for thicknesses larger than 2 nm. Following that, the second material was deposited stepwise with XPS and UPS measurements being conducted after each step. Initially, it was aimed for small steps of about 0.2 nm in order to achieve a large amount of molecules directly at the interface to contribute to the overall signal. When a top layer thickness of about 1 nm was reached, the deposition time for each step was increased until the spectra resembled that of pure film of the respective top material.

For the preparation of blends, the materials were first evaporated separately in order to find the respective optimal temperatures for a given evaporation rate. The reason for this was that only one thickness monitor, placed above the sample holder, was available in the used setups. Subsequently, both materials were evaporated simultaneously at the respective temperatures that were determined before. The mixing ratio was then estimated by analysing the core level peak area ratios (see Sec. 3.2.3).

During deposition, the substrate was at room temperature without active cooling. After

the evaporation, the sample was positioned away from the evaporator focus until the evaporator was cooled down below the sublimation temperature. Finally the sample was transferred to the measurement chamber.

Alkali metal doping

For the controlled doping of films with alkali metals, alkali metal dispensers of the company SAES Getters S.p.A. were mounted in the preparation chamber. The dispenser is a mixture of an alkali metal chromate and a reducing agent. The alkali metals were evaporated by resistive heating of the dispenser with a current between 4.5 and 6 A. Depending on the experiment, the alkali metal evaporation was conducted in steps of 20 to 60 s evaporation time. The dopant concentration was estimated by analysing the core level peak area ratios (see Sec. 3.2.3).

4 Results and discussion

4.1 The acceptor F₆TCNNQ

4.1.1 Potassium doping

Most of the interfaces and mixed films discussed in this work contain F₆TCNNQ as organic electron acceptor. Therefore, this chapter is started with the discussion of the photoemission spectra of pure F₆TCNNQ evaporated on a polycrystalline gold foil which was the standard substrate used for photoemission measurements. Furthermore, it seems reasonable to address the spectra of fully ionised F₆TCNNQ which represents the extreme case of full ionic charge transfer. To achieve this, the film is doped with potassium which, due to its small size, is expected to diffuse into the molecular film and transfer its 4s electron to F₆TCNNQ, forming a charge transfer salt (K⁺)(F₆TCNN⁻). It is aimed for a stoichiometric composition of (K₁)(F₆TCNNQ) which is determined, as described in Sec. 3.2.3, by comparing the areas of the K2p and C1s peaks weighted with the photoionisation cross sections [139] and the number of carbon atoms in F₆TCNNQ (C₁₆N₄F₆). Fig. 4.1 displays the XPS spectra of the C1s, N1s and F1s levels with the pure film spectra shown at the bottom and the doped film with a determined stoichiometry of (K_{0.9})(F₆TCNNQ) above. The film thickness determined by the attenuation of the Au4f core level was 8.5 nm. Note that the spectra are plotted in dependence of the ionisation energy (IE, see Sec. 3.2.2).

Beginning with the C1s spectrum of pure F₆TCNNQ, it comprises two peaks centred at 292.3 eV and 293.6 eV with the high energy flank decreasing less steeply than the low energy one. The 16 carbon atoms in F₆TCNNQ are bound to three different partners, other carbon atoms (6), nitrogen (4) and fluorine (6). Analogous to the similar molecule F₄TCNQ [142], the C-F bonds are assigned to the high ionisation energy peak due to the high electronegativity of fluorine and the C-C and C-N to the low energy peak. The spectrum could be fitted by three peaks with area ratios that reflect the ratio of the differently bound carbon atoms, C-C : C-N : C-F = 3 : 2 : 3. The asymmetric high energy flank is assigned to a shake-up satellite structure [143].

The N1s spectrum, shown in Fig. 4.1 (middle), consists of a main peak at 404.9 eV stemming from the nitrogen atoms that are all equally bound to carbon and a smaller one at 406.9 eV that can be assigned to a $\pi - \pi^*$ shake-up transition as well [143]. In the F1s region (right), a large peak at an ionisation energy of 693.7 eV and a small intensity satellite structure centred at 693.6 eV are detected.

Doping of the film by potassium leads to significant changes in all core levels. The C1s spectrum now comprises two peaks of more similar intensity and a shoulder at the high energy side. It is possible to fit this spectrum with two contributions with the same shape but different intensities and an energy difference of around 1.3 eV. Both contributions

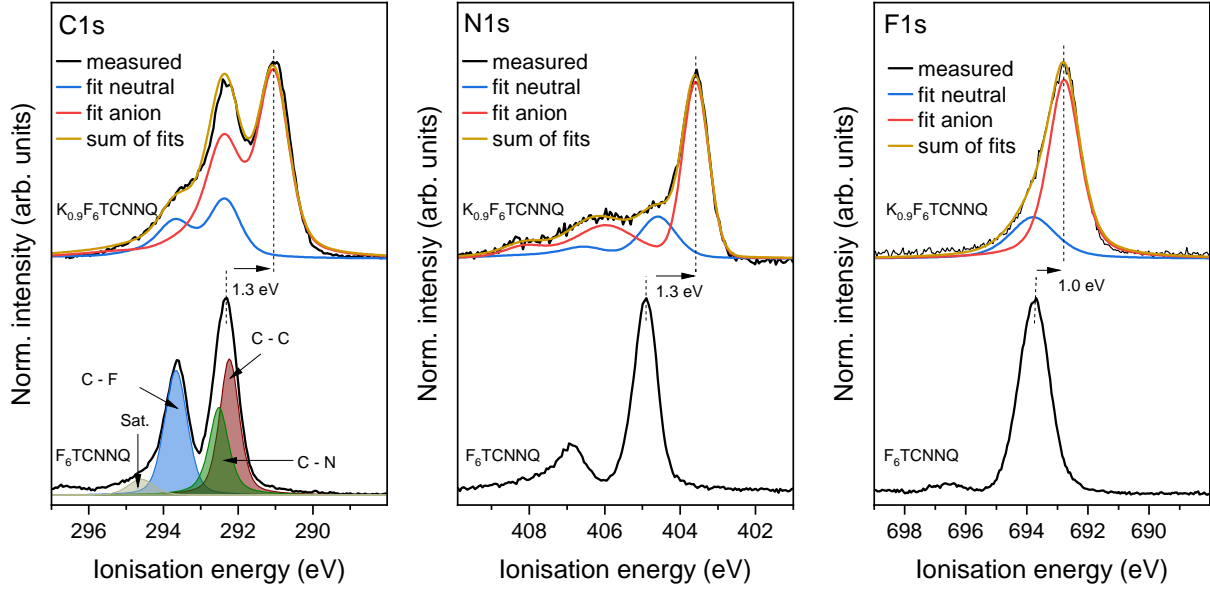


Figure 4.1: C1s (left), N1s (centre) and F1s (right) spectra of an F_6TCNNQ film (bottom) and of the same film after deposition of potassium (top). C1s spectrum can be fitted by 3 components reflecting the different carbon configurations in F_6TCNNQ and a satellite feature. Potassium doped F_6TCNNQ spectra comprise neutral (blue) and anionic contribution (red).

are broadened by about 50% compared to the neutral spectrum. The presence of a new species in the XPS spectrum is a clear sign of a charge transfer from K to F_6TCNNQ . The additional electron in the former LUMO leads to a stronger screening of the photohole in the core level and hence to a decreased ionisation energy. Accordingly, the low energy spectrum is assigned to anionic F_6TCNNQ molecules and the high ionisation energy one to molecules that remained neutral. The broadening of the spectra can be explained by structural inhomogeneities and disorder, induced by the insertion of potassium atoms between the molecules. This leads to a unequal electronic surrounding of the molecules which induces small binding energy changes which manifest themselves in a broadening of the core level peaks. The N1s and F1s spectra of $(K_{0.9})(F_6TCNNQ)$ are consistent to the C1s case. They can be fitted with a neutral contribution and an anionic one that is shifted by 1.3 eV in the N1s and 1.0 eV in the F1s case. For the N1s core level, the neutral contribution in the spectrum of K doped F_6TCNNQ is slightly shifted to lower energy compared to the spectrum of neutral F_6TCNNQ . This might be due to uncertainties in the background subtraction or the fitting procedure. Another explanation could be that in the K doped film, the presence of K atoms and charged molecules in the surrounding induces small binding energy shifts in the neutral N1s spectra due to the exposed position of the nitrogen atoms in the molecule. The area ratios between both species is 3.1:1 for all three core levels. This indicates that around 75% of the molecules in the measured region of the sample are negatively charged. The discrepancy to the stoichiometric composition of 0.9 K atoms per molecule is probably due to the uncertainty of the peak area analysis. It is also possible that there is a thin layer of potassium formed on top of the F_6TCNNQ film where the K atoms react with residual gas from the chamber.

The valence spectra of the same film recorded by UPS are shown in Fig. 4.2. Starting

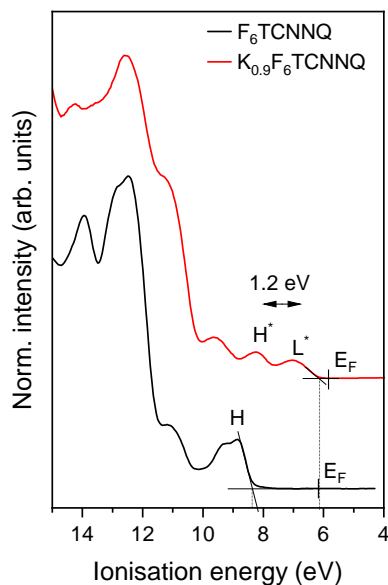


Figure 4.2: UPS spectra of the valence region of an F₆TCNNQ film (bottom) and of the same film after deposition of potassium (top). H denotes HOMO of the pure film, H* and L* denote former HOMO and the former now half filled LUMO.

with the spectrum of neutral F₆TCNNQ, the first HOMO derived feature has an onset of 8.35 eV, which is 2.2 eV below the Fermi level. The published value for the optical gap which constitutes a lower limit for the transport gap (cf. Sec. 2.1) is approx. 2.4 eV [99, 144], hence, the Fermi level lies close to the LUMO of F₆TCNNQ. Upon potassium doping, the spectrum changes drastically. The new HOMO has an onset at 6.14 eV which is only 0.31 eV below the Fermi level. The energetic distance to the next lower orbital (HOMO-1) is approx. 1.2 eV. If a full integer charge transfer is considered, the new HOMO is the now singly occupied former LUMO and the HOMO-1 is the former HOMO. The original HOMO-LUMO distance of at least 2.4 eV is reduced to 1.2 eV due to a deformation of the molecule upon negative ionisation. The molecule now comprises a negative polaron (see Sec. 2.2). The energetic position of the frontier orbitals is in good agreement to density functional theory (DFT) calculations of the density of states of an isolated F₆TCNNQ anion [105]. The just stated interpretation of integer charge transfer assumed the formation of a (K₁)(F₆TCNNQ) phase. Theoretically, also a coexistence of areas with a (K₂)(F₆TCNNQ) phase and areas with pure F₆TCNNQ can lead to the measured composition of (K_{0.9})(F₆TCNNQ). The good conformity of the UPS spectra with published DFT calculations and the comparison of the XPS spectra with other F₆TCNNQ based charge transfer systems (discussed in the following sections) leads us to the conclusion that F₆TCNNQ is singly ionised.

4.1.2 Interface to polycrystalline gold

In this section, the interface between F_6TCNNQ and the polycrystalline gold substrate, which was mostly used in in this work, is investigated. Interfaces between metals and organic semiconductors are of scientific interest due to their technical importance in applications, such as light emitting diodes and photovoltaic cells. Previously, a charge transfer reaction between the similar molecular acceptor F_4TCNNQ and gold was reported which enabled tuning the barrier for hole injection into a subsequently deposited organic semiconductor [145]. All spectra that are discussed in the following were published in Ref. [146].

As elaborated in Sec. 3.4, F_6TCNNQ was evaporated stepwise onto the gold substrate and core and valence levels were measured after each step. Sputter cleaned gold foil usually has a work function of around 5.0 eV which is in the same range as the reported electron affinity of F_6TCNNQ between 5.0 and 5.6 eV [88, 89], which makes a charge transfer from gold to F_6TCNNQ energetically favourable. The XPS spectra are displayed in Fig. 4.3 in dependence of the ionisation energy, analogous to the previous section.

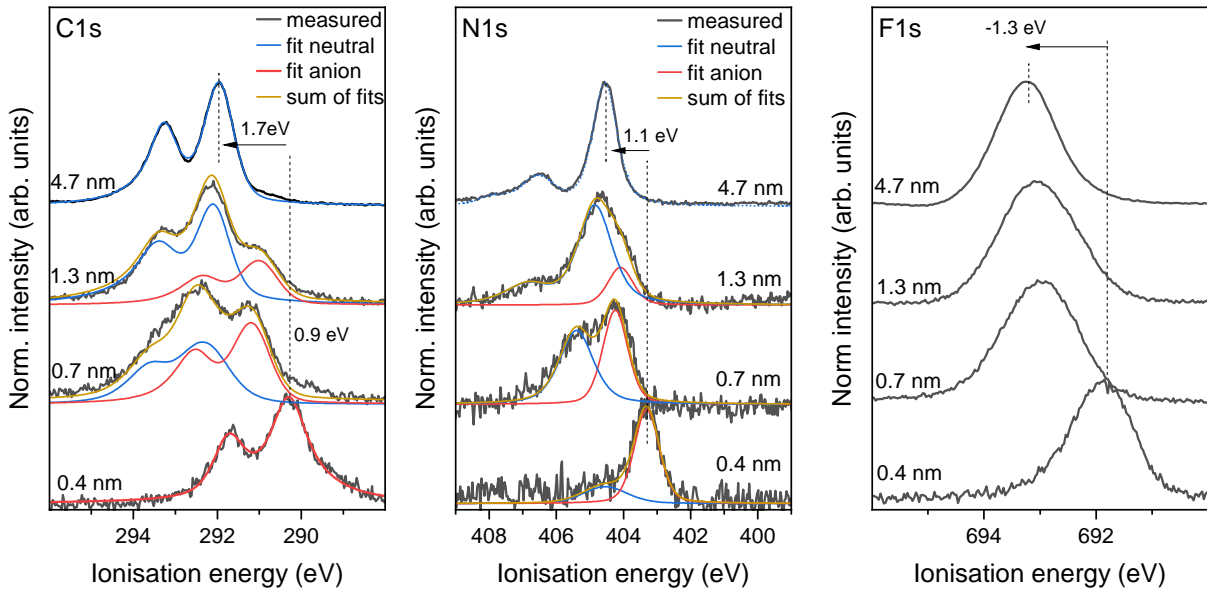


Figure 4.3: C1s (left), N1s (centre) and F1s (right) spectra of F_6TCNNQ deposited stepwise on a sputter cleaned polycrystalline gold foil. C1s and N1s spectra comprise a neutral contribution (blue) and another contribution that is attributed to negatively charged F_6TCNNQ and the interface.

The topmost spectra are in accordance to the spectra of pure F_6TCNNQ in the in the previous section indicating that no electronically affected molecules are detected at a thickness of 4.7 nm. Going to smaller film thicknesses, the contribution of molecules in the interface region to the overall signal increases. In the C1s case (left panel), a second double peak structure appears (red) at lower ionisation energy and gets stronger in intensity until for a thickness of 0.4 nm the spectrum comprises only this structure. It is attributed to negatively charged F_6TCNNQ . The N1s spectra (middle panel) progress in a similar manner with a second peak at lower energy appearing at in the interface region. A $\pi - \pi^*$ shake-up satellite which is present in the neutral spectrum around 2 eV

above the main feature is not clearly resolved which might be due to the smaller signal to noise ratio compared to the thick potassium doped film in the previous section. Finally, the F1s spectra (right panel) do not show an obvious second species in the interface region. Instead, only a slight asymmetry of the peak with a flank on the low energy side is visible for the 0.7 and 1.3 nm films indicating the presence of a second species.

It is apparent that the anion spectra broaden with increasing film thickness. On the other hand, the width of the neutral spectra decrease with increasing film thickness. This behaviour can be rationalised by structural changes of the molecular arrangement. It is known that many organic molecules tend to lie flat on metal surfaces [147, 148], in particular in case of a charge transfer, also structural deformations of the molecules in close proximity to the metal surface can occur as has been shown for F₄TCNQ [149, 150]. After the first monolayer, the film structure gradually shift towards a more upright standing structure. Since the core level ionisation energy is sensitive to the electronic surrounding, it can differ depending on the morphology of the film. Consequently, for intermediate film thicknesses, when core electrons from molecules from the first layer and from the following layer are detected, the spectra are broadened due to small differences in binding energy. For large film thickness, only electrons from standing molecules are emitted from the film leading to sharper spectra.

The ionisation energy difference between neutral and anionic spectrum is 1.7 eV for C1s, 1.1 eV for N1s and 1.3 eV for the F1s level. While these differences are also sensitive to structural changes in the film morphology, also the spatial distribution of the frontier orbitals affect the core level ionisation energy. DFT calculations of F₆TCNNQ deposited on ZnO [151] and of the similar acceptor F₄TCNQ on various metals [149] show a complex interplay between charge forward and backward donation and strong adsorption induced geometry changes. Thus, a more detailed analysis of all core level shifts in the present system would require further methods for structural analysis and calculations which is beyond the scope of this work.

We continue the discussion with the UPS data, shown in Fig. 4.4. The left panel shows the spectrum of the 0.7 nm thick film. Since it is a superposition of the gold substrate spectrum and the spectrum stemming from the deposited film it is useful to subtract the substrate spectrum after rescaling it so that the Fermi edges of both spectra are aligned. Fig. 4.4 (middle) shows the resulting difference spectra for increasing film thickness together with the spectrum of (K_{0.9})(F₆TCNNQ) as reference. It becomes apparent that the spectra for low film thicknesses look similar to the spectrum of (K⁺)(F₆TCNNQ⁻), whereas with increasing thickness the spectra resemble more and more the structure of the neutral F₆TCNNQ known from the last section (Fig. 4.2). Apparently, the nature of the charge transfer is very similar for both cases. The energetic separation between the now singly occupied LUMO centred at 7.2 eV and the former HOMO, now HOMO-1, at 8.4 eV is the same as in the (K_{0.9})(F₆TCNNQ) case, thus the polaronic relaxation of the frontier orbitals is apparently equal. The small variations in intensity of the three first peaks could be attributed, in analogy to the core level spectra, to differences in the molecular arrangement between the thin charged film at the gold interface and the thick film doped with potassium.

Finally, the progression of the work function, depicted in the right panel of Fig. 4.4 is discussed. The work function of the substrate (data point at 0 nm film thickness) is

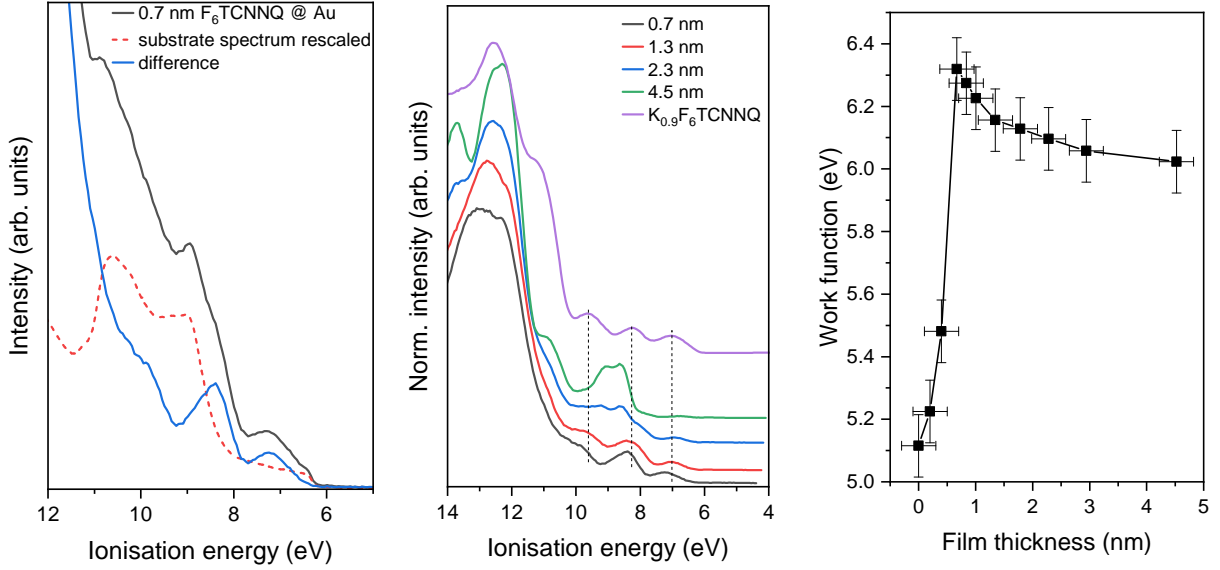


Figure 4.4: UPS spectra and work functions of F_6TCNNQ /gold interface. Left: Subtraction of substrate spectrum from overall spectrum yields the difference spectrum reflecting only the signal stemming from the F_6TCNNQ film. Middle: UPS valence spectra of F_6TCNNQ deposited stepwise on a sputter cleaned polycrystalline gold foil after subtraction of the pure substrate spectrum. The spectrum of potassium doped F_6TCNNQ is shown in purple for comparison. Right: Work function in dependence of film thickness of F_6TCNNQ deposited stepwise on a sputter cleaned polycrystalline gold foil. Solid line is guide to the eye.

5.1 eV. Deposition of F_6TCNNQ leads to a drastic increase of the work function by 1.2 eV already for the first 0.7 nm of coverage. This phenomenon is common for the deposition of acceptors on metal surfaces and is referred to as interface dipole. It is a result of an electron transfer from the metal to the first molecular layers which leads to the formation of a narrow space charge region (cf. Sec. 2.3). For increasing film thicknesses the work function decreases slightly from 6.3 eV to 6.0 eV. This is a further indication for a change of the film morphology after the first monolayer is completed. The energy level alignment, deduced from the UPS measurements is shown schematically in Fig. 4.5.

In summary, it was shown in this section that an ionic charge transfer is taking place at the interface between gold and F_6TCNNQ . It displays very similar spectroscopic signatures as the potassium doped film. Energetic shifts and the progression of the work function indicates that the film morphology is different at the interface than for the multilayered film. In the next section, various interfaces between F_6TCNNQ and other organic semiconductors are discussed.

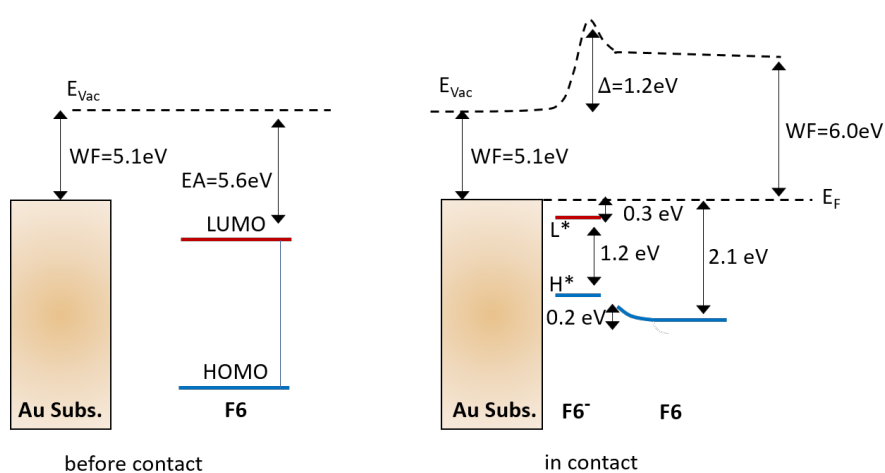


Figure 4.5: Schematic illustration of the energy level alignment at the F₆TCNNQ/gold interface before and after contact. Molecules at the interface get reduced which leads to a polaronic relaxation. The now singly occupied LUMO is denoted L* and relaxed former HOMO H*.

4.2 F₆TCNNQ based organic heterostructures

After having established an understanding of probing charge transfer at an organic/metal interface, we will proceed to purely organic interfaces. The first part of this chapter will deal with the interfaces between F₆TCNNQ and the two prototypical polycyclic hydrocarbons pentacene and 1,2:8,9-dibenzopentacene (DBP). This is followed by a study of the charge transfer characteristics between F₆TCNNQ and a ruthenium acetylide complex, a large molecule which is a building block for conducting polymers. Finally, the organosulfur compound Bis-(ethylenedithio)-tetrathiafulvalen (BEDT-TTF or ET), which is an electron donor for a family of organic conductors and superconductors is used to form charge transfer interfaces to F₆TCNNQ and the smaller similar acceptor F₂TCNQ. Both systems are compared and investigated in terms of a possible metallic state at the interface.

4.2.1 Polycyclic hydrocarbons

Interface

Pentacene is a polycyclic hydrocarbon (PCHC) that has been scientifically investigated especially as a potential material for organic transistors due to its relatively high charge carrier mobility of $35\text{ cm}^2\text{ V}^{-1}\text{ s}^{-1}$ in single crystalline and $0.6\text{ cm}^2\text{ V}^{-1}\text{ s}^{-1}$ in thin film form at room temperature [152, 153]). The bulk p-doping of pentacene with F₄TCNQ [154] and F₆TCNNQ [155] is reported in literature. Furthermore, the interface between pentacene and F₄TCNQ was investigated with PES and did not show signs of a charge transfer [156]. In the following, the interface between pentacene and F₆TCNNQ is investigated and compared to the interface of DBP and F₆TCNNQ. There are two motivations for this study. On the one hand, the interface between the polycyclic hydrocarbon rubrene and the acceptor type phtalocyanine F₁₆CoPc shows metallic conduction properties which were attributed to the realisation of a 2-dimensional hole gas at parts of the interface [18]. A heterojunction with the aforementioned material combinations could lead to interesting results in this regard. On the other hand, a comparison between the pentacene and DBP interfaces could provide information about the influence of the structural difference on the charge transfer characteristics. DBP has the same backbone as pentacene with two additional benzene rings at the 1,2 and 8,9 position but shows a quite similar electronic structure near the Fermi level [157]. The following results were published in Ref. [158].

In the following discussion, the XPS results are presented in a four panel arrangement, showing the F₆TCNNQ/pentacene interface on the bottom and the F₆TCNNQ/DBP interface on top with the deposition sequence with F₆TCNNQ as bottom layer on the left and the reverse sequence on the right panel, respectively. The C1s core level spectra are depicted in Fig. 4.6. The spectra of the respective pure materials are shown as black lines in each panel. The F₆TCNNQ spectrum consists of the characteristic double peak structure which was already discussed in Sec. 4.1.1. The PCHC's C1s signal comprises one broad peak with the maximum at 288.5 eV and the same width which agrees with spectra reported in literature [159, 160]. This is expected, since the carbon atoms in pentacene and DBP occur in six different configurations, regarding the number of bonds

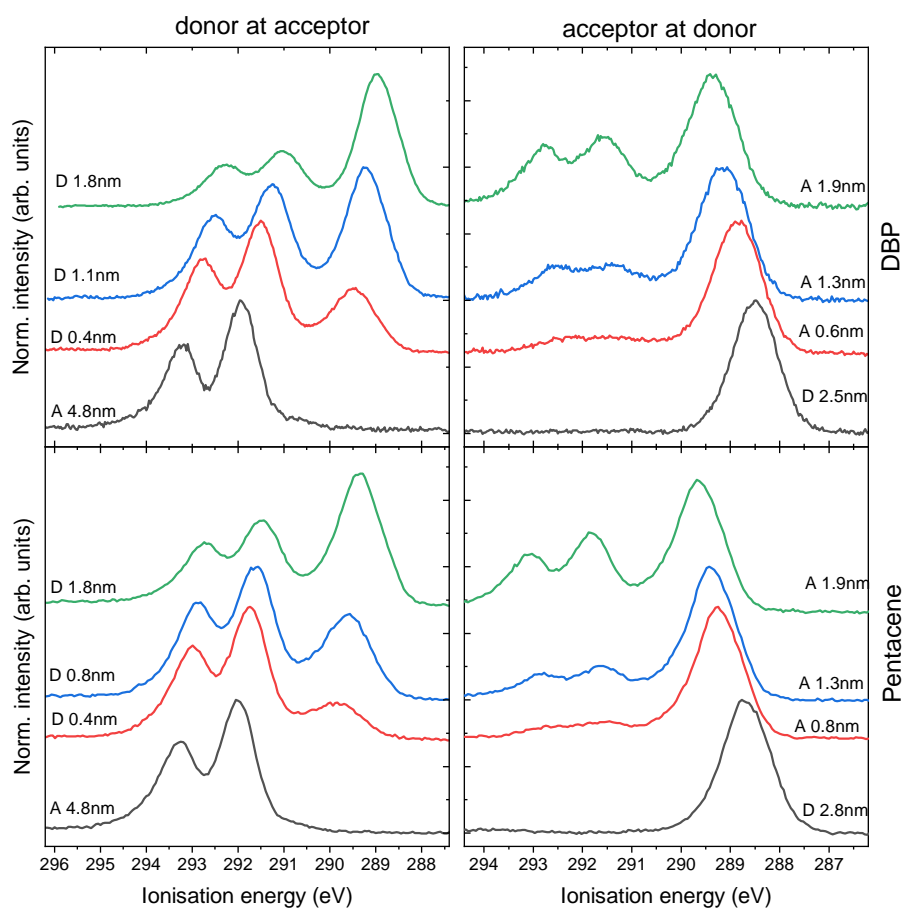


Figure 4.6: C1s photoemission core level spectra of interfaces between pentacene (bottom row) and dibenzopentacene (DBP) (top row) and F₆TCNNQ for an increasing top layer thickness. The left panels show F₆TCNNQ (A) as the bottom layer with stepwise deposition of the PCHCs (D) on top. The right panels the opposite deposition sequence with the PCHCs at bottom layers. Taken from [158].

to carbon and hydrogen, which only differ slightly in their respective binding energies, resulting in a single broad peak. With the deposition of the second material, a shift of the respective C1s features is observed. For the sequence where F₆TCNNQ is the top layer (right column), the PCHC as well as the F₆TCNNQ features shift to higher ionisation energies. For the reversed sequence (left column) they shift to the opposite direction. Assuming a charge transfer at the interface, the thin film system would be built up from bottom to top in the following way:



or vice versa. This leads to an alignment of the Fermi levels in both materials at the interface which is compensated by a vacuum level shift which results in an increase of the work function for the sequence with F₆TCNNQ as top layer and a decrease for the opposite sequence. The surface sensitivity of PES leads to a shift of the "information window" across the interface region. Accordingly, the C1s spectra shift to higher ionisation energies for F₆TCNNQ@PCHC sequence and to lower ones for the reverse sequence. The analogous behaviour is observed in the F1s core level spectra, shown in Fig. 4.7. The peak shape of the F1s feature remains unchanged, which is not surprising because according to DFT calculations, the LUMO of F₆TCNNQ is located predominantly at the carbon and nitrogen sites and less at the fluorine sites of the molecule [150, 151, 161].

Going back to the C1s spectra (Fig. 4.6), the feature associated with the PCHC is hardly changing. As mentioned before, it consists of six different overlapping carbon species. The change in peak shape induced by an additional charge on the molecules in the interface region is probably too small to be detected with the used setup. Looking at the F₆TCNNQ spectra, no change in peak shape is apparent for the sequence with F₆TCNNQ as bottom layer (left column). For the opposite deposition sequence however, a deviation from characteristic intensity ratio of the two peaks is observable, especially for the 1.3 nm coverage (blue curves, right column). These spectra cannot be reproduced by a simple superposition of both neutral spectra. A detailed peak fitting is not possible due to the many different carbon species in both the acceptor and donor molecules. However, in order to gain a qualitative understanding of the interface spectra, the pure spectra of thick (neutral) donor and acceptor films are subtracted from the measured C1s spectra. As shown in Fig. 4.8, the pristine spectra are adjusted in intensity and shifted in energy so that the pristine F₆TCNNQ spectrum is aligned to the high energy flank of the measured interface spectrum and the pristine donor spectrum is aligned to the low energy flank. Obviously, the C1s peaks stemming from the PCHCs cannot be fitted by solely the neutral spectrum since they are too broad. Hence, the neutral spectra were scaled to lower intensity and shifted by 0.7 eV for pentacene and 0.6 eV for DBP to account for the assumed oxidised PCHC spectra. This assumption neglects a possible structure induced broadening or peak shape changes due to an uneven HOMO distribution over the PCHCs, but seems sufficient for the purpose of a qualitative analysis. Subtraction of neutral F₆TCNNQ, neutral and oxidised PCHC spectra from the measured spectra yields difference spectra (red curves in Fig. 4.8) which are attributed to reduced F₆TCNNQ at the interfaces. Their spectral shape is different to the neutral F₆TCNNQ spectrum in that the intensities of the two peaks are almost even and the low energy peak is broader. Interestingly, they are similar to a previously measured F₆TCNNQ⁻ spectrum at an interface to manganese phthalocyanine (MnPc) [162], which had a similar shape, intensity

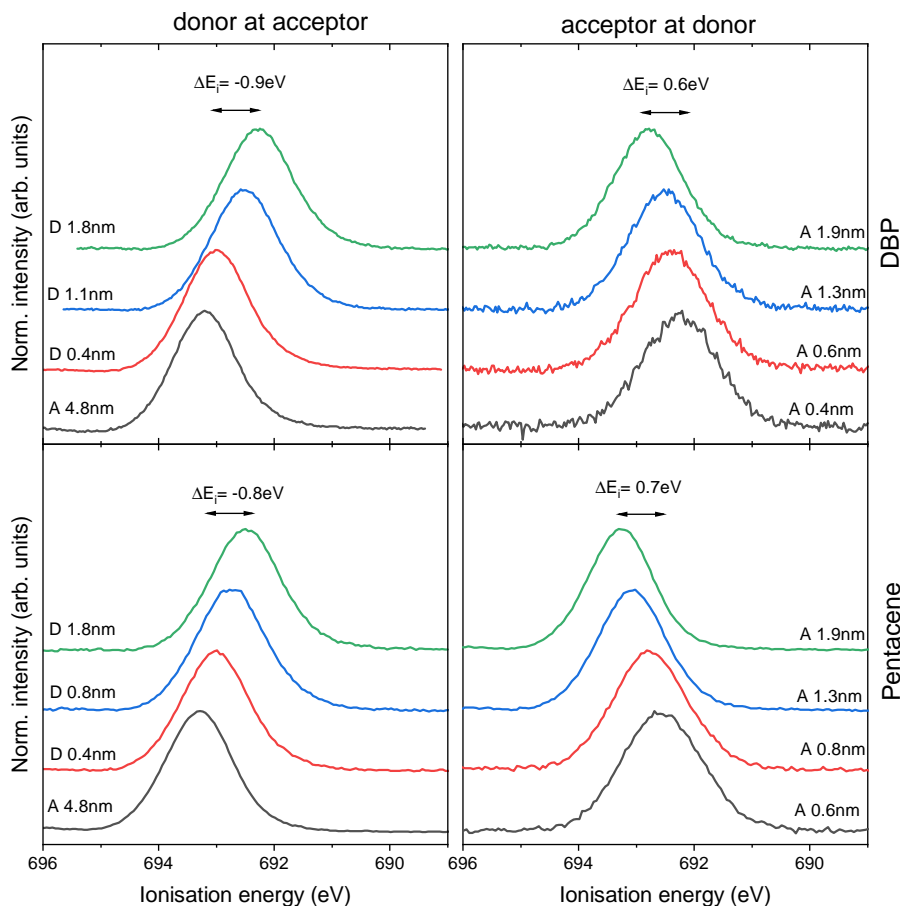


Figure 4.7: F1s photoemission core level spectra of interfaces between pentacene (bottom row) and dibenzopentacene (DBP) (top row) and F₆TCNNQ for an increasing top layer thickness. The left panels show F₆TCNNQ (A) as the bottom layer with stepwise deposition of the PCHCs (D) on top. The right panels show the opposite deposition sequence with the PCHCs at bottom layers. Taken from [158].

ratio and energy difference between the two peaks.

As discussed in Sec. 4.1.1 (Fig. 4.1), the high energy peak stems from the carbon atoms bound to fluorine and the peak at lower energy comprises two contributions, one from the carbon atoms bound to nitrogen and the other one from carbon bound to other carbons. Fig. 4.9 shows a comparison between the C1s spectrum of neutral F₆TCNNQ and the interface spectra taken from the subtraction procedure in Fig. 4.8. It becomes apparent that in the interface spectra all species are broadened and the C-N contribution is shifted to higher energy while the C-C contribution is shifted to lower energy (more strongly for F₆TCNNQ/DBP). This either indicates that the additional charge is not evenly distributed over the molecule which is a sign of hybridisation. The other possible explanation is a different arrangement of the F₆TCNNQ molecules in the interface region compared to the "bulk". Molecular orientation can lead to binding energy shifts up to a couple hundreds of meV [80]. The fact that the C1s spectra for higher F₆TCNNQ thicknesses on the PHCH's looks identical to the thick films on gold shows that after the first couple of layers, the molecules arrange in the same manner as on the pristine gold substrate. Interestingly, the C1s interface spectrum of F₆TCNNQ/gold,

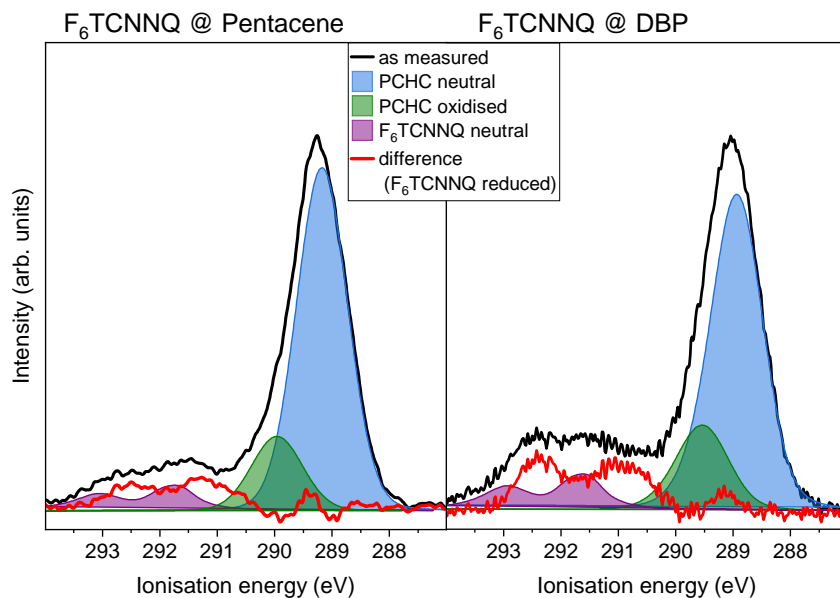


Figure 4.8: Qualitative analysis of the C1s spectra of F₆TCNNQ on PCHCs to verify the existence of anionic F₆TCNNQ. The measured interfaces have an estimated thickness of the acceptor top layer of approximately 1.3 nm. The plot shows the measured curve (black) of the heterojunction, the pristine spectra of F₆TCNNQ (green), and the superposition of the neutral donor molecule and its cation (blue). It is assumed that the cation has the same shape and is only shifted to higher binding energies. The difference spectrum (red) is attributed to the acceptor anion. Taken from [158].

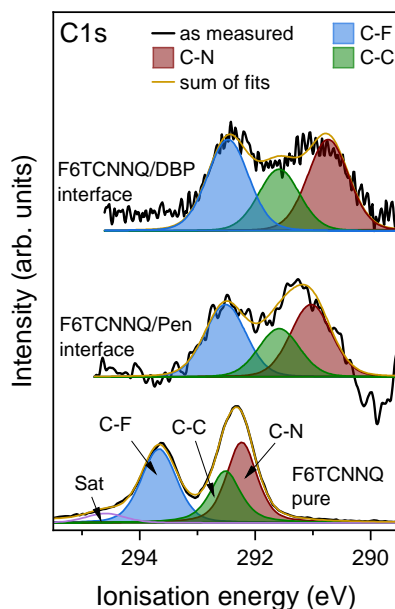


Figure 4.9: Qualitative comparison between C1s spectra of neutral F₆TCNNQ and F₆TCNNQ at the interfaces to pentacene and dibenzopentacene. Peak areas ratios reflect quantitative ratio of configurations of carbon atoms in F₆TCNNQ (C-C:C-F:C-N = 3:3:2).

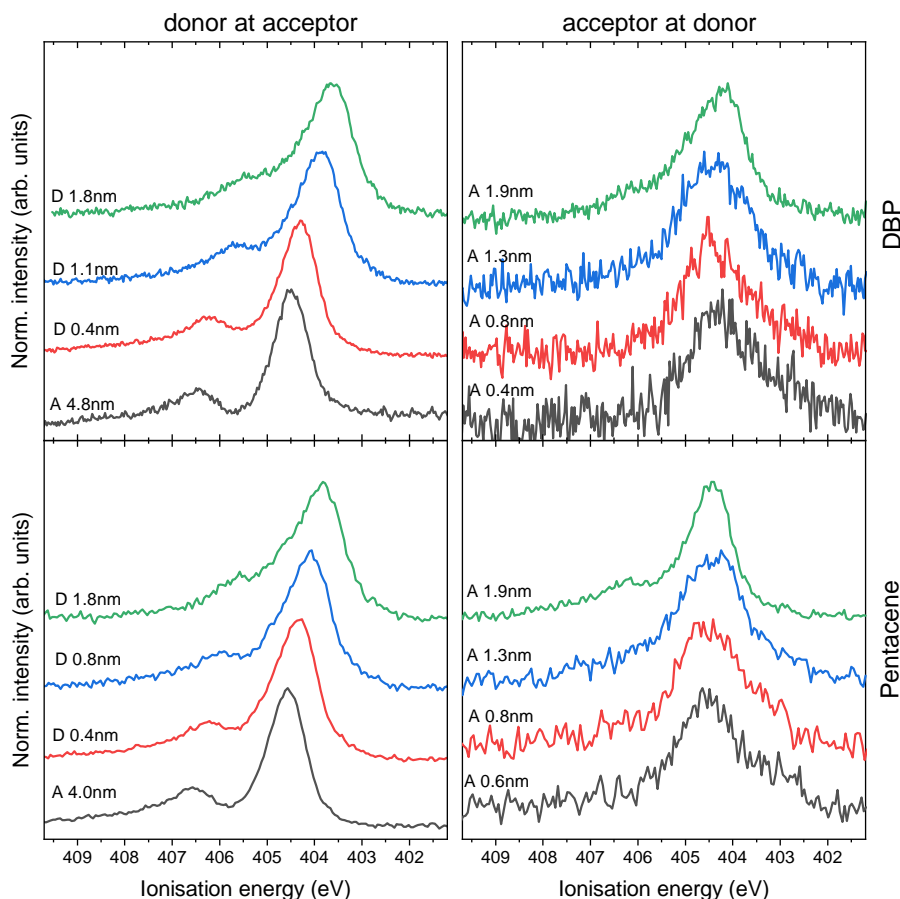


Figure 4.10: N1s photoemission core level spectra of interfaces between pentacene (bottom row) and dibenzopentacene (DBP) (top row) and F₆TCNNQ for an increasing top layer thickness. The left panels show F₆TCNNQ (A) as the bottom layer with stepwise deposition of the PCHCs (D) on top. The right panels show the opposite deposition sequence with the PCHCs at bottom layers. Taken from [158].

discussed in Sec. 4.1.2 and that of potassium doped F₆TCNNQ (Sec. 4.1.1) did not show these changes which indicates that either the type of charge transfer (ionic vs. hybridisation) or the molecular orientation is different at F₆TCNNQ/PCHC interfaces.

Further information might be gained by analysing the N1s spectra of the interfaces, shown in Fig. 4.10. Note that the PCHCs do not comprise nitrogen, which is why the stacked spectra start with the first deposition step of F₆TCNNQ. For the PCHC@F₆TCNNQ sequence the bottom spectra (left column, red) show the pristine N1s peak with the shake-up satellite, which is in agreement with the spectra discussed before (Sec. 4.1.1). With increasing PCHC thickness, a shift to lower ionisation energies (analogous to the C1s and F1s spectra) and a broadening can be observed. The broadening indicates the presence of at least one additional species at the interface. For the reverse sequence, a shoulder at the low ionisation energy side is visible for low F₆TCNNQ coverages which decreases in intensity with increasing thickness. Moreover, the spectra show a clearly asymmetric shape up to 1.9 nm top layer thickness. The position of the shoulder at around 403.3 eV has roughly the same energy distance to the neutral peak

at 404.5 eV as the N1s anion spectrum found for the $(\text{K}^+)(\text{F}_6\text{TCNNQ}^-)$ ($\Delta E=1.0$ eV) and the $\text{F}_6\text{TCNNQ}/\text{Au}$ ($\Delta E=1.1$ eV) systems. This leads us to the conclusion that this feature can be attributed to anionic F_6TCNNQ at the interface. The share of the anion feature to the overall spectra at low F_6TCNNQ coverage is very small, whereas for the $\text{F}_6\text{TCNNQ}/\text{Au}$ interface the spectrum comprised almost exclusively the anion signature at a comparable film thickness. An explanation for this could be again the orientation of the molecules which has a strong influence on the charge transfer ability at a molecular heterojunction [163]. If the first layers of F_6TCNNQ arrange randomly on the PCHC bottom layer, only a fraction of the molecules exchange charges which is reflected in the core level spectra.

Finally, the valence spectra recorded by UPS are shown in Fig. 4.11. The ionisation

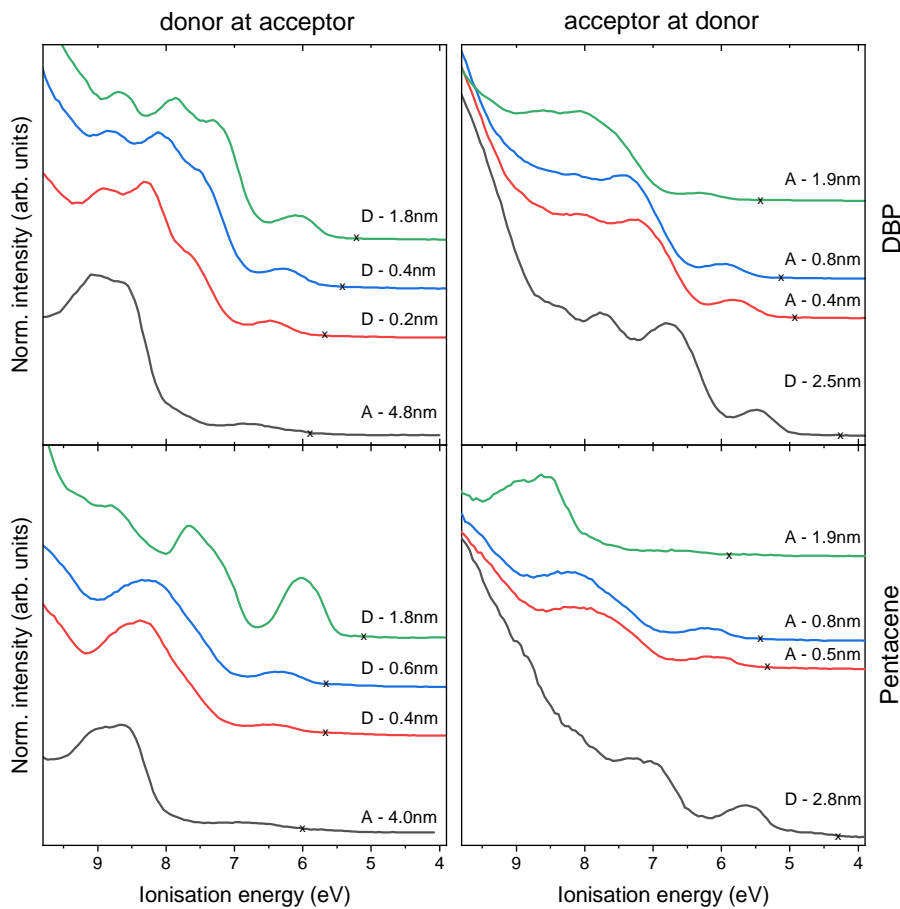


Figure 4.11: UPS spectra of the valence region of interfaces between pentacene (bottom row) and dibenzopentacene (DBP) (top row) and F_6TCNNQ for an increasing top layer thickness. The left panels show F_6TCNNQ (A) as the bottom layer with stepwise deposition of the PCHCs (D) on top. The right panels show the opposite deposition sequence with the PCHCs at bottom layers. The layer thicknesses, determined by the substrate signal attenuation, are indicated. Taken from [158].

potentials of both materials, determined by the HOMO onsets both lie at around 5.0 eV. With increasing top layer thickness, the respective peaks of the top layer grow

in intensity until at a thickness of around 2 nm the spectra mainly comprise the top layer features (black spectra in left panels look similar to green spectra in the right panels). No sign of the F₆TCNNQ anion spectrum, known from the Au/F₆TCNNQ and (K⁺)(F₆TCNNQ⁻) systems is detected. This is not surprising since only a small fraction of molecules is ionised according to the XPS spectra. Furthermore, the occupied LUMO of F₆TCNNQ is overlapped by the HOMO of the PCHC's. The hole injection barrier of the PCHCs (energy of HOMO onset relative to Fermi level) is reduced by about 0.5 eV upon deposition of 1 nm of F₆TCNNQ. This is analogous to p-doping in inorganic semiconductors which leads to a shift of the Fermi level towards the valence band. However, no valence spectrum in the series shows signs of occupied states directly at the Fermi level (black crosses in Fig. 4.11), which indicates semiconducting properties of all interfaces and a localised charge transfer.

Summarising, spectroscopic evidence for a charge transfer at both interfaces was found. The anion spectra in the C1s and N1s core levels are more strongly pronounced in the F₆TCNNQ/DBP interface which indicates that more molecules are ionised. Since the ionisation potentials of both PCHC's are equal, the different interface morphology must be responsible for the slightly more strongly pronounced charge transfer at the F₆TCNNQ/DBP interface. Apart from that, both systems did not show signs of hybridisation or new electronic states at the interface which suggests that the structural difference between pentacene and DBP does not have a strong influence on the charge transfer properties. The C1s anion spectrum of F₆TCNNQ has a different shape and intensity ratio than the anion spectrum known from F₆TCNNQ/gold and (K⁺)(F₆TCNNQ⁻). The absence of signs of hybridisation in the UPS spectra supports the hypothesis that this is due to structural effects rather than a charge transfer complex formation. The interfaces both do not show signs of "metal-like" electron delocalisation. In the next section, a co-evaporated blended film of F₆TCNNQ and DBP is investigated in terms of possible charge transfer reactions.

Mixed film

To further investigate the charge transfer between F₆TCNNQ and dibenzopentacene (DBP), both materials were evaporated simultaneously with the aim of achieving a blend with a 1:1 stoichiometry. Co-evaporating donor and acceptor molecules can result in the formation of a charge transfer salt with electronic properties that differ significantly from those of the individual constituents (cf. Sec. 2.2). The molecular ratio was determined as approx. 1:1 by comparing the C1s peak areas of both molecules, weighted with the number of carbon atoms per molecule. After measuring XPS and UPS spectra of the mixed film, it was annealed at a temperature of 100 °C for 1 h. The XPS core level spectra of the mixed film directly after co-evaporation and after annealing are shown in Fig. 4.12. As a comparison, also spectra of films of the pristine materials and the referential charge transfer salt potassium doped (K⁺)(F₆TCNNQ⁻) (cf. Sec. 4.1.1) are depicted. In analogy to the interface spectra in the previous section, the spectra are shown in dependence of the ionisation energy.

Starting with the C1s spectrum of the mixed film (light red curves), several changes to the pristine spectra are apparent. The double peak structure of F₆TCNNQ exhibits a shift of 0.6 eV to lower energy, whereas the DBP derived single broad peak shifts by 0.7 eV to higher energy. Moreover, the intensity ratio of the two F₆TCNNQ peaks is clearly changed, so that both peaks have roughly the same intensity. At first glance one would assume that these effects are a clear sign of an intermolecular charge transfer from DBP to F₆TCNNQ in the mixed film. However, the observed peak shift of the F₆TCNNQ features is significantly smaller than for (K⁺)(F₆TCNNQ⁻) (green curve), where it was 1.0 eV. Interestingly, annealing the mixed film leads to a further shift to lower energy which is now comparable to the potassium doped F₆TCNNQ film. Annealing also leads to an additional shift of the DBP feature but only a very small one of around 0.1 eV.

Continuing the discussion with the N1s core level spectra, displayed in the middle panel of Fig. 4.12, the situation becomes more clear. The mixed film spectrum is significantly broader than the pristine spectrum and its maximum is slightly shifted, by approx. 0.2 eV, to lower energy. Subsequent annealing leads to the emergence of a new species at about 1.1 eV lower energy at the same position as the anionic spectrum of potassium doped F₆TCNNQ.

The F1s spectra (Fig. 4.12, right panel) do not show changes in the spectral shape but shifts that resemble those of the C1s spectra. The evolution of the core level spectra clearly indicates that a significant charge transfer of ionic character only occurs after annealing of the sample. Although characteristic shifts of the donor and acceptor derived peaks are already observed in the non-annealed film, a second species in the N1s region is not strongly pronounced at that stage. Also the energy shifts are significantly smaller than in the reference system (K⁺)(F₆TCNNQ⁻). The F1s spectrum is an exception here, because the shift after annealing even exceeds the one observed in the (K⁺)(F₆TCNNQ⁻) salt. We therefore suggest that the peak shifts and broadening observed in the non-annealed film mainly reflect changes in the local molecular environment. A broadening of the N1s spectrum of similar magnitude was observed at the F₆TCNNQ/DBP interface, shown in Fig. 4.10, which was discussed in the previous section. The changes in the peak intensity ratio in the C1s spectrum and the small shoulder in the N1s spectrum indicate that a small portion of molecules also undergo a charge transfer reaction, possibly a weak hybridisation of the frontier orbitals takes place. However, annealing leads to an

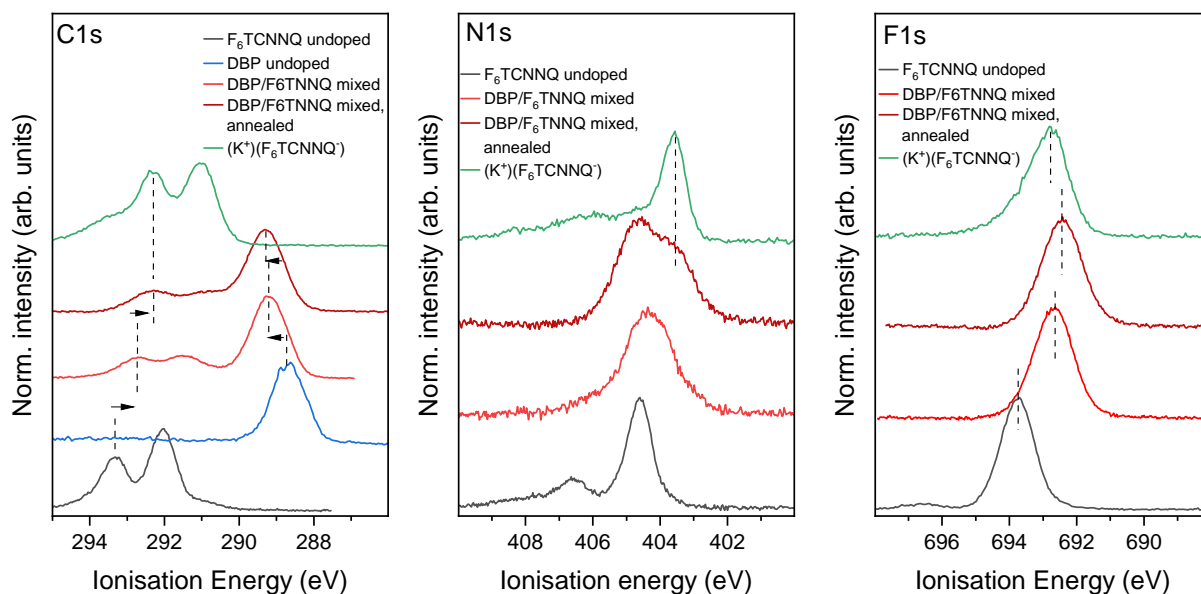


Figure 4.12: C1s (left), N1s (centre) and F1s (right) spectra of pristine a F₆TCNNQ film (black) a pristine dibenzopentacene film (blue) and a co-evaporated mixed film of approx. 1:1 composition before (light red) and after (dark red) annealing at 100 °C for 1 h. Mixing both materials leads to energetic shift, annealing leads to further shifts and emergence of new feature in N1s spectrum. Spectra of (K⁺)(F₆TCNNQ⁻) salt are shown in green as reference.

additional significant change in the spectra. Probably, the donor and acceptor molecules initially arrange in separated clusters where only few acceptor molecules find a donor molecule to undergo charge transfer. Annealing leads to intermixing of those clusters and consequently to a stronger pronunciation of the anionic species in the core level spectra.

We continue the discussion with the UPS measurements of the valence region, displayed in Fig. 4.13. The HOMO of the mixed film before annealing has a spectral onset at about 5.6 eV and is followed by a broad structure with at least three distinguishable peaks that extends approx. from 6.7 eV to 9.0 eV. Compared to pristine DBP, its HOMO is shifted by about 0.5 eV to a higher ionisation energy. The core level spectra suggested that only a small portion of molecules underwent a charge transfer for the non-annealed film. If that is the case, its valence spectrum should be a superposition of mainly the two valence spectra of the pristine materials. Such a spectrum reconstruction is shown in the right panel of Fig. 4.13. It becomes apparent that the valence spectrum can be roughly reproduced by superimposing the pristine spectra but they had to be shifted in energy. The shifts were -0.95 eV for F₆TCNNQ and 0.45 eV for DBP. This finding first seems contradictory because on the one hand, the energetic shifts suggest a charge transfer and on the other, the mixed film spectrum can be reconstructed by only the neutral spectra of the two constituents and no anionic F₆TCNNQ spectrum or (unknown) cationic DBP spectrum was necessary. A reduction of the ionisation energy difference in a blend compared to neat films of two different materials were also observed in other systems [31, 164] and was attributed to a long-range Coulomb interaction, namely the interaction of the molecules quadrupole moments [29]. This leads to two effects: the ionisation energy

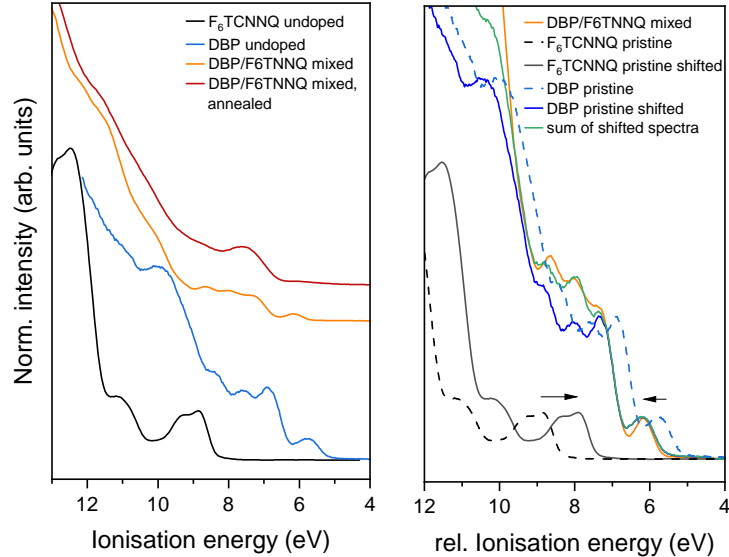


Figure 4.13: Left: UPS spectra of pristine a F_6TCNNQ film (black) a pristine dibenzopentacene film (blue) and a co-evaporated mixed film of approx. 1:1 composition as deposited (orange) and after annealing at $100^\circ C$ for 1 h (red). Right: Reconstruction of non-annealed mixed film spectrum by shifting the two pristine spectra (dashed lines) and superimposing them. The sum (green line) roughly matches with the measured spectrum without taking anionic or cationic spectra into account which signals mainly electrostatic interactions.

difference of the two blend components is reduced by mutual polarisation and the overall ionisation energy of the blend is determined by the mixing ratio [31, 165]. Apparently, we observe a similar effect in the the present F_6TCNNQ/DBP mixed film. Previously studied material combinations mostly included the fluorinated and non-fluorinated version of the same molecule with relatively small energetic offsets of $\leq 1 eV$ between their respective HOMOs. In the present system however, the ionisation potentials are $4.9 eV$ for DBP and $8.4 eV$ for F_6TCNNQ , yielding a difference of $3.5 eV$. Interestingly, instead of an integer charge transfer and ion pair formation, apparently the XPS and UPS spectra can be explained by mainly the just described electrostatic interactions. The determination of the exact correlation between mixing ratio and ionisation energy would require a detailed measurement series and possibly accompanying theoretical calculations which was not in the scope of this work.

After annealing, the valence spectrum changes significantly. The peak at lowest energy is reduced in intensity and a broad feature between 1.6 and $3.2 eV$ appears. The zoomed in region at the Fermi level is displayed in the left panel of Fig. 4.14, referenced to the Fermi level of the substrate. It shows detected occupied states up to the Fermi energy and even slightly above it. Since the onset of the peak does not resemble the shape of a Fermi edge, even when considering instrumental broadening, it is probably not a sign of a metal-like delocalisation of electrons. Instead, this is an indication that the assumption of a common Fermi level or in other words a common work function at every spot on the sample does not hold in this case. The lack of a complete thermodynamic equilibrium at the surface results in small variations of the chemical potential which in turn lead to the emission of electrons with slightly higher kinetic energy which appear in the spectrum at

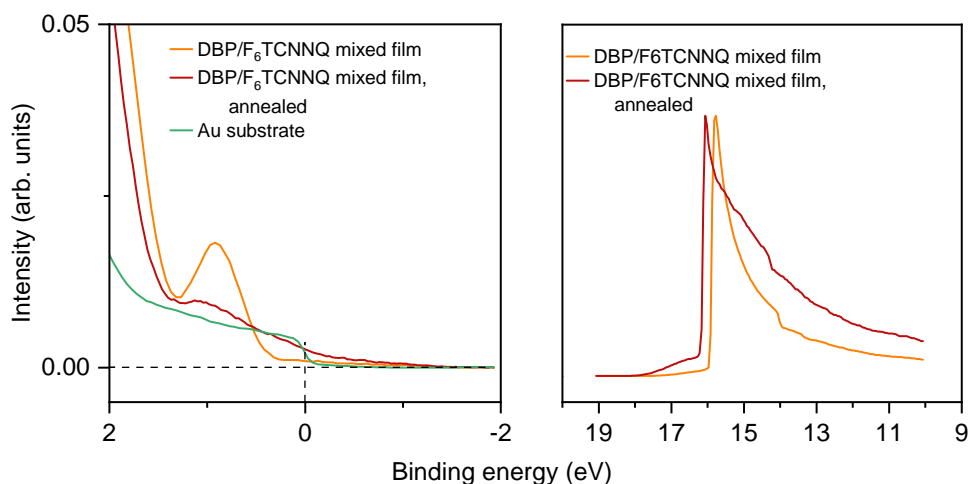


Figure 4.14: Left: UPS spectra of a F₆TCNNQ/DBP 1:1 blended film before (orange) and after annealing (red) on the gold substrate spectrum (green) as reference. Right: High binding energy cutoff of annealed film shows increased intensity at energies higher than the cutoff at about 16.2 eV which suggests a non-equilibrium situation.

negative binding energies. This argumentation is further supported by the high binding energy cutoff (right panel Fig. 4.14), which shows the appearance of a broad low intensity structure in front of the main cutoff for the annealed film. Thus, the seemingly occupied states above the Fermi level are most probably not a property of the charge transfer salt but a consequence of a non-equilibrium situation at the surface. Such a behaviour was also observed by other groups at alkali-metal doped organic semiconductor films [166, 167]. Hence, it cannot be determined with certainty if the whole structure close to the Fermi level is an artefact of a varying chemical potential at the surface or a property of the charge transfer salt. Nevertheless, the broad feature close to the Fermi level shows that the electronic structure of the pristine materials is not reflected in the spectrum any more. This is a further sign of a significant charge transfer reaction which was triggered by a positional rearrangement of the molecules by annealing. Assuming an ionic charge transfer without significant hybridisation, the spectrum should then be a superposition of the anionic F₆TCNNQ spectrum, the cationic DBP spectrum and both neutral spectra since it can be deduced from the areas of the neutral and anionic N1s species that the ratio of anionic to neutral F₆TCNNQ is approx. 1.5:1. Since the cationic spectrum of DBP and the shifts of the other spectra are unknown, a spectrum reconstruction of the annealed film would require too many arbitrary assumptions and is therefore not attempted.

Summarising, we have found that electrostatic interactions determine the electronic properties of a co-evaporated mixed film of F₆TCNNQ and DBP. Annealing leads to large changes in the electronic structure with a charge transfer of ionic character with similar signatures as in the referential charge transfer salt (K⁺)(F₆TCNNQ⁻). The blend stays semiconducting, states at the Fermi level are probably due to variations of the chemical potential at the film surface. The next section will deal with the pairing of F₆TCNNQ with a large metal-acetylide complex which is possibly relevant for single molecule switching applications.

4.2.2 Ruthenium-acetylide complex

In the previous section, the charge transfer characteristics between F₆TCNNQ and two polycyclic hydrocarbons with a similar size were investigated. This section will deal with a significantly larger molecule, an organometallic complex, *trans*-[Ru(dppe)₂(T)₂], which was synthesised by collaboration partners from the Leibniz Institute for Polymer Research in Dresden. The synthesis route together with the spectroscopic results that will be discussed in the following can be found in Ref. [144].

trans-[Ru(dppe)₂(T)₂] is a so called metal-acetylide complex referring to the involved carbon triple bonds. It comprises a Ru atom surrounded by a phosphine ligand in its centre between two acetylenes which are end-capped with thiophene. An illustration of the molecule, gained by X-ray diffraction measurements on a single crystal, done by Olivier Blaque (University of Zurich) is shown in Fig. 4.15. This sort of organometallic

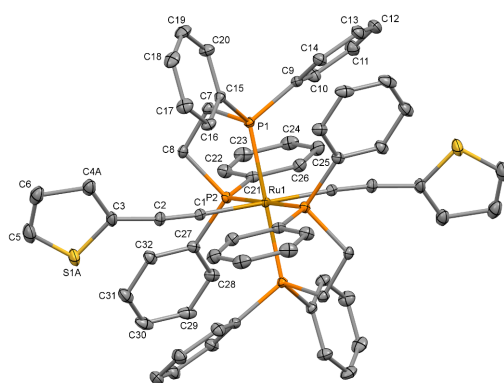


Figure 4.15: Molecular structure of *trans*-[Ru(dppe)₂(T)₂] from single crystal X-ray diffraction, measured by a collaboration partner. Taken from [144].

complexes are building blocks for polymers that are of scientific interest due to their potential application in molecular electronics. For example, in molecular wires that are built up polyiyne units (-≡-), the d_{xz} and d_{yz} orbitals of the transition metal centre can interact with the π -orbitals of the carbon chain [168]. This enables a conductance switching by charge-state alternation of the metal centre [116]. In the following, the electronic properties of *trans*-[Ru(dppe)₂(T)₂] evaporated as thin film will be discussed. Moreover a possible charge transfer reaction at the interface to F₆TCNNQ will be investigated.

Since *trans*-[Ru(dppe)₂(T)₂] was a new molecule which was not investigated spectroscopically before, this section is started by discussing the electronic properties of a pristine film. *trans*-[Ru(dppe)₂(T)₂] will be referred to as Ru complex (RuC) in the following. Fig. 4.16 shows the optical absorption in the UV and visible range, measured by our collaboration partners, of the RuC dissolved in dichloromethane and in solid form as spin-coated film. The spectral onset is at 3.1 eV for the spin-coated film and at 3.2 eV for the solution. The relatively small energetic difference of the excitation indicates a small molecular interaction (polarisation energy, cf. Sec. 2.1) in the film. The optical gap of 3.1 eV represent a lower limit for the transport gap, since optical excitations in organic solids are of excitonic nature (see Sec. 2.1).

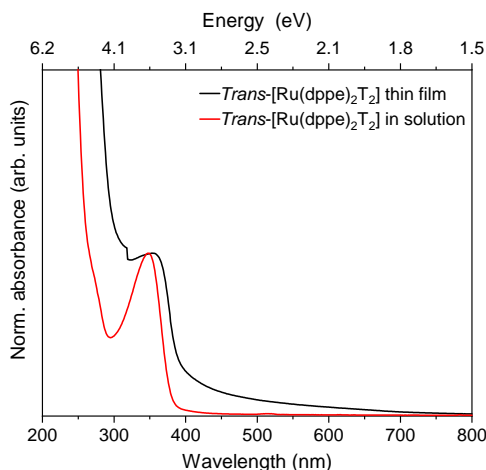


Figure 4.16: Optical absorption spectra of a spin-coated *trans*-[Ru(dppe)₂(T)₂] film on a glass substrate (black) and 0.7 mmol L⁻¹ solved in dichloromethane (DCM) (red). Measurement conducted by collaboration partners. Adapted from [144].

The photoemission spectra of a 7.0 nm thick vacuum-evaporated film are shown in Fig. 4.17 in dependence of the ionisation energy. Starting with the C1s XPS spectrum, shown in Fig. 4.17 (a), it comprises a large peak at an ionisation energy of 288.8 eV and a smaller peak at 287.0 eV. The Ru3d_{5/2} line is found at 284.7 eV, whereas the Ru3d_{3/2} line at 288.9 eV [139] is superimposed by the main C1s feature. In order to further analyse the C1s spectrum the Ru3d peaks were subtracted (intensity and position of Ru3d_{3/2} in relation to Ru3d_{5/2} line is determined by quantum mechanics [139], cf. Table 3.2). Fig. 4.17 (b) shows the C1s spectrum after subtraction of the Ru3d features. In the molecular structure of the RuC, carbon is present in 3 different configurations. 56 of the 64 carbon atoms are sp²-hybridised (double bonds) and 4 each are sp- (triple bonds) and sp³-hybridised (single bonds). The feature with the lowest ionisation energy at 187 eV is assigned to the sp-hybridised carbon with the assumption that the two electron forming π -bonds provide additional screening to the photohole which results in a lower ionisation energy. Accordingly, the strongest peak at 288.8 eV should stem from the sp² hybridised carbon atoms while the sp³ hybridised carbons are assigned to the peak at the highest ionisation energy. The area ratio of the three different C1s peaks should reflect the quantitative ratio of the three carbon configurations in the molecule (14:1:1) This ratio could be reproduced by the fits shown in Fig. 4.17 (b).

The S2p and P2s core level spectra (Fig. 4.17 c, d) comprise one single spin-orbit split component each, which is expected since both atoms are only present in a single configuration. The area ratios of the core levels weighted with the respective ionisation cross sections reflected the same elemental composition of the film as expected for the molecule which indicates that the molecules stayed intact during the evaporation.

The UPS spectrum in Fig. 4.17 (e) gives an ionisation potential, derived from the onset of the HOMO derived feature, of 5.0 eV. The work function of the film was calculated from the high binding energy cutoff position as 3.5 eV. Together with the optical gap determined from the optical absorption measurements, it can be concluded that the RuC is a wide-gap semiconductor with the Fermi energy positioned in the middle of the gap. An energy level diagram is shown in Fig. 4.18.

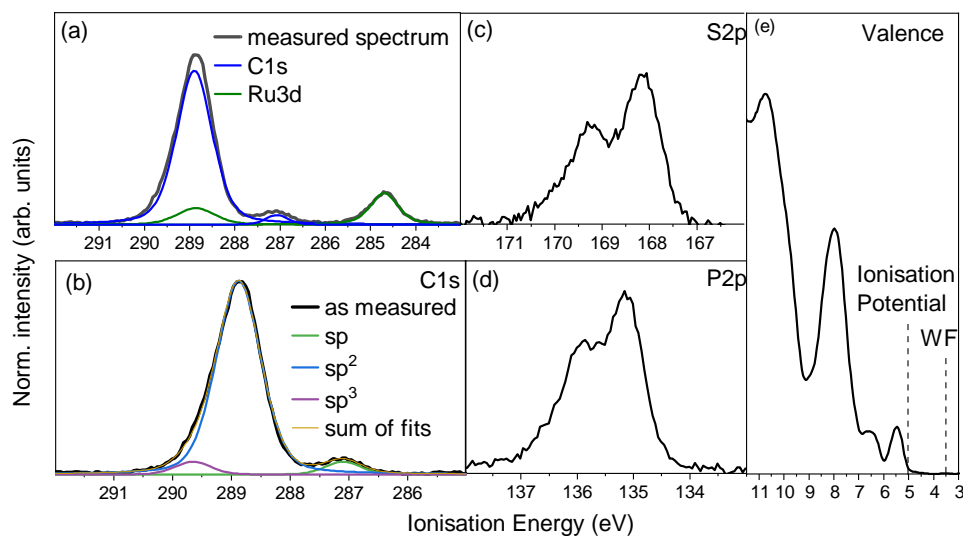


Figure 4.17: Photoemission spectra of a 7.0 nm thick film of *trans*-[Ru(dppe)₂(T)₂]. (a) C1s (blue) and Ru3d (green), (b) only C1s spectrum after subtraction of Ru3d doublet, (c) S2p, (d) P2p and (e) UPS valence spectrum.

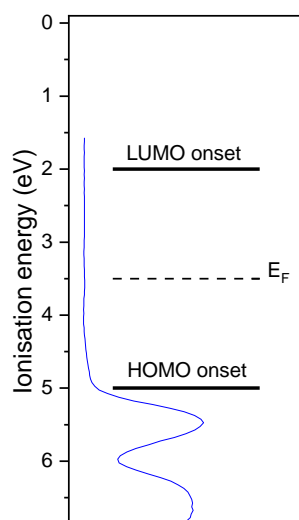


Figure 4.18: Energy level diagram of *trans*-[Ru(dppe)₂(T)₂] based on UPS and UV-VIS absorption measurements. UPS spectrum is shown in blue.

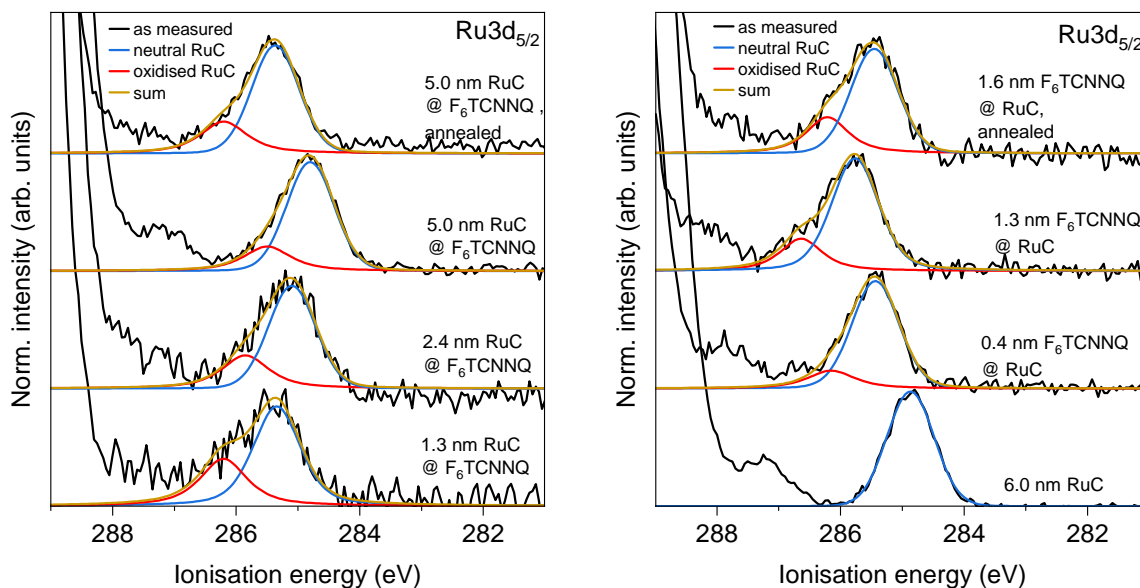


Figure 4.19: XPS spectra of Ru3d_{5/2} level of *trans*-[Ru(dppe)₂(T)₂] deposited stepwise on F₆TCNNQ (left) and the opposite sequence (right). The Fit obtained from the neutral spectrum is (bottom right) is shown in blue. All other spectra can be reproduced by a superposition of the neutral spectrum and a second contribution (red) which is assigned to oxidised *trans*-[Ru(dppe)₂(T)₂] at the interface.

After having established the electronic properties of the new Ru-acetylide complex, a possible charge transfer reaction to F₆TCNNQ is measured by forming an interface with the known procedure, described in Sec. 3.4. The following photoemission spectra are arranged side by side with the RuC@F₆TCNNQ sequence on the left and F₆TCNNQ@RuC on the right.

The discussion is started with the Ru3d_{5/2} level shown in Fig. 4.19. The bottom right spectrum shows the pristine RuC film with a single feature which was fitted by a Voigt profile with predominantly Gaussian contribution (blue). Analogous to the F₆TCNNQ/PCHC system discussed in Sec. 4.2.1, the deposition of F₆TCNNQ leads to a shift to higher ionisation energies indicating a charge redistribution at the interface. The opposite shift is observed for the reverse deposition sequence. Moreover changes in the spectral shape are observed. With increasing F₆TCNNQ overlayer thickness, a shoulder at 0.85 eV higher ionisation energy appears and increases in relative intensity. The same feature is present for the reverse sequence, this time decreasing in intensity with increasing RuC thickness. This behaviour is in accordance with the assumption of a charge transfer at the interface withdrawing electron density from the Ru atom which leads to a diminished screening of the photohole and therefore a higher ionisation energy. Since only RuC molecules at the interface get oxidised, the cationic feature decreases with increasing RuC thickness. For the reverse sequence, RuC signal is first dominated by unreacted lower lying molecules whereas for increasing F₆TCNNQ coverage, the share of molecules close to the interface to the overall signal increases. The topmost spectra were taken after annealing the same heterojunctions at 100 °C for 1 h. Interestingly, the share of the charged feature increases again, indicating a temperature induced inter-diffusion of both molecules despite the large size of the RuC.

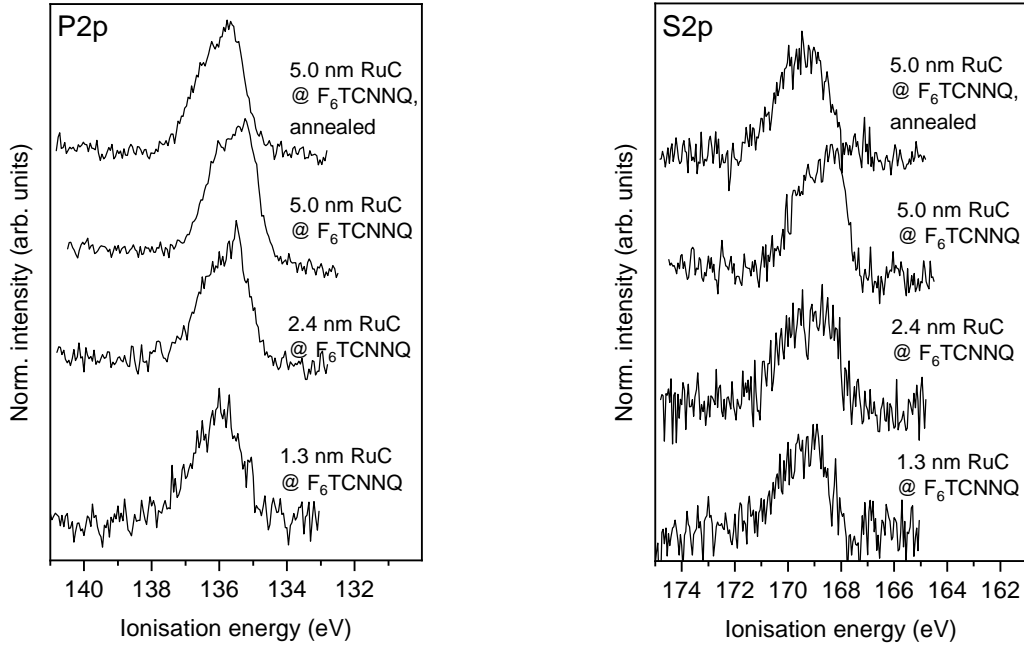


Figure 4.20: P2p (left) and S2p (right) spectra of *trans*-[Ru(dppe)₂(T)₂] deposited step-wise on F₆TCNNQ.

The P2p and S2p core level spectra of the RuC@F₆TCNNQ sequence are shown in Fig. 4.20. Compared to the pristine film in Fig. 4.17, both S2p and P2p spectra show less structure. This indicates a more disordered growth of the RuC in this sample. Although the relatively low signal-to-noise ratio makes it difficult to analyse the peak shape in detail, no significant difference between the 5.0 nm film and the annealed film can be observed. This indicates that the additional charge is located mainly at the Ru centre. Changes in the C1s spectra at the interface could not be determined due to the different C1s species and the overlap of the Ru3d_{5/2} line. Having identified a oxidised RuC species at the interface, we proceed with the N1s spectrum of F₆TCNNQ, shown in Fig. 4.21, which proved very sensitive for charge transfer in the previously discussed systems. Surprisingly, in contrast to the three systems analysed so far, the N1s line of F₆TCNNQ at the interface (bottom right spectrum) comprises two peaks at 402.7 eV and 404.9 eV. The neutral N1s line (bottom spectrum, right panel) lies at 404.6 eV, which is consistent with the previously measured films. The position of the lower energy peak would be consistent with the N1s spectrum of reduced F₆TCNNQ that was measured for the other F₆TCNNQ based interfaces with an energetic difference to the neutral N1s peak of about 1.1 eV. The presence of a second peak at higher ionisation energy however, indicates reduced charge density around the at least some nitrogen atoms. In a study of the similar acceptor F₄TCNQ, a peak in the same energy region was previously assigned to a charge transfer complex state of F₄TCNQ [169]. Both peaks could be fitted with a Voigt profiles that have an area ratio of 3:1 (red dotted lines in bottom right spectrum). This could suggest that a complex is formed where charge is transferred to one of the four cyano groups of F₆TCNNQ which leads to a similar spectral signature as for the other systems discussed previously, while the three other cyano groups form a bond of covalent character with parts of the ligand of the RuC which leads to reduced charge density and hence to a peak

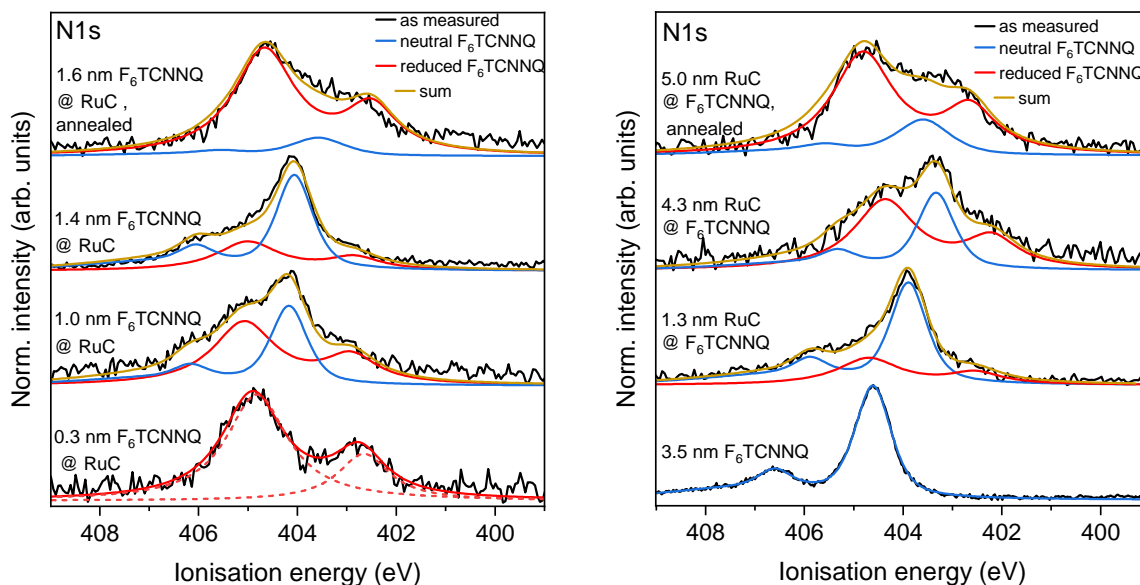


Figure 4.21: XPS spectra of N1s level of F₆TCNNQ as bottom layer and stepwise deposition of *trans*-[Ru(dppe)₂(T)₂] (left) and the opposite sequence (right). The neutral spectrum (bottom left) and the reduced spectrum (bottom right) were fitted by Pseudo-Voigt profiles. All other spectra comprise these two components.

at higher ionisation energy. Another possible scenario is that only 1/4 of all F₆TCNNQ molecules at the interface undergo integer charge transfer, while 3/4 form a charge transfer complex. This is however unlikely because annealing of the heterojunctions yields the same spectrum for both deposition sequences. If at the interface 1/4 of the F₆TCNNQ molecules underwent ionic charge transfer, then an intermixing of both molecules should change this ratio.

To gain further hints about the charge transfer reaction, F₆TCNNQ and the RuC were solved in DCM in a 1:1 ratio for a UV-VIS absorption measurement by our collaboration partners. The spectra of both pristine molecules and the mixture are shown in Fig. 4.22. The excitation onset of pure F₆TCNNQ is around 500 nm which corresponds to an optical gap of 2.4 eV which in accordance to published values [99]. The RuC spectrum shows a strong peak with a spectral onset of 400 nm or 3.1 eV. In the mixture of both materials a new broad feature with an onset at around 950 nm or 1.3 eV appears which extends to 1400 nm or 0.9 eV. This peak shows that intermolecular charge transfer also takes place in solution. The spectrum of anionic F₆TCNNQ reported in literature comprises a major peak centred at around 1150 eV followed by vibronic satellites at smaller wavelengths [170]. In the present spectrum, these features are not clearly resolved. It is possible that they are overlapped by the (unknown) cationic RuC spectrum, but nevertheless, the measurement suggests a complex formation rather than an ionic charge transfer.

Finally, the valence spectra are shown in Fig. 4.23 with the work function, determined by the secondary electron cutoff, indicated by vertical lines. The spectrum of the pure F₆TCNNQ film (bottom left) shows occupied states up to the Fermi level. This attributed to the gold substrate and the charge transfer from gold to F₆TCNNQ which was discussed in Sec. 4.1.2. Apparently, the film exhibits island-like growth resulting in thin areas where photoelectrons of the F₆TCNNQ/Au interface are still detected. With increasing

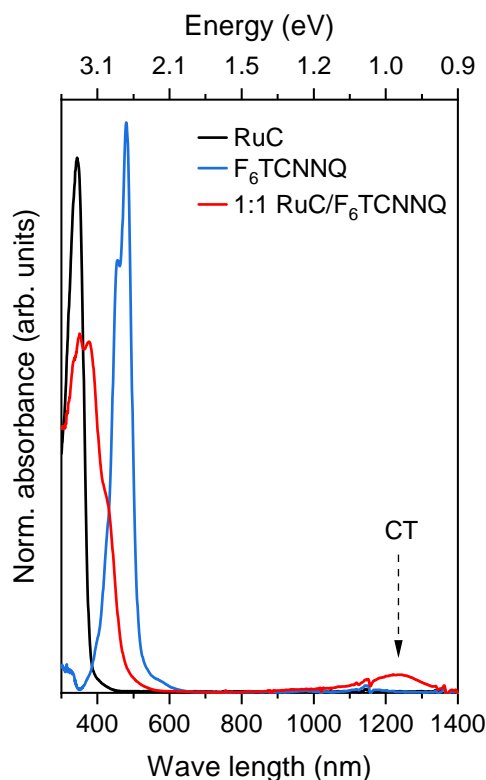


Figure 4.22: Optical absorption spectra of pristine materials *trans*-[Ru(dppe)₂(T)₂] (black) and F₆TCNNQ (blue) and a 1:1 mixture in DCM solution (red). Measurement conducted by collaboration partners. Adapted from [144].

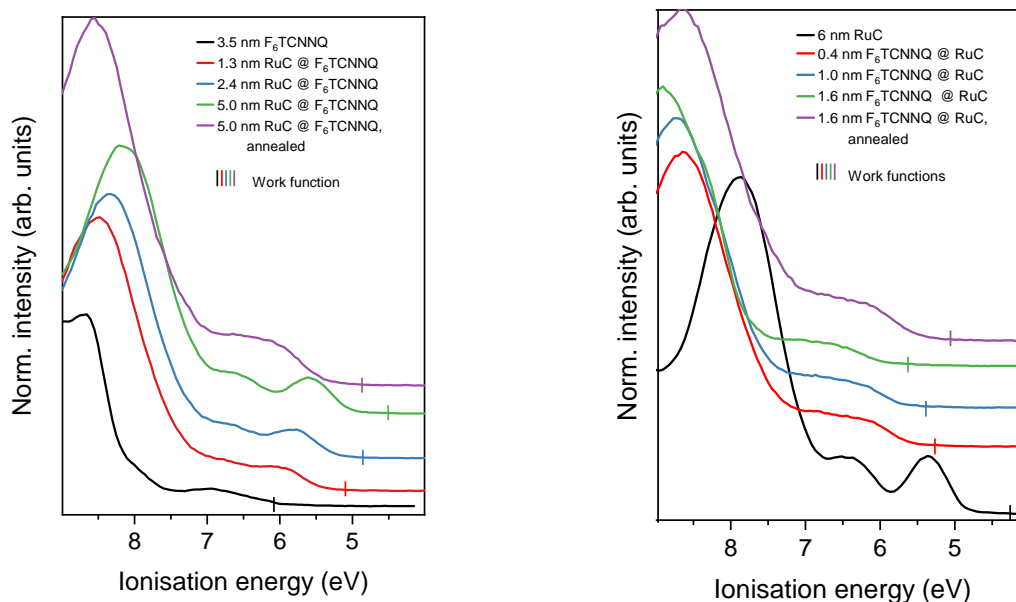


Figure 4.23: UPS spectra of a F₆TCNNQ film and stepwise deposition of *trans*-[Ru(dppe)₂(T)₂] (left) and opposite deposition sequence (right). The work function of each deposition step, determined by the secondary electron cutoff, is denoted by a vertical line.

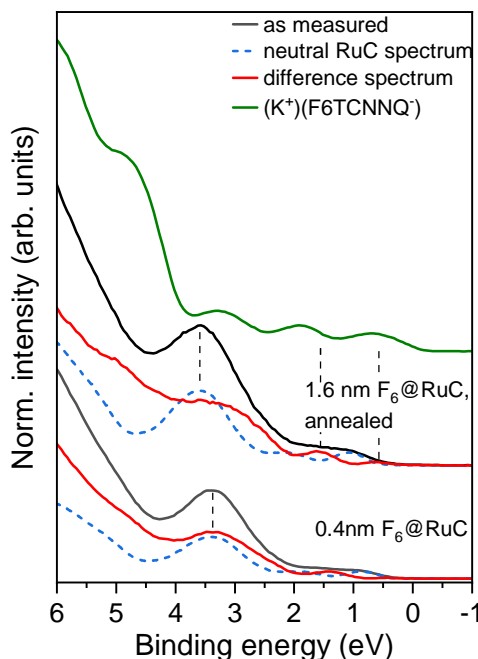


Figure 4.24: UPS spectra of a *trans*-[Ru(dppe)₂(T)₂] film with a 0.4 nm thick F₆TCNNQ overlayer and an annealed interface. Subtraction of pristine *trans*-[Ru(dppe)₂(T)₂] spectrum (blue) yields difference spectrum (red). Spectrum of (K⁺)(F₆TCNNQ⁻) is shown for comparison (green) which differs from red spectra, suggesting that F₆TCNNQ is not present in purely anionic form but rather as part of a charge transfer complex with *trans*-[Ru(dppe)₂(T)₂].

coverage of the RuC, the previously discussed valence structure of the RuC appears until the spectrum resembles that of pure RuC. The spectral evolution is analogous for the reverse deposition sequence, so that the for intermediate film thicknesses (red curve on left and blue curve on the right) both spectra look alike. After annealing, the spectra resemble those for intermediate thicknesses with a broad feature that extends from 5.5 eV to the onset of the RuC's HOMO at around 7.0 eV. This feature cannot be reproduced by simply superimposing the spectra of both pristine materials. Fig. 4.24 shows the valence spectra of 0.4 nm F₆TCNNQ/RuC and the annealed film of the same sequence. It becomes apparent that after subtracting the pristine RuC spectrum, the resulting difference spectra show two peaks centred at around 0.6 and 1.6 eV that cannot stem from pristine F₆TCNNQ and must therefore be attributed to the charge transfer complex. Apart from a small shift to higher binding energy, the spectrum of the annealed film is equal to the one at of the interface which is in accordance to the XPS spectra and signals that the charge transfer reaction is equal. For comparison, also the spectrum of (K⁺)(F₆TCNNQ⁻) which was shifted so that the features closest to the Fermi energy are aligned is shown in Fig. 4.24. It becomes apparent that the energetic distance of the first two features of (K⁺)(F₆TCNNQ⁻) and the F₆TCNNQ/RuC difference spectra are different, which is further indication that F₆TCNNQ is not present in purely anionic form but as a charge transfer complex with the RuC.

Summarising, a charge transfer reaction between F₆TCNNQ and *trans*-[Ru(dppe)₂(T)₂] was detected spectroscopically. The N1s and UPS spectra indicate charge transfer complex

formation rather than ionic charge transfer because the spectra differ from those of the referential system $(K^+)(F_6TCNNQ^-)$. Annealing lead to an intermixing of both molecules which lead to the same charge transfer reaction as at the interface.

4.2.3 F₆TCNNQ/ET and F₂TCNQ/ET interfaces: a comparison

This section will deal with the organosulfur molecule BEDT-TTF also referred to as ET. It gained a lot of scientific interest as a cation for superconducting charge transfer salts [171]. In those materials, it is arranged with various counter-ions in a separate stack crystal structure. The binary crystal of ET and the acceptor F₂TCNQ is reported to show Mott insulating behaviour [83, 98]. Moreover, the interface between single crystals of ET and F₂TCNQ is claimed to show band-like transport properties [19]. Thus, the purpose of the experiment presented in the following was on the one hand to investigate the material combination ET and F₂TCNQ as an interface and on the other hand to compare these findings with the interface to the larger and stronger acceptor F₆TCNNQ. The presented results were published in Ref. [172].

The C1s spectra of the two interfaces are not discussed since they show a strong overlap between the ET and F₆TCNNQ (F₂TCNQ) derived spectra which makes a detailed analysis almost impossible. The F1s spectra follow the progression of the work function and do not show obvious changes in the peak shape, which was also observed for the previously discussed systems and was explained by the small contribution of the fluorine electrons to the LUMO of the acceptors. Thus, we start the discussion with the N1s core level spectra, shown in Fig. 4.25, with the F₆TCNNQ/ET sequence on the left and the F₂TCNQ/ET sequence on the right. The topmost spectra represent the unreacted

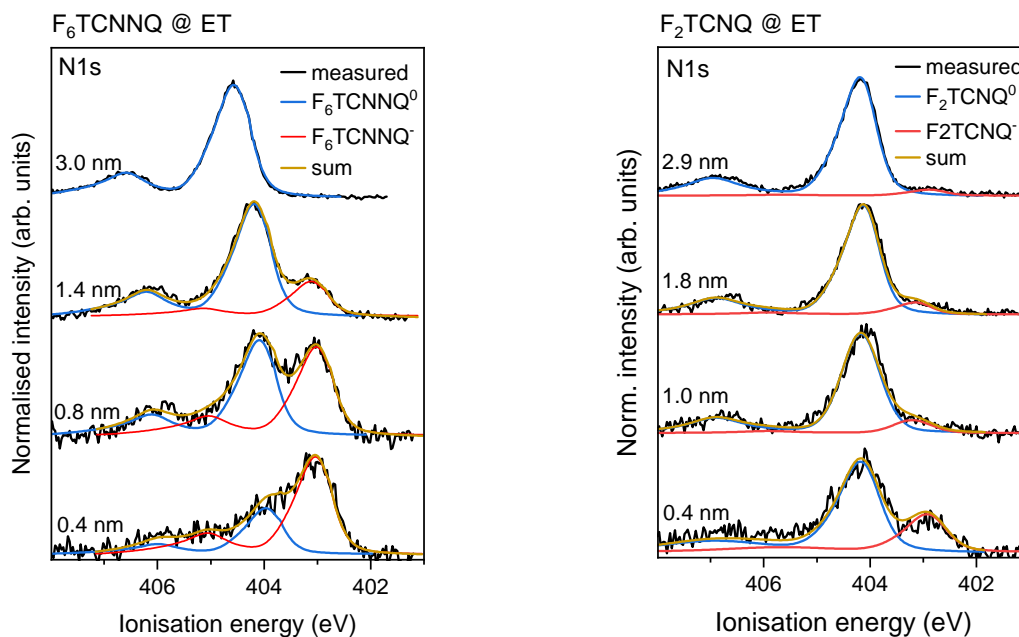


Figure 4.25: N1s core level spectra of F₆TCNNQ (left) and F₂TCNQ (right) deposited stepwise on ET films of 5.0 and 4.7 nm thickness. All spectra can be fitted by the superposition of neutral (blue) and reduced (red) contribution. Reduced spectrum is identical to neutral spectrum but shifted to lower binding energies.

molecules due to the relatively large film thickness with the main line of F₆TCNNQ centred at 404.6 eV and that of F₂TCNQ at 404.2 eV. This difference in ionisation energy is due to a chemical shift stemming from the electronegativity of fluorine that diminishes the electron density around the nitrogen atoms, which leads to a higher ionisation energy

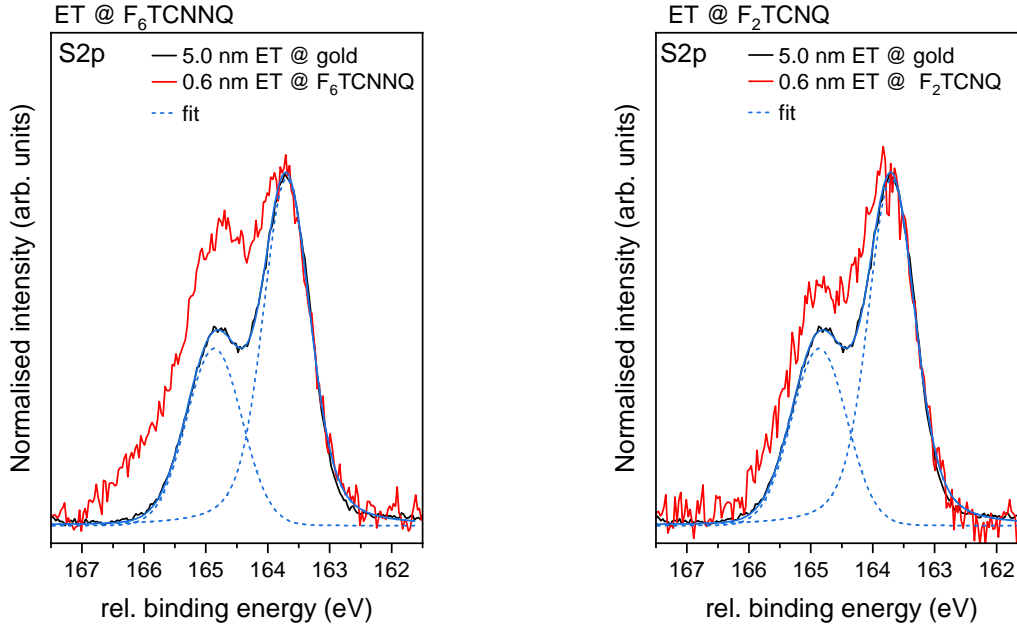


Figure 4.26: S2p core level spectra of a thick ET film on a polycrystalline gold substrate (black) and thin ET films on F₆TCNNQ and F₂TCNQ (red). The red spectra were shifted relative to the black spectra so that the larger peak is aligned in order to visualize the broadening and difference in intensity ratio. The spectra of the thick films can be fitted with two Voigt profiles with $\Delta E = 1.16$ eV and an area ratio of 2:1 (blue).

for F₆TCNNQ since it comprises more fluorine than F₂TCNQ. The energy difference to the π - π^* shake-up satellite is 1.9 eV for F₆TCNNQ and 2.7 eV for F₂TCNQ indicating a larger HOMO-LUMO gap for F₂TCNQ. At small film thicknesses, a second peak at 1.1 eV lower ionisation energy for F₆TCNNQ and 1.2 eV lower energy for F₂TCNQ is present. All spectra can be fitted by superpositions of these two contribution. This is in line with the spectra of at the interfaces of F₆TCNNQ with the polycyclic hydrocarbons (Sec. 4.2.1) and gold (Sec. 4.1.2). Therefore it indicates an ionic charge transfer for both, the F₆TCNNQ and F₂TCNQ interface. The area ratio of the anionic species to the neutral one at a small film thickness of 0.4 nm is 2:1 for F₆TCNNQ/ET and 1:2 for F₂TCNQ/ET which suggests a different degree of charge transfer or number of reduced molecules at the interface. This will be discussed later in this section.

The discussion is continued with the core level spectra of sulphur which is only present in ET. Fig. 4.26 shows the S2p spectra of thick unreacted ET films on a gold substrate (black) and thin ET films on both acceptors (red) that were aligned in binding energy for comparison. The pristine ET spectrum consists of one spin-orbit split species, which is expected since the electronic surrounding of the 8 sulphur atoms in ET that are each bound to two carbon atoms by single bonds should not differ strongly. By contrast, the red spectra show a clear difference in intensity ratio of the two components and a broadening. For the ET/F₆TCNNQ these differences are more strongly pronounced and a shoulder at a relative binding energy of 166.5 eV is present. The obvious approach would be to fit the spectra with a second species which is shifted to higher binding energies due to the reduced electron density around the S atoms due to an electron transfer to the respective acceptors. This is however not possible. A third species is necessary to reproduce

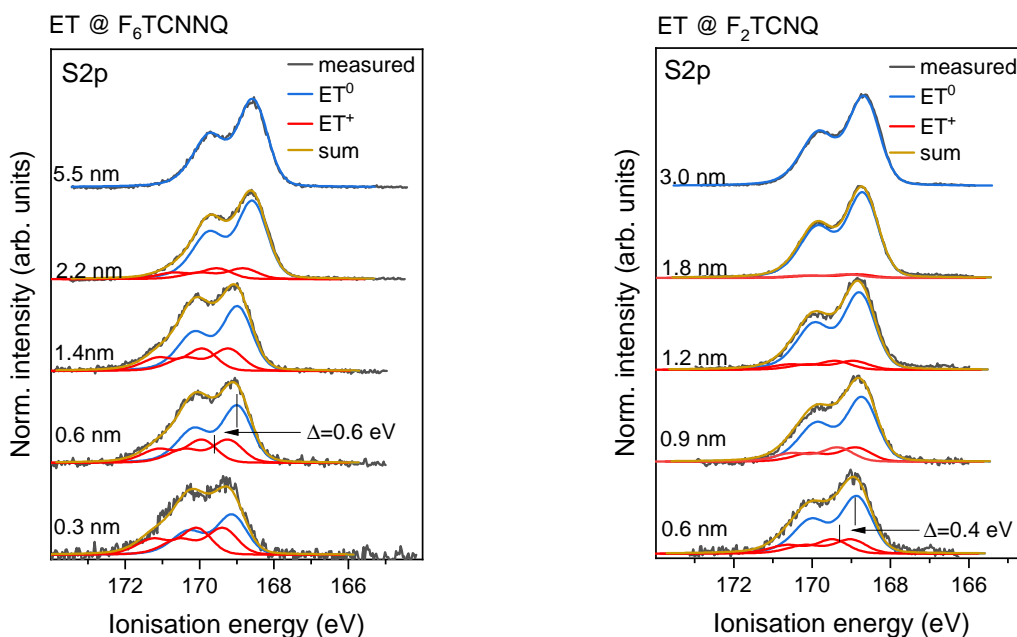


Figure 4.27: S2p core level spectra of ET/F₆TCNNQ (left) and ET/F₂TCNQ interface (right). With increasing film thickness, the cation contribution (red) stemming from the interface to the overall spectrum decreases while the share of the neutral spectrum (blue) increases. Anion spectrum consists of 2 components due to unequal contributions of the sulphur atoms to the HOMO of ET.

the interface spectra. This approach is motivated by the reported HOMO distribution on the ET molecule which was determined by quantum chemical calculations (MNDO method) by other groups [173, 174]. It is stated in these publications that the inner 4 sulphur atoms contribute to the HOMO in a significantly larger extent than the outer 4 sulphur atoms. The removal of charge from this molecular orbital would therefore induce a stronger chemical shift in the inner rings' sulphur atoms than on the outer. Accordingly, the ET S2p spectrum at the interface should comprise three species: unreacted ET, the inner 4 and the outer 4 S atoms of oxidised ET. In the neutral state, the chemical environment of the S atoms is apparently more similar, so that the neutral spectrum can be fitted with one species.

The full evolution of the spectra across the interfaces is shown in Fig. 4.27. The spectra can be fitted well with 3 contributions, the neutral spectrum in blue and the two cation spectra, with equal areas, corresponding to the equal number of inner and outer sulphur atoms, in red. As expected, the share of the two oxidised species to the overall spectrum decreases for increasing coverage. Considering the nominal coverage of 0.6 nm ET on the respective acceptors, the energy difference between the neutral and the cation species is 0.6 eV for the ET/F₆TCNNQ and 0.4 eV for the ET/F₂TCNQ interface (cf. Fig. 4.27). Here, the centre between the two cationic S2p contribution was used as reference point. The area ratios oxidised : neutral are 1.3:1 for the ET/F₆TCNNQ and 0.5:1 for ET/F₂TCNQ interface. These values can only be taken as rough estimations because of the significant uncertainties of the film thickness determination and the fitting procedure. The area ratios and energy differences of the N1s and S2p core level spectra are summarised in table 4.1. For the ET/F₂TCNQ combination we observe area ratios

Table 4.1: Comparison of the energy differences (ΔE) and area (A) ratios between neutral ($N1s^0$, $S2p^0$) and charged ($N1s^-$, $S2p^+$) core level spectra for the two interfaces F_6TCNNQ/ET and F_2TCNNQ/ET .

	$\Delta E N1s^{0/-}$	$\frac{A(N1s^-)}{A(N1s^0)}$	$\Delta E S2p^{0/+}$	$\frac{A(S2p^+)}{A(S2p^0)}$
F6/ET	1.1 eV	2:1	0.6 eV	1.3:1
F2/ET	1.2 eV	0.5:1	0.4 eV	0.5:1

reacted/unreacted of 0.5:1 for both N1s and S2p spectra, whereas these ratios are 2:1 and 1.3:1 for ET/ F_6TCNNQ . Since the N1s and S2p spectra were recorded for opposite deposition sequences, differences in the film morphology and the uncertainty in the film thickness determination are an explanation for the different ratios for the ET/ F_6TCNNQ combination. The clear tendency however is that for the ET/ F_2TCNNQ combination the share of the reacted contributions to the interface spectra are significantly smaller than for ET/ F_6TCNNQ combination. Moreover, the energetic shift of the S2p anion species is 50 % larger for the F_6TCNNQ combination.

The area ratios can be rationalised in two different ways: If we consider a complete ionic charge transfer, the area ratios reflect the quantitative ratio of ionised to non-ionised molecules. If F_2TCNNQ grows in a more island like manner or is on average oriented differently to ET than F_6TCNNQ , this could lead to a lower fraction of reduced F_2TCNNQ molecules. The other interpretation is that the peak area ratios correspond to the degree of charge transfer. For a partial charge transfer, the molecules' state is a superposition of the charged and uncharged state. The photoemission process probes one of both states with a probability that reflects the degree of charge transfer, which then again corresponds to the area ratios of the two core level species. The same argumentation was used in a photoemission study of the organic metal TTF-TCQ [84]. To elucidate which interpretation seems more plausible, we direct our attention back on the energy differences between neutral and reacted species listed in table 4.1. The shift of the S2p cation spectrum for the ET/ F_6TCNNQ interface is approximately 50 % larger. This is an indication for a higher degree of charge transfer. A higher charge transfer leads to a weaker screening of the photohole during the photoemission process and therefore to a stronger increase of the ionisation energy (cf. Sec. 3.2.3). Additionally, the deformation of the molecule (polaron, cf. Sec. 2.2) depends on the degree of charge transfer which also leads to different core level energy shifts for both systems.

While different molecular orientations could indeed play a role, the strong discrepancies in the area ratios and the energy shifts in the ET core levels leads us to the conclusion that a stronger degree of charge transfer for the ET/ F_6TCNNQ combination is the more probable scenario. This also reflects the larger electron affinity of F_6TCNNQ . Previous studies of ET/ F_2TCNNQ mixed single crystals reported a complete ionic charge transfer [83]. This is however not in contradiction to our findings, since the degree of charge transfer can differ significantly in low ordered thin films compared to single crystals.

The analysis is proceeded of the UPS spectra, first with the deposition sequence with ET as bottom layer, shown in Fig. 4.28. All UPS spectra are normalised to the highest intensity and shown in dependence of the binding energy. The insets show the zoomed in low binding energy region. The pure ET spectra, shown in black, have a spectral onset

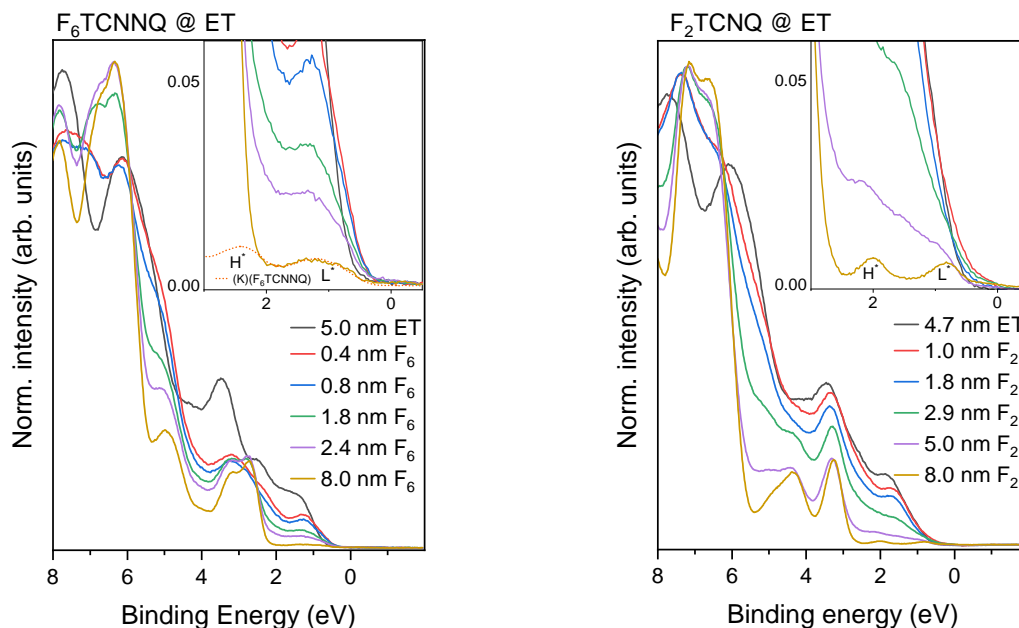


Figure 4.28: UPS valence region spectra of F₆TCNNQ/ET (left) and F₂TCNQ/ET interface (right). The inset shows the same spectra zoomed to the low binding energy region. The ET films evaporated first on polycrystalline gold foils, followed by a stepwise deposition of the acceptors F₆TCNNQ and F₂TCNQ, respectively. H* and L* denote the HOMO and now partially occupied LUMO of charged F₆TCNNQ and F₂TCNQ.

of the HOMO feature of around 0.7 eV. With the work function, shown in Fig. 4.30, the ionisation potential is determined to be 5.0 eV. The second feature, centred at 2.4 eV is more pronounced for the film shown in the left panel. This is probably due to a difference in the films molecular order, which however did not change the ionisation potential. With growing overlayer thickness the ET derived features loose intensity and get superimposed by the acceptor spectra. For high film thicknesses (yellow spectra) it can be assumed that the spectra comprise mostly the neutral acceptor spectra with a small share of the interface spectra. For the reverse deposition sequence (Fig. 4.29), the same spectral composition should be present for small ET overlayer thicknesses (red spectra). Starting with the F₆TCNNQ/ET combination, the spectra of both deposition sequences show a broad feature with a spectral onset of approximately 0.4 eV. Shape and energetic position of this feature would be in accordance with the F₆TCNNQ anion spectrum (shown as red dashed line), determined in Sec. 4.1.1. However it is well possible that also cationic ET has occupied states in this binding energy region, so the spectra might be a superposition of both contributions.

The interfaces between ET and F₂TCNQ are shown in the right panels of Fig. 4.28 and Fig. 4.29. The HOMO derived peak of pristine F₂TCNQ (Fig. 4.29, black curve) has as spectral onset of 2.7 eV. Again, we turn our attention to the spectrum of ET with a high coverage of F₂TCNQ (Fig. 4.28, yellow curve). Two distinct features, centred at 0.8 and 2.0 eV, appear that do not stem from neutral ET. For the opposite deposition sequence, we observe a broad feature that extends from 0.5 eV until the onset of the original HOMO of F₂TCNQ. The different spectra for the two deposition sequences might be due to structural differences. Since there is no published UPS data of F₂TCNQ, the spectra

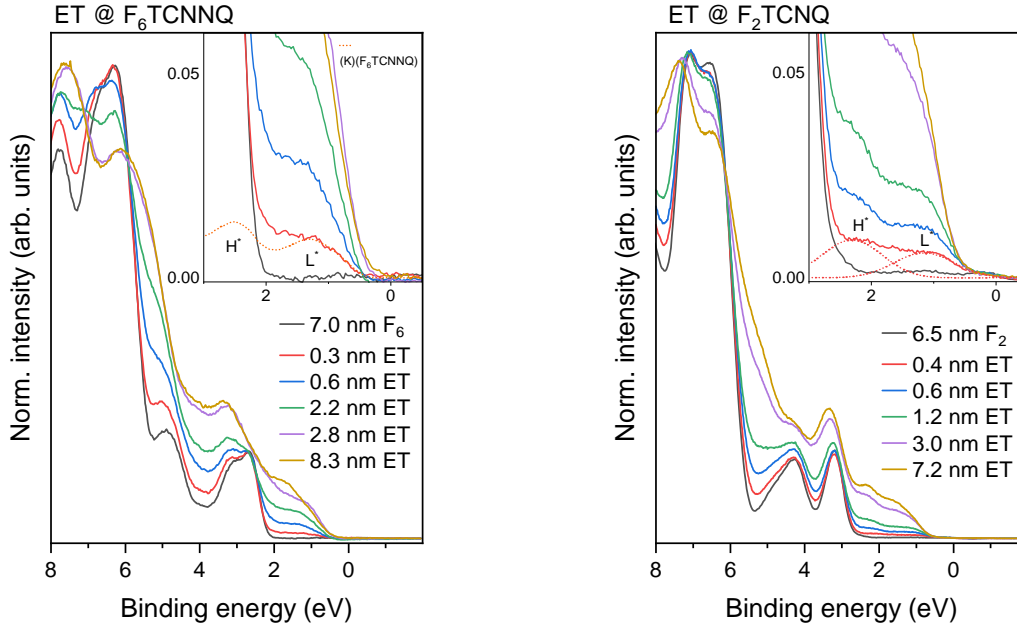


Figure 4.29: UPS valence region spectra of ET/ F_6 TCNNQ (left) and ET/ F_2 TCNQ interface (right). The inset shows the same spectra zoomed to the low binding energy region. The acceptor films of F_6 TCNNQ and F_2 TCNQ were evaporated first on polycrystalline gold foils, followed by a stepwise deposition of ET. H^* and L^* denote the HOMO and now partially occupied LUMO of charged F_6 TCNNQ and F_2 TCNQ.

are compared with studies of other groups on the similar acceptor F_4 TCNQ. An overview of the binding energy positions of the relaxed HOMO and occupied LUMO of anionic F_4 TCNQ is given in Ref. [175]. The energy separation ranges from 0.9 to 1.4 eV, in our case it is 1.2 eV. This would suggest that the two features can be assigned to anionic F_2 TCNQ. However, since the XPS spectra suggest only partial charge transfer from ET to F_2 TCNQ, these two states could also stem from a charge transfer complex formed of both molecules. To shed more light on this question, a detailed analysis of the molecular orientation supported by calculations could be promising but were beyond the scope of this work.

The nominal thickness of 8.0 nm exceeds the escape depth of photoelectrons emitted by UV radiation. The fact that we observe interface related spectra at this film thickness indicates either island growth or the absence of a sharp interface due to interdiffusion. The latter was previously reported for F_6 TCNNQ on perovskite and graphene [103, 104] and for F_4 TCNQ on various substrates [176]. Also diffusion of F_4 TCNQ into various organic films was observed before [177–179]. The progression of the work function in dependence of the top layer thickness, shown in Fig. 4.30, might give further indications. The F_6 TCNNQ/ET interface shows a step initial increase that saturates at a nominal film thickness of 2.0 nm and stays virtually constant at 5.8 eV, a behaviour which was also observed for the interfaces to polycyclic hydrocarbons (Sec. 4.2.1) and *trans*-[Ru(dppe)₂(T)₂] (Sec. 4.2.2). For the reverse sequence, the work function progresses in a similar way with a step decrease followed by a saturation at a thickness of 3 nm. By contrast, for the interfaces comprising F_2 TCNQ, no saturation takes place, instead, the work function continues to increase (decrease) until the nominal thickness of 8 nm. This

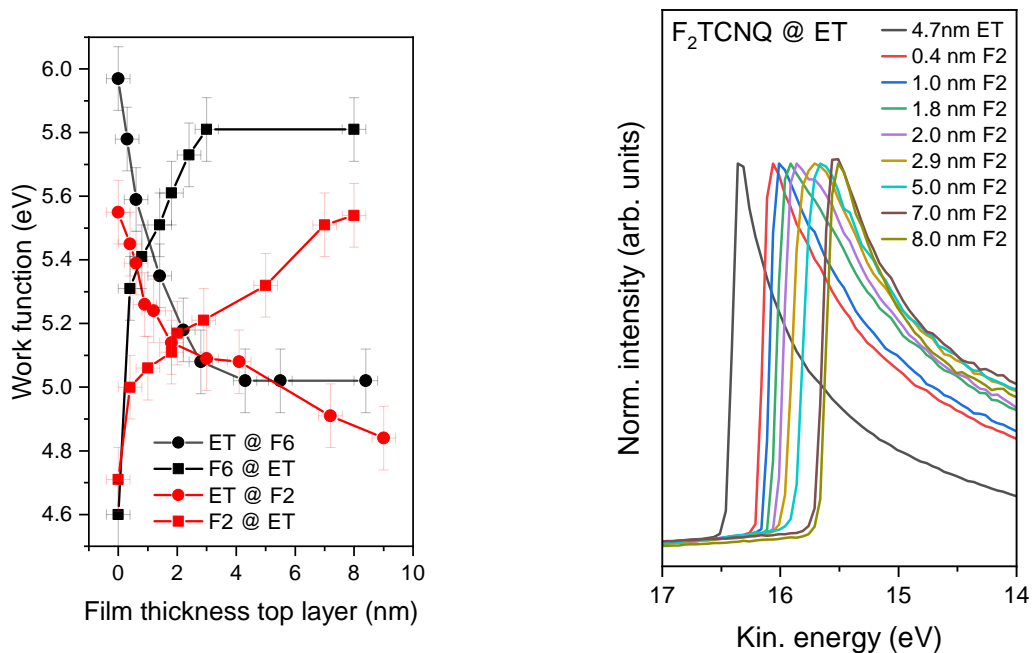


Figure 4.30: Left: Work function progression in dependence of overlayer film thickness for F₆TCNNQ/ET, F₂TCNNQ/ET and the opposite deposition sequences. The data point at 0 nm represents the work function of the bottom layer. Right: exemplary high binding energy cutoffs for one of the interfaces.

is an indication of a more significant interdiffusion of F₂TCNNQ and ET. The high binding energy cutoffs, exemplary shown for F₂TCNNQ@ET in the right panel of Fig. 4.30, do not show any kinks or steps which would indicate regions with significantly different surface compositions with different work functions. This suggests that first a mixed layer of ET/F₂TCNNQ is formed which is followed by island growth. This growth behaviour is referred to as Stranski-Krastanov growth [180]. From this, it can be concluded that F₆TCNNQ forms a relatively sharp interface with ET while interdiffusion is present at the interfaces involving F₂TCNNQ.

For both interfaces, no occupied states at the Fermi level were detected. This is not necessarily in contradiction to studies that reported "metallic" conduction at the interface of ET and F₂TCNNQ single crystals as we are dealing with low ordered films and observe interdiffusion at the interface. Disorder prevents the molecular orbitals from forming bands which leads to a localisation of the charge carriers on their respective molecules. The charge transport is in this case dominated by thermally activated hopping. Moreover it is possible that the number of possibly delocalised electrons is too low to be detected by our spectrometer.

4.2.4 Summary of F₆TCNNQ based interfaces

After having discussed four different interfaces of F₆TCNNQ to other organic semiconductors in detail, a summarising comparison of the different heterojunctions is attempted in this section. It was found that F₆TCNNQ is a reliable electron acceptor that undergoes significant charge transfer when combined with donor molecules that fulfil the condition of having a smaller ionisation potential than the electron affinity of F₆TCNNQ. The charge transfer reaction manifested itself by additional species in the N1s core levels of F₆TCNNQ. Also, the C1s core levels showed additional species, that were however in some cases harder to analyse in detail, due to the overlap with the donor related C1s signals.

Fig. 4.31 shows the N1s spectra of thin layers of F₆TCNNQ on the four different donor molecules together with the F₆TCNNQ/Au interface and the (K⁺)(F₆TCNNQ⁻) charge transfer salt as reference in dependence of the ionisation energy. It becomes apparent

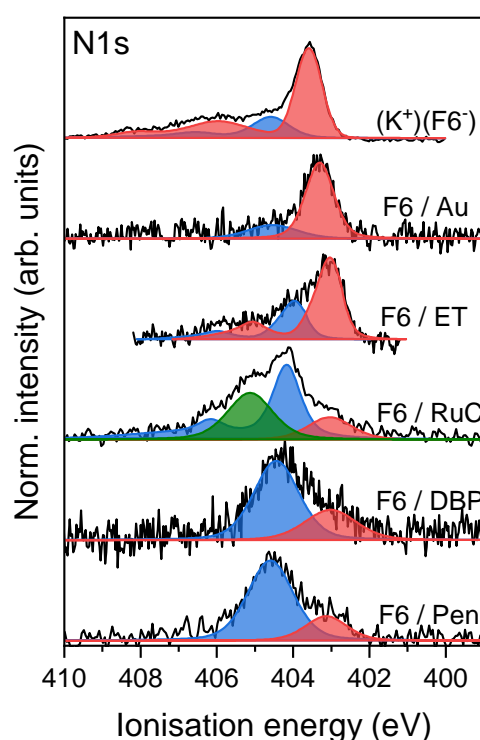


Figure 4.31: N1s core level spectra of thin F₆TCNNQ layers on the donor molecules pentacene (PEN), dibenzopentacene (DBP), *trans*-[Ru(dppe)₂(T)₂] (RuC) and BEDT-TTF (ET). The F₆TCNNQ/Au interface and the (K⁺)(F₆TCNNQ⁻) are shown as reference. Fits of neutral species are shown in black, of anionic F₆TCNNQ in blue and a third species that probably stems from local interactions of the nitrogen groups in green. Peak centre positions are indicated by dashed lines as guide for the eyes.

that in all four combinations, an additional species at lower ionisation energy is present which indicates a charge transfer reaction. Interestingly, the maxima of these features all lie at a similar ionisation energy of about 403.0 eV. This means that the electronic surrounding of the nitrogen atoms in the charged F₆TCNNQ molecules is similar for all investigated interfaces which in turn suggests an equivalent charge transfer reaction.

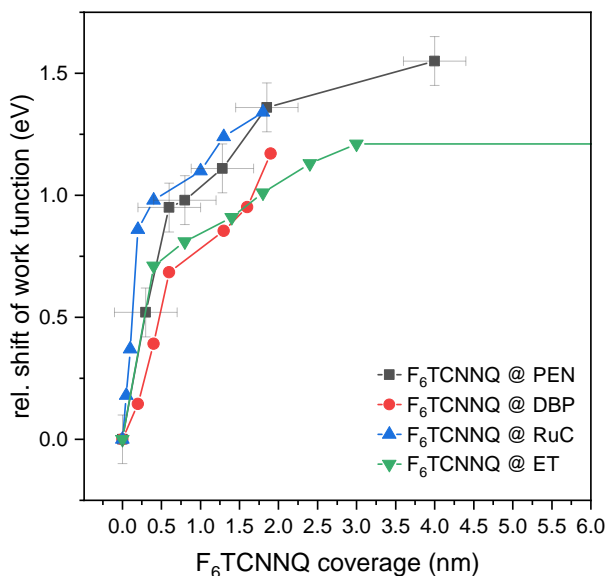


Figure 4.32: Comparison of the work function progression of the different F₆TCNNQ based interfaces investigated in this work, where F₆TCNNQ was deposited as top layer. Error bars are estimated as equal for all interfaces but are only shown for one curve for the sake of clarity.

However, it cannot be concluded with certainty that in all cases the charge transfer is of ionic character because a hybridisation of the frontier orbitals which does not drastically change the electron density around the nitrogen atoms is also a possible scenario. The interface involving the Ru-acetylide complex (RuC) is an exception, since it comprises an additional third species (green) besides the neutral (blue) and anionic (red) contribution. This is a sign for a local interaction, possibly a backdonation of charge, of some cyano groups of F₆TCNNQ with the ligand of the RuC. The width of the fitted peaks varies for the different interfaces which indicates differences in the structural arrangement and molecular order.

All investigated interfaces showed significant shifts of the vacuum level across the interface. As outlined in Sec. 2.3, such a shift is referred to as interface dipole and is a sign of charge rearrangements due to charge transfer at the interface. The progression of the work function for all discussed interfaces with F₆TCNNQ as top layer is shown in Fig. 4.32. Within the experimental uncertainty, all interfaces show a similar shift of the vacuum level. This suggests the formation of relatively sharp interfaces for all material combinations.

Deduced from the measured work functions and valence levels, a comparison of the energy level alignment for the different interfaces is shown in a simplified representation in Fig. 4.33. The vacuum level is shown in black and the evolution of the HOMO energy of the bottom (donor) material is depicted in blue starting on the left side. Furthermore, the HOMO position of neutral F₆TCNNQ was determined by taking the HOMO onset of thickest F₆TCNNQ overlayer for the respective interface and is shown in blue on the right. The anticipated LUMO position is depicted as red dashed line and was determined by taking into account the optical gap of 2.4 eV measured by optical absorption on F₆TCNNQ in solution (cf. Fig. 4.22). In the interface region, the occupied LUMO of F₆TCNNQ

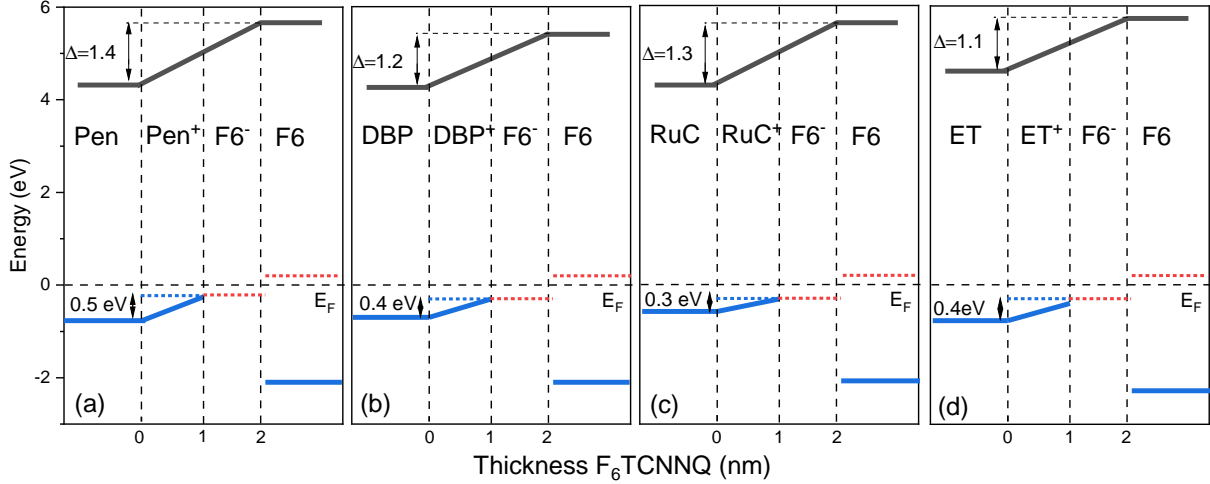


Figure 4.33: Comparison of energy level alignment of different F_6TCNNQ based interfaces. (a) F_6TCNNQ /pentacene, (b) F_6TCNNQ /dibenzopentacene, (c) F_6TCNNQ /*trans*- $[Ru(dppe)_2(T)_2]$ and (d) F_6TCNNQ /ET. The HOMOs of the respective materials are shown in blue, the LUMO of F_6TCNNQ is indicated as red dashed line because it could not be resolved due to the overlap with the donors HOMO. The progression of the vacuum level, determined from the high binding energy cutoff is shown in black.

could not be clearly distinguished from the HOMO position of the donor which is why both states are shown as dashed blue and red lines at the onset position of the highest measured occupied states. The energy values are referenced to the Fermi energy at 0 eV. The interface dipole Δ was defined in this representation as the vacuum level shift within the first 2 nm of F_6TCNNQ coverage.

The differences in the magnitude of the interface dipole are not correlated to the differences of the ionisation potentials of the donors to the electron affinity of F_6TCNNQ . As outlined in Sec. 2.3, the interface dipole is also sensitive to mutual polarisation effects, surface morphology and molecular orientation. Hence, the magnitude of the interface dipole is not only correlated to the magnitude of the charge transfer. The HOMOs of the donor materials all exhibit a shift to lower binding energies at the interfaces. However, all interfaces show non-vanishing hole injection barriers between 0.2 and 0.3 eV and are therefore semiconducting. From a solely electrostatic point of view, as in the model [64] introduced in Sec. 2.3, one would expect the frontier orbitals to follow the progression of the vacuum level. However, in analogy to XPS, the binding energy measured in UPS is not only sensitive to global potential changes but also to local screening effects (cf. Sec. 3.2.3), that are not considered in a purely electrostatic treatment of the system. Reduced charge density at the donor molecules leads to a diminished screening of the photohole and therefore to a higher ionisation energy. Screening effects can also stem from changes in molecular orientation at the interface which was also observed for other systems [181]. Although clear signatures of charge transfer were found for all F_6TCNNQ containing interfaces presented in this work with, occupied states directly at the Fermi level were not detected. This shows that the Fermi level in all systems was not pinned inside the partially filled LUMO of the acceptor or the partially unoccupied HOMO of the donor but clearly below. As discussed in Sec. 2.3, there is no scientific consensus about the origin

of the pinning levels. The mainly discussed suggestions are surface or defect induced intra gap states or the polaronic states of the respective molecules. As all investigated interfaces were built up of evaporated thin films on polycrystalline gold substrates, the presence of defects and molecular disorder is very likely. Since charge transfer and charge delocalisation is very sensitive on the orientation of the molecules π -electron systems to each other, it is possible that the formation of a 2-dimensional electron or hole gas is only achievable at highly ordered single-crystalline interfaces. This could possibly be realised in the future by the use of single crystalline substrates and epitaxial deposition with subsequent determination of the molecular order by microscopy or X-ray diffraction techniques. It is also possible that delocalised charges are present in small areas of the investigated samples but the resolution of the used photoemission setup is too low to detect them. The hole injection barrier (energy distance of HOMO to Fermi level) was determined by constructing the peak onset of the HOMO derived peak which does not consider the low binding energy tail of the peak. Moreover the satellite correction of the UPS spectra (cf. Sec. 3.2.2) adds an uncertainty that reduces the resolution. The addition of a monochromator to the setup or the use of a synchrotron source would avoid that and could possibly enable the detection of delocalised charges at such interfaces.

4.3 F₁₆CoPc based organic heterostructures

In the last chapter, various organic interfaces where F₆TCNNQ served as a molecular acceptor were investigated on a fundamental level. It was shown that F₆TCNNQ forms relatively sharp interfaces to all investigated donors and shows a charge transfer, that was probably ionic except in the case of the Ru acetylide complex. These findings represent a starting point for further research on F₆TCNNQ based heterojunctions and applications. This chapter will deal with another molecular acceptor, F₁₆CoPc, which belongs to the class of transition metal phthalocyanines (TMPc) (cf. Sec. 2.4). Its electron affinity determined by DFT calculations is 4.5 eV [93], whereas an experimental determination by e.g. inverse PES is not reported in literature. This value is significantly lower than that of F₆TCNNQ (5.6 eV), however, several studies found spectroscopic evidence for a charge transfer to molecules, some of which do not fulfil the condition $EA_{Acc} \geq IP_{Don}$ [182–184]. This interesting behaviour was explained by the particular nature of the Co3d_{z²} orbital of the central Co atom which is reduced from Co(II) to Co(I) without significant alteration of the ligand orbitals. This charge transfer ability, which is observed also at the interfaces of poly- [185] and single-crystalline gold [186], together with the high thermal and chemical stability and reliable growth properties of TMPcs makes F₁₆CoPc an attractive acceptor for the application in molecular electronic devices. Since a charge transfer reaction between F₆TCNNQ and dibenzopentacene (DBP) was addressed in Sec. 4.2.1, the interface between DBP and F₁₆CoPc will be discussed in the following section.

The second part of this chapter will deal with a rectifier based on a F₁₆CoPc / CuPc heterojunction which was fabricated by collaboration partners from the Institute for Integrative Nanosciences at the IFW Dresden. Its relevant interfaces were measured in our group's photoemission setup. Moreover, the influence of different processing conditions on its electronic landscape was studied.

4.3.1 Interface to dibenzopentacene

The interface between F₆TCNNQ and dibenzopentacene (DBP), which was discussed in Sec. 4.2.1, showed clear signs of a charge transfer but no indication for metal-like delocalisation of charge carriers. Furthermore, a broadening of core level peaks signalled significant disorder at the interface. Since F₁₆CoPc is a larger molecule with higher symmetry, a sharper and more ordered interface formation might be expected.

Fig. 4.34 shows the XPS spectra of the relevant core levels of a DBP film with subsequent incremental deposition of F₁₆CoPc. The C1s spectra, shown in the left panel of Fig. 4.34, evolve gradually from the known single peak structure of DBP into the F₁₆CoPc spectrum which consists of several peaks due to the different configurations of carbon atoms in F₁₆CoPc. The peak at 290.4 eV can be attributed to aromatic carbon, the one at 291.7 eV to the carbon bound to nitrogen and the one at 292.6 eV to carbon bound to fluorine, whereas the peak at 294.5 eV is due to a π - π^* shake-up transition [187, 188]. No obvious changes in the C1s spectra are visible, although the complex nature of the spectra with the many different carbon contributions makes a detailed analysis difficult. The N1s spectrum (centre panel in Fig. 4.34) comprises one peak since the nitrogen positions in the F₁₆CoPc molecule are equivalent. Also here, no coverage dependent changes are observable, which indicates that the chemical environment at the nitrogen sites at the

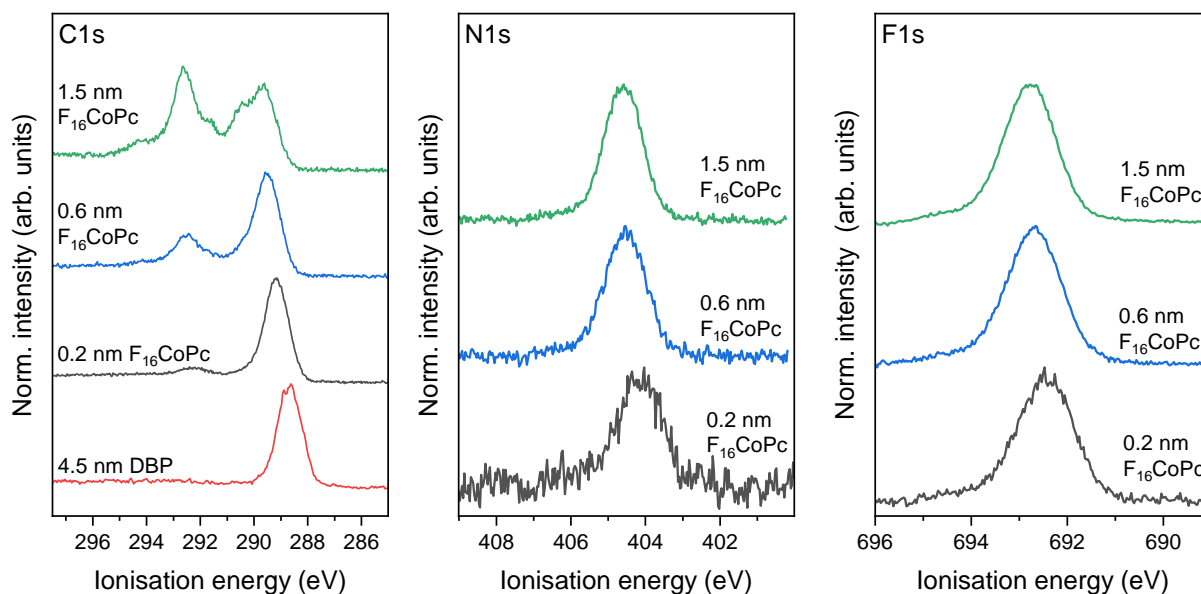


Figure 4.34: C1s (left), N1s (centre) and F1s (right) spectra of a dibenzopentacene film with subsequent incremental deposition of F₁₆CoPc.

interface is not different to that in the film. The same behaviour is observed in the F1s spectra (right panel in Fig. 4.34).

By contrast, clear thickness dependent changes are visible in the Co2p spectra, displayed in the left panel of Fig. 4.35. The "bulk" spectrum of F₁₆CoPc, represented by the green curve, consists of a large peak centred at 786.3 eV and a smaller one at 788.2 eV, which is a satellite feature stemming from multiplet splitting due to the interaction of unpaired electrons in the photoemission final state [185]. For lower coverages, the satellite feature is less pronounced, and a third peak arises which is shifted by about 2.3 eV to lower ionisation energies compared to the main neutral line. Similar Co2p interface spectra were observed before for F₁₆CoPc and related Co containing compounds on various metal substrates [185, 189–192], as well as for the organic interfaces of F₁₆CoPc to rubrene [183] and MnPc [182]. The new feature at lower binding energy is explained by a charge transfer to the Co 3d_{z²} orbital leading to a reduction of the Co centre from Co(II) to Co(I). The fact that the C1s, N1s and F1s spectra remain unchanged show that in contrast to other TMPs, the ligand remains largely unaffected by the charge transfer. This is explained in literature by the special nature of the half filled d_{z²} orbital, which is oriented perpendicular to the substrate for flat-lying molecules [184, 192].

Insight into the electronic structure at the interface region near the Fermi level can be gained by the UPS spectra, shown in Fig. 4.35. The centre panel shows the raw spectra in the ionisation energy region from 4 to 12 eV. From the onset of the pristine DBP spectrum (red curve) an ionisation potential of 5.2 eV can be determined, which is in agreement with previous measurements on DBP. The spectrum of 1.5 nm F₁₆CoPc coverage has an onset at about 6.4 eV. In a recent publication, the electronic gap of F₁₆CoPc determined by STM on a monolayer of molecules on a h-BN/Cu(111) substrate is 2.1 eV [193]. This would yield an electron affinity of 4.3 eV which is considerably smaller than the ionisation potential of DBP. The fact that a charge transfer is still observed, underlines the special property of the Co d_{z²} orbital. The right panel of Fig. 4.35 shows the zoomed in region

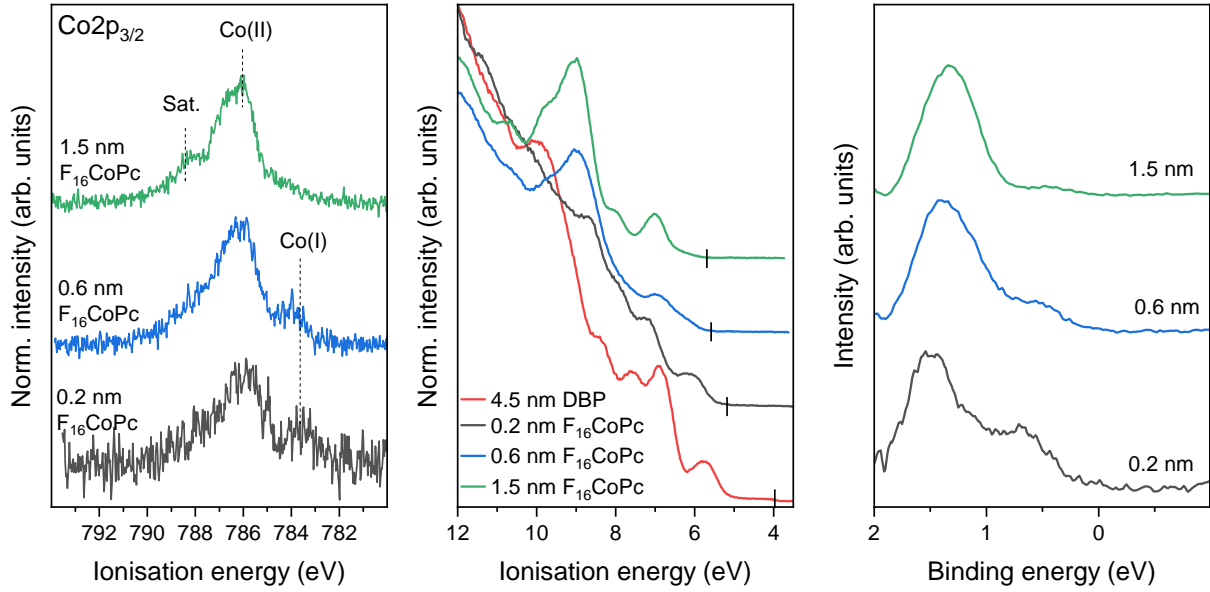


Figure 4.35: Left: $\text{Co}2p_{3/2}$ core level spectra of F_{16}CoPc deposited incrementally on a dibenzopentacene film. Centre: UPS spectra of the interface. Fermi level position is indicated by black lines. Right: Same spectra after subtraction of pristine dibenzopentacene spectrum in dependence of binding energy relative to Fermi level.

close to the Fermi level of the same spectra, but in dependence of the binding energy relative to the substrate's Fermi level and after subtraction of the pristine DBP spectrum. It becomes apparent that for low coverages an additional occupied state, centred approx. 0.9 eV below the HOMO of neutral F_{16}CoPc is observed. Of course, this state must stem from the filled $\text{Co}3d_{z^2}$ orbital. With increasing F_{16}CoPc film thickness its intensity decreases because only the first few molecular layers are reduced. Occupied states directly at the Fermi level that would imply the formation of a 2-dimensional electron or hole gas are not detected for this interface. As discussed in Sec. 4.2.4, it is possible that small areas of the interface turn metallic but due to the limited instrumental resolution these states are not resolved. In a previous study on the interface between single-crystalline rubrene and F_{16}CoPc , enhanced conductivity and a band-like temperature dependence of the resistivity was measured [18]. The UPS spectra of the corresponding thin film interface were similar to those shown in Fig. 4.35 (centre). Transport and Hall effect measurements of $\text{F}_{16}\text{CoPc}/\text{DBP}$ and $\text{F}_6\text{TCNNQ}/\text{DBP}$, which both showed clear signs of charge transfer in their photoemission spectra, could lead to interesting results in that regard.

4.3.2 Phtalocyanine heterojunction in an integrated molecular diode

Organic semiconductors offer some advantages that inorganic semiconductors do not have. These include lower energy consumption for processing molecular materials, the possibility of using flexible polymer foils as substrates and potentially a large flexibility regarding the tailoring of electronic properties by means of organic chemistry. On the other hand, there are important drawbacks, such as a low charge carrier mobility and weak durability at high temperatures, under radiation or contact to oxygen. Achieving progress in these areas regarding the basic understanding of the underlying mechanisms and the improvement of material and device properties is a matter of current research.

Organic semiconductor films of several hundred nanometres are already widely used in LEDs (OLEDs) and possibly close to marketability in organic photovoltaic cells. An application area that is still limited to lab experiments is the field of molecular electronics which refers to electronic devices based on single molecules or assemblies of molecules on the scale of a few nanometres [194]. This could potentially enable further miniaturisation of electric circuits and lead to novel applications.

A rectifier is a simple device, often based on a semiconductor diode, which transforms alternating current (AC) into direct current (DC). One potential application of organic based rectifiers is as low-cost components of radio-frequency identification tags where a rectifier is used for converting electromagnetic radiation into DC [195]. This section will address the electronic properties of a rectifier based on a F₁₆CoPc/CuPc heterojunction between two gold contacts. The results discussed in the following were published in Ref. [196].

The maximum operating frequency (f_{max}) of a diode-based rectifier is given by $f_{max} \propto \mu/L^2$ where μ is the mobility and L is the thickness of the semiconductor layer, if the leakage current is negligible [197]. Thus, by using a semiconductor thickness in the nanometre range and assuming a (for organics) high mobility in the range of $1 \text{ cm}^2 \text{ V}^{-1} \text{ s}^{-1}$, a rectification ratio in the THz range is theoretically predicted. While rectification in the GHz and THz range was demonstrated in prototypical molecular systems [198, 199], integrated molecular devices with such a frequency performance have not been reported yet. One challenge in the fabrication of such a device is the deposition of the top metal electrode because due to the large distance between adjacent molecules, a penetration of metal into the organic film is often observed [200]. Especially in molecularly thin films, this could lead to a short circuit of the device. This problem is avoided by using a special fabrication process, developed by our collaboration partners at the Institute for Integrative Nanosciences at the IFW Dresden [201–203], which involves a rolled up micro-tube as a soft top contact. As the organic semiconductor spacer, copper phtalocyanine (CuPc) (cf. Sec. 2.4) was chosen, because it has proven good processability and chemical and thermal stability in the past [204–206].

The performance of devices based on organic semiconductors significantly depends on the charge carrier mobility and on the energy level alignment at the interfaces, which controls charge injection into the organic film [163]. The mobility is very sensitive to the molecular order which is why in previous studies thin inserted interlayers were used to improve the crystallinity [207]. Planar organic molecules that are evaporated onto metal electrodes tend to orient in a face-on orientation in the first couple of layers due to the electronic

interaction of the organics π -system with the metal. The following layers gradually take on a more edge-on orientation. An interlayer could decouple the organic layer from the metal which would prevent this change in molecular order. Another approach to improve the electric performance is the rearrangement of carriers by either doping or the introduction of a heterojunction. The latter was used in previous studies where an acceptor layer was introduced between electrode and organic transport layer to increase carrier concentration at the interface and reduce the hole injection barrier from the electrode due to a charge transfer between the acceptor and the electrode and/or the acceptor and the other organic [145, 208, 209]. Therefore, in the present device, 1 nm of fluorinated cobalt phthalocyanine ($F_{16}CoPc$) was introduced between the bottom Au electrode and the CuPc layer.

The fabrication procedure was as follows: A finger-shaped mesa structure is formed by selective etching with HF on a Si(100) wafer with 1 μm SiO_2 . Then, a sacrificial layer of GeO_x with a strained metallic structure of Au/Ti/Cr (from top to bottom) is deposited by electron beam deposition. The strain gradient between the Cr and Ti layer leads to a rolling up of the structure after the removal of the GeO_x sacrificial layer in acetone or deionised H_2O . Before the roll up process, the bottom Au electrode was deposited which was followed by the thermal evaporation of the organic layers. Afterwards, the sample was taken out of the vacuum chamber and the self roll-up was performed to ensure a damage free top contacting of the structure. A visualisation of the device structure with corresponding microscope and AFM images, done by our collaborators, is shown in Fig. 4.36. Grazing incidence X-ray diffraction measurement showed that with and without the $F_{16}CoPc$ interlayer, the CuPc molecules predominantly arranged in an edge-on orientation. A face-on orientation would be more beneficial regarding charge transport in the out-of-plane direction, due to a maximum overlap of the pi-orbitals [210]. However, the crystallinity of the CuPc film deposited on Au/ $F_{16}CoPc$ was improved compared to a film that was directly evaporated on the Au bottom electrode which is also expected to improve the transport properties.

Photoemission can provide vital insight into the energy level alignment at interfaces which often is required for a microscopic understanding of the device functionality regarding charge transport and injection. Hence, XPS and UPS measurements of the device architecture was provided by our group. For that, a Si substrate with the equal multi-layer structure as for the device fabrication (Si/Cr/Ti/Au from bottom to top) was used. The substrate was not sputter-cleaned in order to provide the same conditions as were present during device fabrication. After measuring the Au surface, the organic films were deposited incrementally with UPS and XPS measurements being conducted after each deposition step. The sample had a predetermined breaking point so that after the heterojunction was completed, the sample was taken out of the measurement chamber and one half of the sample was rinsed with water and the other one with acetone which were the two possible environment the roll-up process was conducted in. Lastly, both pieces of the sample were measured in order to study the influence of the different treatment on their electronic properties.

As became apparent in the discussion of the $F_{16}CoPc/DBP$ interface in the previous section (4.3.1) and in other studies, if a charge transfer takes place, charge is transferred predominantly to the Co centre of $F_{16}CoPc$. The left panel of Fig. 4.37 shows the evolution of the $\text{Co}2p_{3/2}$ peak with incremental deposition of first the $F_{16}CoPc$ interlayer and

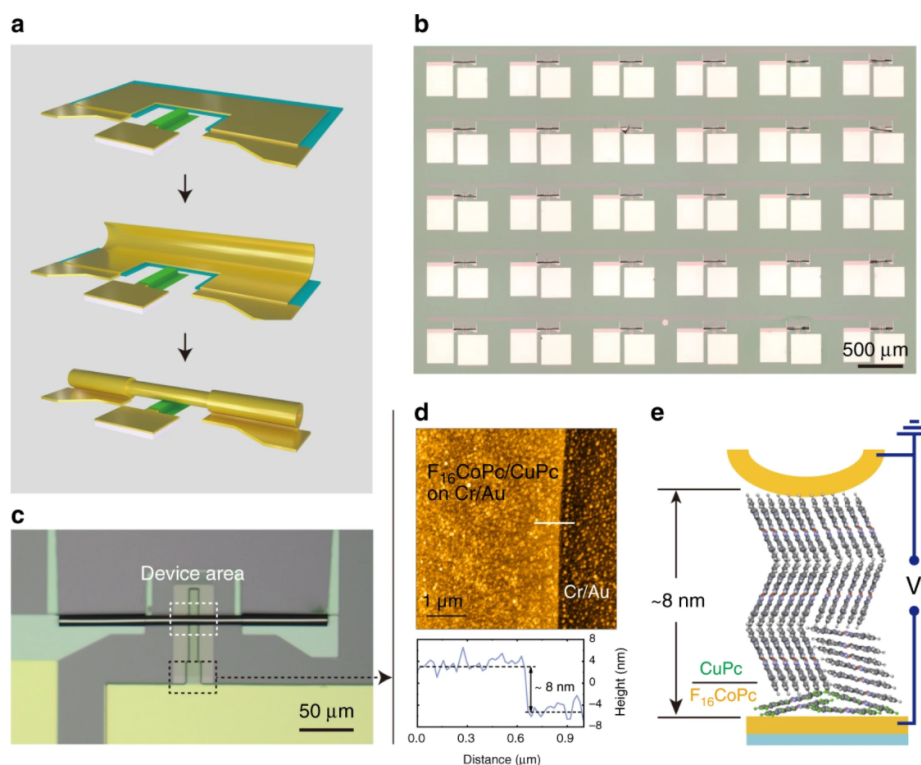


Figure 4.36: Overview of device set-up and fabrication process, conducted by our collaboration partners. (a) Self roll-up process. (b) Microscope image of the device array. (c) Close-up of a single device. (d) Tapping mode AFM image of $F_{16}CoPc(1\text{ nm})/CuPc(7\text{ nm})$ grown on mesa (as marked in c by black dotted box) and corresponding height profile. (e) conceptual visualisation of $Au(\text{finger})/F_{16}CoPc(1\text{ nm})/CuPc(7\text{ nm})/Au(\text{tube})$. Figure created by collaboration partners [196].

then the CuPc transport layer. Starting from the bottom spectrum, it shows two species that were also observed in the $F_{16}CoPc/DBP$ interface and are assigned to the oxidation states of Co(II), the normal configuration of the metal centres in TMPcs, and Co(I), which arises due to a charge transfer from the Au substrate to $F_{16}CoPc$. Charge transfer from a gold single crystal was reported previously [184], however in the present structure the gold electrode is polycrystalline and not sputter cleaned after insertion in the vacuum chamber, which manifested itself by contamination related N1s, O1s and C1s core level peaks detected by XPS. With increased thickness of $F_{16}CoPc$, the contribution of the Co(I) feature decreases, which is in accordance with a charge transfer that is restricted to the first couple of molecular layers. Panel (b) of Fig. 4.37 shows the evolution of the ratio Co(I)/Co(II) in dependence on the deposition steps. During the incremental deposition of CuPc, the Co(I) species initially decreases further but then increases again. This behaviour was also observed for other interfaces discussed in this thesis and can be rationalised taking into account the limited information depth of XPS. With increased CuPc thickness the information window shifts upwards and the share of the $F_{16}CoPc/CuPc$ interface region to the overall Co2p signal becomes larger. Importantly, this indicates that also from the CuPc layer, electrons are transferred to $F_{16}CoPc$.

No changes are observed in the $Cu2p_{3/2}$ spectra of CuPc across the heterojunction as can

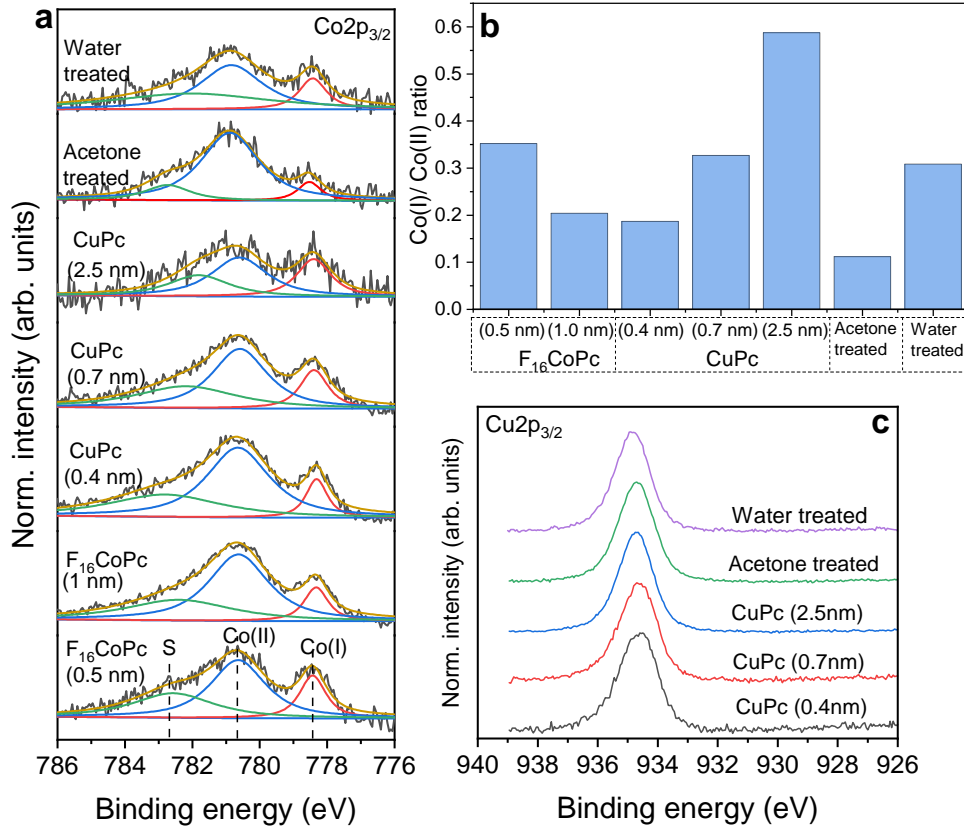


Figure 4.37: (a) $\text{Co}2p_{3/2}$ core level of the Au/ F_{16}CoPc / CuPc system after each processing step with fitted Co(I) , Co(II) and satellite (S) contributions. (b) Peak area ratio of $\text{Co(I)}/\text{Co(II)}$. (c) $\text{Cu}2p_{3/2}$ spectra show no changes across the heterojunction. Adapted from [196].

be seen in panel (c) of Fig. 4.37. This is expected, since it is known that contrary to CoPc , in CuPc charges are transferred predominantly from the ligand and not from the metal centre [184]. However, nitrogen and carbon are present in both molecules which is why an identification of the charge transfer in the CuPc related XPS spectra is not possible in this system.

Continuing the discussion with the valence region, we turn our attention to the UPS spectra, shown in Fig. 4.38. Panel (a) shows the high binding energy cutoffs and panel (b) the low binding energy region of the heterojunction. The HOMO positions are determined by the positions of the onset and are displayed in panel (c) together with the evolution of the work function. The blue curve shows the occupied $\text{Co}3d$ derived LUMO of F_{16}CoPc , centred at an energy of about 0.5 eV in analogy to the $\text{F}_{16}\text{CoPc}/\text{DBP}$ interface in Sec. 4.3.1. It becomes apparent that the now singly occupied former LUMO of F_{16}CoPc (LUMO* in Fig. 4.38) bends down towards the Au/ F_{16}CoPc interface, while the HOMO of CuPc bends up towards the $\text{F}_{16}\text{CoPc}/\text{CuPc}$ interface. This indicates an ohmic contact between the electrode and F_{16}CoPc , and a charge carrier accumulation in the contact region, which is expected for a semiconductor metal contact where the semiconductor's work function is larger than the metal's [211]. To estimate the distribution of holes in the CuPc layer, the following equation for the occupation probability P from traditional semiconductor

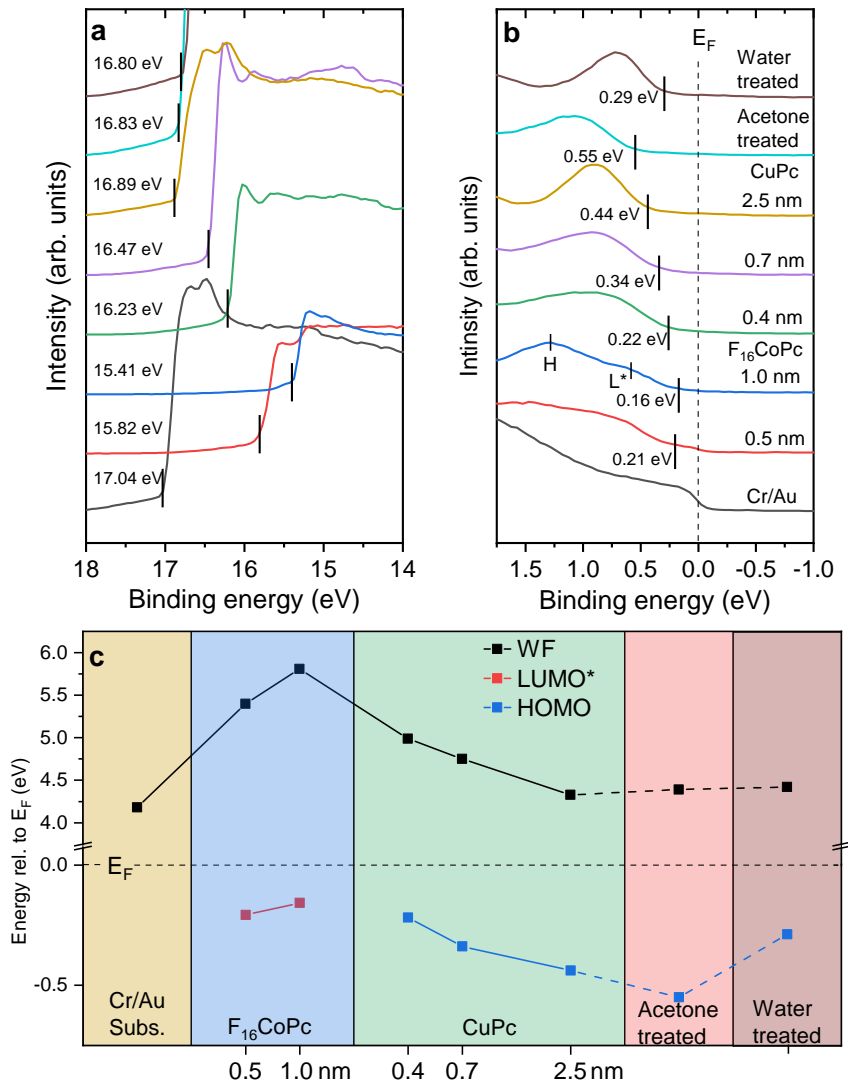


Figure 4.38: High binding energy cutoffs (a) and valence region (b) of the Cr/Au/F₁₆CoPc/CuPc system measured by UPS. (c) Evolution of the work function (WF), partially filled LUMO of F₁₆CoPc (LUMO*) and HOMO of CuPc relative to Fermi level of the Cr/Au substrate. Adapted from [196].

physics is applied [212]:

$$P(x) = N_v \exp\left(-\frac{E_F - E_v(x)}{k_B T}\right), \quad (4.1)$$

with the effective density of states for holes in the valence band (or HOMO) N_v , the Fermi level E_F , the upper edge of the valence band at position x , the Boltzmann constant k_B and the temperature T . The density of states in organic semiconductors is usually described by a Gaussian to account for static and dynamic disorder. However, for our estimation it is sufficient to calculate the ratios $P(x=0.4 \text{ nm})/P(x=0.7 \text{ nm})$ and $P(x=0.4 \text{ nm})/P(x=2.5 \text{ nm})$ where N_v cancels out. With $k_B T=0.025 \text{ eV}$ at 300 K and the values for E_V extracted from the UPS measurements, eq. 4.1 yields 103.5 and 4964.2 respectively, which illustrates the significantly increased hole concentration in CuPc at the interface to F₁₆CoPc compared to the bulk.

Apart from the Au(finger)/F₁₆CoPc(1 nm)/CuPc(7 nm)/Au(tube) architecture, several other devices were fabricated to investigate the influence of the F₁₆CoPc interlayer on the device performance. These were devices without the F₁₆CoPc interlayer and devices with reversed order where the F₁₆CoPc layer is on top of the CuPc layer. Moreover, the self roll-up process was performed in acetone and in deionised water to evaluate which processing conditions are more advantageous.

From the UPS spectra in Fig. 4.38, it becomes obvious that the treatment with acetone leads to an increase of the distance between HOMO and the Fermi level (hole injection barrier) of CuPc compared to the water treated devices. This manifests itself in the I-V curves of the different devices, measured by our collaborators, which are shown in Fig. 4.39 (a). The tube electrode was held at ground while the voltage was applied to the Au finger electrode, scanning from negative to positive. Water treated devices show a much higher forward current density and rectification ratio than acetone treated ones. Further insight into the transport mechanisms in the devices can be gained by analysing the I-V curves in a double logarithmic representation, which are displayed in Fig. 4.39 (b). Both curves show three different regimes that can be distinguished by the exponent of m in the relation $I \propto V^m$. This behaviour is typical for an insulator with traps sandwiched between two metal electrodes with ohmic charge injection [213–215]. The first regime with a slope around 1 occurs at low voltages when the current is dominated by thermally generated charge carriers and is referred to as ohmic regime. At a certain voltage, the injected carrier concentration exceeds that of the thermally generated and the current would become space charge limited which is characterised by a slope of 2. However, disordered organic films comprise traps which immobilise a significant amount of charge carriers which leads to trap-limited current with slopes larger than 2. Apparently, in the present devices, two trap-limited regimes with slopes of 2.15 and 3.38 are observed, which are assigned to shallow- and deep-trap limited current [214]. A complete filling of the traps and a subsequent quadratic dependence of J on V did not occur at voltages below 5 V. The trap densities for acetone and water treated devices were estimated to be $2.7 \cdot 10^{18}$ and $1.58 \cdot 10^{18} \text{ cm}^{-3}$, respectively (details on this estimation can be found in Ref. [196]). Thus, acetone treatment leads to an increase of the hole injection barrier and creates more traps compared to water treatment.

Fig. 4.39 (a) also shows that devices based on the Au(finger)/F₁₆CoPc/CuPc/Au(tube)

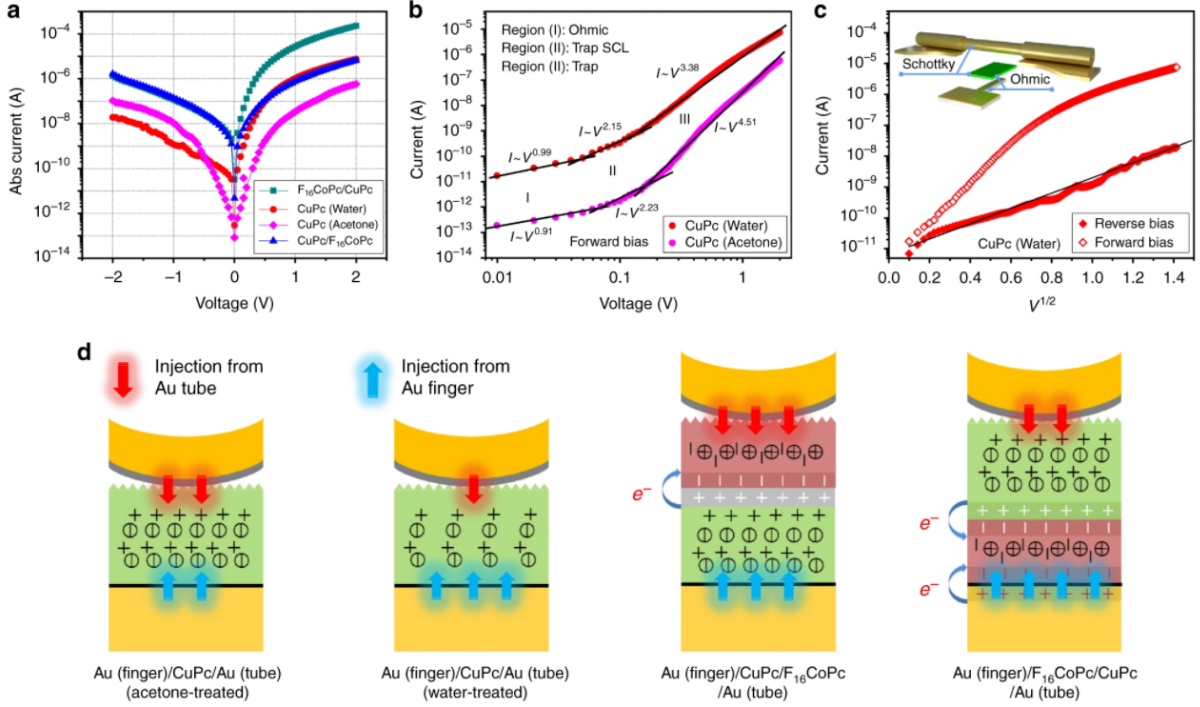


Figure 4.39: (a) I-V curve of devices based on different architectures as measured by our collaboration partners. (b) Log-log plot of the I-V curves of diodes based on acetone- and water-treated Au(finger)/CuPc(7nm)/Au(tube), exhibiting three transport regimes distinguished by different m in $I \propto V^m$. (c) $\log(I)$ versus $V^{1/2}$ plot for water treated Au(finger)/CuPc/Au(tube) diode to showing linear progression under reverse bias which indicates Schottky type injection at tube electrode. (d) Schematic visualisation of electrical properties of different device architectures. Plots and illustrations were created by collaboration partners [196].

sequence exhibit a higher current for forward and reverse bias than devices without the F₁₆CoPc interlayer. This is ascribed to the improved crystallinity and the increased carrier density induced by the F₁₆CoPc layer. Interestingly, the rectification ratio is lower (300 at ± 2 V) than for water treated devices without a F₁₆CoPc interlayer (around 400 at ± 2 V). This finding suggests that the rectifying behaviour does not stem mainly from the organic heterojunction at the bottom contact but from the CuPc/Au(tube) top contact. Fig. 4.39 (c) shows the plot of $\log(I)$ versus $V^{1/2}$ for a water treated Au(finger)/CuPc/Au(tube) device. Obviously a linear relationship is present under reverse bias but not under forward bias. This indicates a Schottky type contact at the CuPc/Au(tube) interface [216], which leads to the question whether this difference between top and bottom electrode contact stems from the electronic properties of the Au tube electrode.

To investigate this, the layer sequence Cr(20 nm)/Ti(15 nm)/Au(5 nm)/Ge(10 nm) was deposited on a Si wafer and the Ge layer was dissolved in deionised water before transferring the sample into the photemission setup. As becomes apparent from Fig. 4.40, the kinetic energy of the cutoff of the mimicked "Au tube" was measured to be 16.9 eV compared to 17.04 eV, which was measured for the Au finger electrode (cf. Fig. 4.38). This yields very similar work functions of 4.31 eV for the Au tube and 4.17 eV

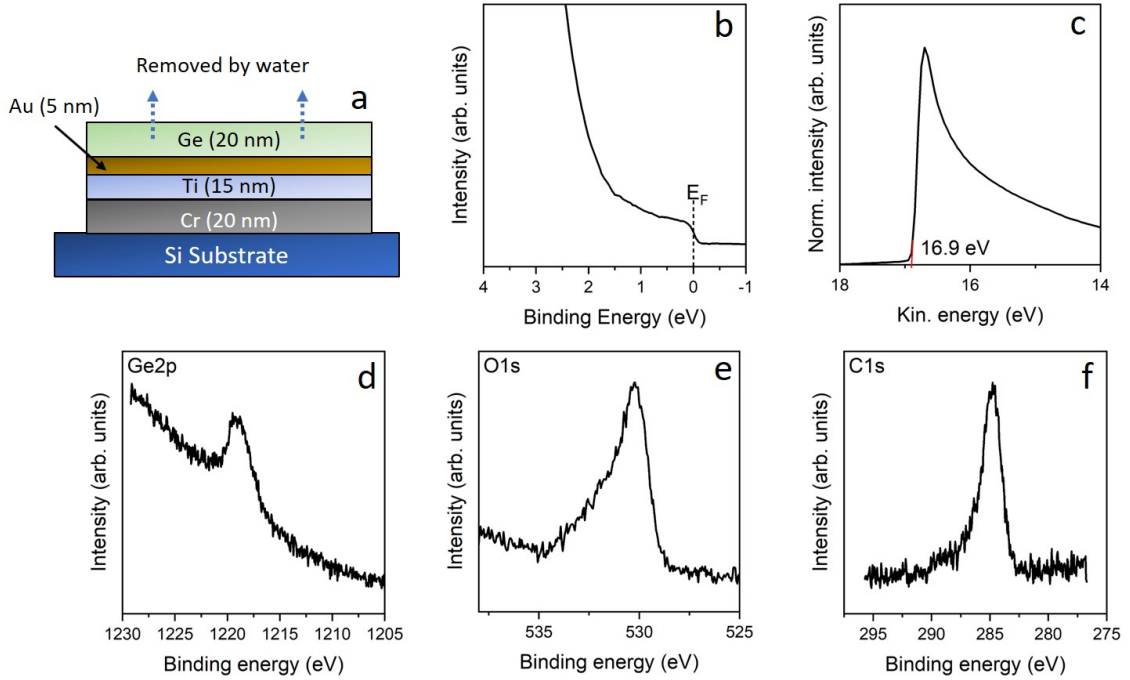


Figure 4.40: (a) Scheme of the sample design to mimic the top tube electrode for photoemission measurements. Valence region (b) and high binding energy cutoff (c) measured by UPS. (d-f) XPS spectra of relevant core levels. Adapted from [196].

for the Au finger electrode. Hence, the different injection mechanisms must be due to the different preparation routes of the two contacts. The bottom interface was formed by evaporation of CuPc in ultra-high vacuum onto the finger electrode, while the top contact was formed in water by mechanical contact after the self roll-up.

Lastly, the rectification behaviour of $F_{16}CoPc$ containing devices with reversed layer sequence, Au(finger)/CuPc/ $F_{16}CoPc$ /Au(tube), is discussed. As can be seen in Fig. 4.39 (a), the I-V curve of this device is nearly symmetric with a decreased current under forward bias and an increased one under reverse bias. This behaviour makes sense because the $F_{16}CoPc$ interlayer improves the charge injection from the Au tube into the CuPc layer while the injection from the bottom electrode is diminished. A visualisation of the electronic performance of all device configurations is shown in Fig. 4.39 (d).

Summarising, the electronic properties of fully integrated rectifiers based on a molecularly thin organic hybrid layer ($F_{16}CoPc/CuPc$) were analysed. The devices were fabricated by collaboration partners with a special roll-up nanotechnology. Based on photoemission studies, it was shown that the rectifying behaviour of the Au(finger)/ $F_{16}CoPc/CuPc/Au$ (tube) device originates from the different injection mechanisms at the gold contact (Ohmic vs. Schottky type) rather than from the $F_{16}CoPc/CuPc$ junction. An explanation for this might be the small thickness of the organic heterojunction. A previous study on a $F_{16}CuPc/CuPc$ rectifier found an accumulation width of 10 nm thickness which would mean in our case that the organic thin film structure is fully accumulated and that the barrier stemming from the organic interface is negligible. How-

ever, the F₁₆CoPc interlayer improved the conduction properties which lead to a stable operation of the rectifier up to 10 MHz (frequency dependent performance characterisation in Ref. [196]).

5 Conclusion and Outlook

In the present work, several charge transfer systems based on organic donors and acceptors were studied with photoemission spectroscopy. Our aim was to find pairs that undergo an as large as possible charge transfer and to determine whether this leads to new electronic properties at the interface or in a blended film between both materials. In order to investigate properties of low ordered thin films that are also relevant for possible applications, the films were prepared on polycrystalline gold substrates. For most systems, the acceptor F₆TCNNQ was used due to its electron affinity which is one of the largest known. As reference, an F₆TCNNQ film was intercalated with potassium which lead to an integer charge transfer of ionic character yielding a charge transfer salt (K⁺)(F₆TCNNQ⁻) and enabled the identification of the anionic F₆TCNNQ spectrum. It was found that the core level spectra did not change their shape but were shifted by at least 1 eV to higher binding energies and that the valence spectrum changed significantly due to a polaronic relaxation of the molecule due to a filling of the LUMO. The same spectral characteristics were found at the interface between F₆TCNNQ and the gold substrate which shows that a layer of reduced F₆TCNNQ is formed.

Following this, several donor type molecules were paired with F₆TCNNQ. The prototypical polycyclic hydrocarbon pentacene and its close relative dibenzopentacene (DBP) which only differs by two additional benzene rings were used to form charge transfer interfaces with F₆TCNNQ. The aim was to compare both systems and to determine whether the structural difference between bot polycyclic hydrocarbons leads to different charge transfer behaviour. It was found that a charge transfer is present at both interfaces which is slightly stronger for DBP. This is attributed to the different morphology rather than to differing electronic properties of the two hydrocarbons. The charge transfer lead to a shift of the Fermi level towards the HOMO of the hydrocarbons but the films remained semiconducting. In addition, DBP and F₆TCNNQ were co-evaporated to achieve a blended film. It was found that the valence spectrum of the blend was determined by electrostatic interactions rather than charge transfer. Annealing lead to a strong charge transfer reaction which was reflected in significant changes in valence and core level spectra.

Another measurement series was dedicated to *trans*-[Ru(dppe)₂(T)₂], a novel large acetylide complex which was synthesized by collaboration partners and could potentially serve as a building block for molecular wires. After characterising it in pristine form, a charge transfer interface with F₆TCNNQ was formed. Clear signs of a charge transfer were found in the Ru3d core level, which was accompanied by the signature of an ionic charge transfer in the N1s spectrum of F₆TCNNQ known from (K⁺)(F₆TCNNQ⁻). However, a second additional species was detected in the N1s spectrum for which the most probable explanation is a partial hybridisation of the cyano groups with the ligands of *trans*-[Ru(dppe)₂(T)₂].

The third donor molecule investigated in this work was ET, an organosulfur compound

which gained a lot of attention as cation in organic superconductors. Interfaces with F₆TCNNQ and the smaller "weaker" acceptor F₂TCNQ were compared, since previous reports suggested band-like conduction at the ET/F₂TCNQ interface. Several differences between the combinations were found. The degree of charge transfer was larger for F₆TCNNQ/ET and a significant diffusion of F₂TCNQ into ET was observed. The charge transfer was detected in the S2p spectra of ET in form of two additional species due to an uneven HOMO distribution on the ET molecule. Additional occupied states in the former gap of the acceptors were found, but both interfaces remained semiconducting.

F₆TCNNQ proved as a reliable acceptor which was easy to evaporate in vacuum and showed good stability. However, the amount of molecules that underwent charge transfer differed strongly for the investigated interfaces, despite the similar ionisation potential of the different donors. This indicates that the charge transfer significantly depends on the molecular orientation. Also, annealing lead to a strong diffusion of F₆TCNNQ into the PCHSs and even the large Ru acetylide complex, which resulted in a larger amount of detected charged molecules.

Moreover, interfaces with the fluorinated phthalocyanine acceptor F₁₆CoPc were investigated. The F₁₆CoPc/DBP interface showed a charge transfer to the central Co 3d_x² orbital which was in agreement with previously studied interfaces involving this acceptor. Further investigations were conducted at the device relevant interfaces of a rectifier diode, made by collaboration partners. It was built up of a molecularly thin heterojunction of the phthalocyanines F₁₆CoPc and CuPc that were evaporated on a bottom gold electrode and top-contacted by a gold tube, fabricated by a self roll-up technology. Photoemission showed a charge accumulation in the F₁₆CoPc layer due to charge transfer from the bottom gold contact as well as from the CuPc layer. This lead to an improvement of the conductivity through the multilayer structure and therefore to a better device performance compared to a sample without an F₁₆CoPc interlayer.

All investigated interfaces presented in this thesis showed charge transfer. However, all remained semiconducting with the smallest hole injection barrier, determined by the HOMO onset, at about 0.1 eV for the F₆TCNNQ/pentacene combination. A possible explanation could be that the low order of thermally deposited thin films prevents the formation of a sharp interface and therefore leads to a localisation of charge carriers on the respective molecules. Therefore, it might be only possible to create 2-dimensional electron or hole gases at highly ordered interfaces. A route to achieve this could be the use of single-crystalline substrates or pre-structured templates. Molecules which comprise functional groups that improve the ordering of molecules in evaporated thin films could be another possibility. Also, in-situ measurements of the molecule orientation by X-ray absorption spectroscopy or scanning probe microscopy would be advantageous which was not available in the used setup. On the other hand, it is possible that small areas of the prepared samples turned metallic, but the available resolution was too low to detect the involved electrons. To answer this question, conductivity measurements on the most promising interfaces could be interesting. To resolve very small densities of occupied states at such interfaces, photoemission measurements at a synchrotron source could lead to interesting results.

Bibliography

- [1] A. Pochettino and A. Sella, *Acad. Lincei Rend* **15**, 355 (1906).
- [2] W. Pauli, *Annalen der Physik* **345**, 677 (1913).
- [3] H. Inokuchi, *Bulletin of the Chemical Society of Japan* **27**, 22 (1954).
- [4] H. Shirakawa, E. J. Louis, A. G. MacDiarmid, C. K. Chiang, and A. J. Heeger, *Journal of the Chemical Society, Chemical Communications*, 578 (1977).
- [5] C. W. Tang, *Applied physics letters* **48**, 183 (1986).
- [6] C. W. Tang and S. A. VanSlyke, *Applied physics letters* **51**, 913 (1987).
- [7] A. Tsumura, H. Koezuka, and T. Ando, *Applied Physics Letters* **49**, 1210 (1986).
- [8] X. Yang and L. Ding, *Journal of Semiconductors* **42**, 090201 (2021).
- [9] B. Lüssem, M. Riede, and K. Leo, (2013).
- [10] I. Salzmann and G. Heimel, *Journal of Electron Spectroscopy and Related Phenomena* **204**, 208 (2015).
- [11] I. Salzmann, G. Heimel, M. Oehzelt, S. Winkler, and N. Koch, *Accounts of chemical research* **49**, 370 (2016).
- [12] I. E. Jacobs and A. J. Moulé, *Advanced Materials* **29**, 1703063 (2017).
- [13] K. P. Goetz, D. Vermeulen, M. E. Payne, C. Kloc, L. E. McNeil, and O. D. Jurchescu, *Journal of Materials Chemistry C* **2**, 3065 (2014).
- [14] T. Naito, *Crystals* **11**, 838 (2021).
- [15] H. Alves, A. S. Molinari, H. Xie, and A. F. Morpurgo, *Nature materials* **7**, 574 (2008).
- [16] Y. Takahashi, K. Hayakawa, K. Takayama, S. Yokokura, J. Harada, H. Hasegawa, and T. Inabe, *Chemistry of Materials* **26**, 993 (2014).
- [17] R. M. Pinto, E. M. Maçôas, and H. Alves, *Journal of Materials Chemistry C* **2**, 3639 (2014).
- [18] Y. Krupskaya, F. Ruckerl, M. Knupfer, and A. F. Morpurgo, *Advanced Materials Interfaces* **3**, 1 (2016).
- [19] T. Shimada, Y. Takahashi, J. Harada, H. Hasegawa, and T. Inabe, *J. Phys. Chem. Lett* **9**, 424 (2018).
- [20] J. R. Kirtley and J. Mannhart, *Nature materials* **7**, 520 (2008).
- [21] J. E. Lennard-Jones, *Transactions of the Faraday Society* **25**, 668 (1929).
- [22] G. N. Lewis, *Journal of the American Chemical Society* **38**, 762 (1916).

- [23] H. Bässler, G. Schönherr, M. Abkowitz, and D. Pai, *Physical Review B* **26**, 3105 (1982).
- [24] H. Ishii, K. Sugiyama, E. Ito, and K. Seki, *Advanced materials* **11**, 605 (1999).
- [25] D. Cahen and A. Kahn, *Advanced Materials* **15**, 271 (2003).
- [26] N. Ueno, S. Kera, and K. Kanai, “Fundamental electronic structure of organic solids and their interfaces by photoemission spectroscopy and related methods”, in *The molecule–metal interface* (John Wiley & Sons, Ltd) Chap. 7, pp. 173–217.
- [27] N. Sato, K. Seki, and H. Inokuchi, *J. Chem. Soc., Faraday Trans. 2* **77**, 1621 (1981).
- [28] N. Ueno, *Science* **352**, 1395 (2016).
- [29] M. Schwarze, K. S. Schellhammer, K. Ortstein, J. Benduhn, C. Gaul, A. Hinderhofer, L. P. Toro, R. Scholz, J. Kublitski, S. Roland, et al., *Nature communications* **10**, 1 (2019).
- [30] Y. Uemura, S. A. Abd-Rahman, S. Yanagisawa, and H. Yoshida, *Phys. Rev. B* **102**, 125302 (2020).
- [31] M. Schwarze, W. Tress, B. Beyer, F. Gao, R. Scholz, C. Poelking, K. Ortstein, A. A. Günther, D. Kasemann, D. Andrienko, et al., *Science* **352**, 1446 (2016).
- [32] M. Knupfer, *Applied Physics A* **77**, 623 (2003).
- [33] H. Bronstein, C. B. Nielsen, B. C. Schroeder, and I. McCulloch, *Nature Reviews Chemistry* **4**, 66 (2020).
- [34] M. Schwoerer and H. C. Wolf, *Organische molekulare festkörper: einföhrung in die physik von pi-systemen* (John Wiley & Sons, 2012).
- [35] H. Peisert, M. Knupfer, T. Schwieger, G. Fuentes, D. Olligs, J. Fink, and T. Schmidt, *Journal of applied physics* **93**, 9683 (2003).
- [36] L. D. Landau, *Phys. Z. Sowjet.* **3**, 664 (1933).
- [37] A. Köhler and H. Bässler, *Electronic processes in organic semiconductors: an introduction* (John Wiley & Sons, 2015).
- [38] J. L. Bredas and G. B. Street, *Accounts of Chemical Research* **18**, 309 (1985).
- [39] O. Bubnova, Z. U. Khan, H. Wang, S. Braun, D. R. Evans, M. Fabretto, P. Hojati-Talemi, D. Dagnelund, J.-B. Arlin, Y. H. Geerts, et al., *Nature materials* **13**, 190 (2014).
- [40] S. Winkler, P. Amsalem, J. Frisch, M. Oehzelt, G. Heimel, and N. Koch, *Materials Horizons* **2**, 427 (2015).
- [41] G. Heimel, *ACS central science* **2**, 309 (2016).
- [42] R.-Q. Png, M. C. Ang, M.-H. Teo, K.-K. Choo, C. G. Tang, D. Belaineh, L.-L. Chua, and P. K. Ho, *Nature communications* **7**, 1 (2016).
- [43] C. K. Chiang, C. Fincher Jr, Y. W. Park, A. J. Heeger, H. Shirakawa, E. J. Louis, S. C. Gau, and A. G. MacDiarmid, *Physical review letters* **39**, 1098 (1977).
- [44] R. McNeill, R. Siudak, J. Wardlaw, and D. Weiss, *Australian Journal of Chemistry* **16**, 1056 (1963).

-
- [45] G. Parthasarathy, C. Shen, A. Kahn, and S. Forrest, *Journal of Applied Physics* **89**, 4986 (2001).
- [46] J. Kido and T. Matsumoto, *Applied Physics Letters* **73**, 2866 (1998).
- [47] C. R. Bridges and T. Baumgartner, *Journal of Physical Organic Chemistry* **33**, e4077 (2020).
- [48] I. Salzmann, G. Heimel, S. Duhm, M. Oehzelt, P. Pingel, B. M. George, A. Schnegg, K. Lips, R.-P. Blum, A. Vollmer, et al., *Physical Review Letters* **108**, 035502 (2012).
- [49] A. Mityashin, Y. Olivier, T. Van Regemorter, C. Rolin, S. Verlaak, N. G. Martinelli, D. Beljonne, J. Cornil, J. Genoe, and P. Heremans, *Advanced Materials* **24**, 1535 (2012).
- [50] M. L. Tietze, J. Benduhn, P. Pahner, B. Nell, M. Schwarze, H. Kleemann, M. Krammer, K. Zojer, K. Vandewal, and K. Leo, *Nature communications* **9**, 1 (2018).
- [51] M. Schwarze, C. Gaul, R. Scholz, F. Bussolotti, A. Hofacker, K. S. Schellhammer, B. Nell, B. D. Naab, Z. Bao, D. Spoltore, et al., *Nature materials* **18**, 242 (2019).
- [52] M. R. Bryce and L. C. Murphy, *Nature* **309**, 119 (1984).
- [53] T. Mori and T. Kawamoto, *Annual Reports Section "C" (Physical Chemistry)* **103**, 134 (2007).
- [54] G. Saito and Y. Yoshida, *Frontiers of organic conductors and superconductors* (Springer, 2011), pp. 67–126.
- [55] J. Ferraris, D. Cowan, V. t. Walatka, and J. Perlstein, *Journal of the American Chemical Society* **95**, 948 (1973).
- [56] R. Comes, S. Shapiro, G. Shirane, A. Garito, and A. Heeger, *Physical Review Letters* **35**, 1518 (1975).
- [57] F. Denoyer, F. Comès, A. Garito, and A. Heeger, *Physical Review Letters* **35**, 445 (1975).
- [58] K. Bechgaard, K. Carneiro, M. Olsen, F. B. Rasmussen, and C. S. Jacobsen, *Physical Review Letters* **46**, 852 (1981).
- [59] J. M. Williams, A. M. Kini, H. H. Wang, K. D. Carlson, U. Geiser, L. K. Montgomery, G. J. Pyrka, D. M. Watkins, and J. M. Kommers, *Inorganic Chemistry* **29**, 3272 (1990).
- [60] A. Hebard, M. Rosseinsky, R. Haddon, D. Murphy, S. Glarum, T. Palstra, A. Ramirez, and A. Karton, *Nature* **350**, 600 (1991).
- [61] A. Y. Ganin, Y. Takabayashi, Y. Z. Khimiyak, S. Margadonna, A. Tamai, M. J. Rosseinsky, and K. Prassides, *Nature materials* **7**, 367 (2008).
- [62] Y. Gao, *Materials Science and Engineering: R: Reports* **68**, 39 (2010).
- [63] S. Braun, W. R. Salaneck, and M. Fahlman, *Advanced Materials* **21**, 1450 (2009).
- [64] M. Oehzelt, K. Akaike, N. Koch, and G. Heimel, *Science advances* **1**, e1501127 (2015).
- [65] K. Akaike, *Japanese Journal of Applied Physics* **57**, 03EA03 (2018).

- [66] M. Fahlman, S. Fabiano, V. Gueskine, D. Simon, M. Berggren, and X. Crispin, *Nature Reviews Materials* **4**, 627 (2019).
- [67] N. Lang and W. Kohn, *Physical Review B* **3**, 1215 (1971).
- [68] G. Heimel, S. Duhm, I. Salzmann, A. Gerlach, A. Strozecka, J. Niederhausen, C. Bürker, T. Hosokai, I. Fernandez-Torrente, G. Schulze, et al., *Nature chemistry* **5**, 187 (2013).
- [69] L. Romaner, G. Heimel, J.-L. Brédas, A. Gerlach, F. Schreiber, R. L. Johnson, J. Zegenhagen, S. Duhm, N. Koch, and E. Zojer, *Physical review letters* **99**, 256801 (2007).
- [70] O. T. Hofmann, P. Rinke, M. Scheffler, and G. Heimel, *ACS nano* **9**, 5391 (2015).
- [71] N. Koch, A. Gerlach, S. Duhm, H. Glowatzki, G. Heimel, A. Vollmer, Y. Sakamoto, T. Suzuki, J. Zegenhagen, J. P. Rabe, et al., *Journal of the American Chemical Society* **130**, 7300 (2008).
- [72] E. Goiri, P. Borghetti, A. El-Sayed, J. E. Ortega, and D. G. de Oteyza, *Advanced Materials* **28**, 1340 (2016).
- [73] N. Koch, *Electronic structure of interfaces with conjugated organic materials*, 2012.
- [74] M. Oehzelt, N. Koch, and G. Heimel, *Nature communications* **5**, 1 (2014).
- [75] H. Y. Mao, F. Bussolotti, D.-C. Qi, R. Wang, S. Kera, N. Ueno, A. T. S. Wee, and W. Chen, *Organic Electronics* **12**, 534 (2011).
- [76] H. Vázquez, Y. Dappe, J. Ortega, and F. Flores, *The Journal of chemical physics* **126**, 144703 (2007).
- [77] F. Bussolotti, S. Kera, K. Kudo, A. Kahn, and N. Ueno, *Physical review letters* **110**, 267602 (2013).
- [78] H. Vázquez, F. Flores, and A. Kahn, *Organic Electronics* **8**, 241 (2007).
- [79] S. Zhong, J. Q. Zhong, H. Y. Mao, J. L. Zhang, J. D. Lin, and W. Chen, *Physical Chemistry Chemical Physics* **14**, 14127 (2012).
- [80] W. Chen, D. C. Qi, Y. L. Huang, H. Huang, Y. Z. Wang, S. Chen, X. Y. Gao, and A. T. S. Wee, *The Journal of Physical Chemistry C* **113**, 12832 (2009).
- [81] A. Opitz, A. Wilke, P. Amsalem, M. Oehzelt, R.-P. Blum, J. P. Rabe, T. Mizokuro, U. Hörmann, R. Hansson, E. Moons, et al., *Scientific reports* **6**, 1 (2016).
- [82] U. Hörmann, C. Lorch, A. Hinderhofer, A. Gerlach, M. Gruber, J. Kraus, B. Sykora, S. Grob, T. Linderl, A. Wilke, et al., *The Journal of Physical Chemistry C* **118**, 26462 (2014).
- [83] T. Hasegawa, S. Kagoshima, T. Mochida, S. Sugiura, and Y. Iwasa, *Solid state communications* **103**, 489 (1997).
- [84] M. Sing, U. Schwingenschlögl, R. Claessen, M. Dressel, and C. S. Jacobsen, *Physical Review B* **67**, 125402 (2003).
- [85] T. Mathis, K. Mattenberger, P. Moll, and B. Batlogg, *Applied Physics Letters* **101**, 023302 (2012).

- [86] B. Kattel, T. Wang, T. R. Kaffle, and W.-L. Chan, *Organic Electronics* **48**, 371 (2017).
- [87] J. I. Beltrán, F. Flores, J. I. Martínez, and J. Ortega, *The Journal of Physical Chemistry C* **117**, 3888 (2013).
- [88] M. L. Tietze, L. Burtone, M. Riede, B. Lüssem, and K. Leo, *Physical Review B* **86**, 035320 (2012).
- [89] H. Méndez, G. Heimel, A. Opitz, K. Sauer, P. Barkowski, M. Oehzelt, J. Soeda, T. Okamoto, J. Takeya, J.-B. Arlin, et al., *Angewandte Chemie* **125**, 7905 (2013).
- [90] K. Kanai, K. Akaike, K. Koyasu, K. Sakai, T. Nishi, Y. Kamizuru, T. Nishi, Y. Ouchi, and K. Seki, *Applied Physics A* **95**, 309 (2009).
- [91] P. Ru, E. Bi, Y. Zhang, Y. Wang, W. Kong, Y. Sha, W. Tang, P. Zhang, Y. Wu, W. Chen, et al., *Advanced Energy Materials* **10**, 1903487 (2020).
- [92] P. E. Schwenn, P. L. Burn, and B. J. Powell, *Organic Electronics* **12**, 394 (2011).
- [93] M. Toader, T. G. Gopakumar, P. Shukrynau, and M. Hietschold, *The Journal of Physical Chemistry C* **114**, 21548 (2010).
- [94] W. Gao and A. Kahn, *Applied Physics Letters* **79**, 4040 (2001).
- [95] P. Wellmann, M. Hofmann, O. Zeika, A. Werner, J. Birnstock, R. Meerheim, G. He, K. Walzer, M. Pfeiffer, and K. Leo, *Journal of the Society for Information Display* **13**, 393 (2005).
- [96] M. Elawad, L. Sun, G. T. Mola, Z. Yu, and E. A. A. Arbab, *Journal of Alloys and Compounds* **771**, 25 (2019).
- [97] L.-F. Ji, J.-X. Fan, S.-F. Zhang, and A.-M. Ren, *Physical Chemistry Chemical Physics* **20**, 3784 (2018).
- [98] H. Okamoto, H. Matsuzaki, T. Wakabayashi, Y. Takahashi, and T. Hasegawa, *Physical review letters* **98**, 037401 (2007).
- [99] P. K. Koech, A. B. Padmaperuma, L. Wang, J. S. Swensen, E. Polikarpov, J. T. Darsell, J. E. Rainbolt, and D. J. Gaspar, *Chemistry of Materials* **22**, 3926 (2010).
- [100] V. Vijayakumar, P. Durand, H. Zeng, V. Untilova, L. Herrmann, P. Algayer, N. Leclerc, and M. Brinkmann, *Journal of Materials Chemistry C* **8**, 16470 (2020).
- [101] B. Lüssem, M. L. Tietze, H. Kleemann, C. Hoßbach, J. W. Bartha, A. Zakhidov, and K. Leo, *Nature communications* **4**, 1 (2013).
- [102] C. Murawski, C. Fuchs, S. Hofmann, K. Leo, and M. C. Gather, *Applied Physics Letters* **105**, 145_1 (2014).
- [103] F. Zu, P. Amsalem, M. Ralaiarisoa, T. Schultz, R. Schlesinger, and N. Koch, *ACS applied materials & interfaces* **9**, 41546 (2017).
- [104] C. Christodoulou, A. Giannakopoulos, G. Ligorio, M. Oehzelt, M. Timpel, J. Niederhausen, L. Pasquali, A. Giglia, K. Parvez, K. Müllen, et al., *ACS applied materials & interfaces* **7**, 19134 (2015).
- [105] S. Park, T. Schultz, X. Xu, B. Wegner, A. Aljarb, A. Han, L.-J. Li, V. C. Tung, P. Amsalem, and N. Koch, *Communications Physics* **2**, 1 (2019).

- [106] R. Mitsuhashi, Y. Suzuki, Y. Yamanari, H. Mitamura, T. Kambe, N. Ikeda, H. Okamoto, A. Fujiwara, M. Yamaji, N. Kawasaki, et al., *Nature* **464**, 76 (2010).
- [107] X. Wang, R. Liu, Z. Gui, Y. Xie, Y. Yan, J. Ying, X. Luo, and X. Chen, *Nature communications* **2**, 1 (2011).
- [108] M. Xue, T. Cao, D. Wang, Y. Wu, H. Yang, X. Dong, J. He, F. Li, and G. Chen, *Scientific reports* **2**, 1 (2012).
- [109] S. Heguri, M. Kobayashi, and K. Tanigaki, *Physical Review B* **92**, 014502 (2015).
- [110] J. E. Anthony, *Chemical reviews* **106**, 5028 (2006).
- [111] D. Lubert-Perquel, E. Salvadori, M. Dyson, P. N. Stavrinou, R. Montis, H. Nagashima, Y. Kobori, S. Heutz, and C. W. Kay, *Nature communications* **9**, 1 (2018).
- [112] J. Meiss, A. Merten, M. Hein, C. Schuenemann, S. Schäfer, M. Tietze, C. Urich, M. Pfeiffer, K. Leo, and M. Riede, *Advanced Functional Materials* **22**, 405 (2012).
- [113] O. A. Melville, B. H. Lessard, and T. P. Bender, *ACS applied materials & interfaces* **7**, 13105 (2015).
- [114] T. Ishiguro, K. Yamaji, and G. Saito, “Organic conductors”, in *Organic superconductors* (Springer, 1998), pp. 15–43.
- [115] A. M. Kini, U. Geiser, H. H. Wang, K. D. Carlson, J. M. Williams, W. Kwok, K. Vandervoort, J. E. Thompson, and D. L. Stupka, *Inorganic Chemistry* **29**, 2555 (1990).
- [116] F. Schwarz, G. Kastlunger, F. Lissel, C. Egler-Lucas, S. N. Semenov, K. Venkatesan, H. Berke, R. Stadler, and E. Lörtscher, *Nature nanotechnology* **11**, 170 (2016).
- [117] J. Drechsel, B. Männig, D. Gebeyehu, M. Pfeiffer, K. Leo, and H. Hoppe, *Organic electronics* **5**, 175 (2004).
- [118] A. A. Popov, S. Yang, and L. Dunsch, *Chemical reviews* **113**, 5989 (2013).
- [119] H. Hertz, *Annalen der Physik* **267**, 983 (1887).
- [120] W. Hallwachs, *Annalen der Physik* **269**, 301 (1888).
- [121] A. Einstein, *Annalen der physik* **4** (1905).
- [122] K. Siegbahn, *The Nobel Foundation* (1981).
- [123] W. Demtröder, *Experimentalphysik 3: atome, moleküle und festkörper* (Springer-Verlag, 2010).
- [124] S. Hüfner, *Photoelectron spectroscopy, vol. 82 in solid-state sciences*, 1995.
- [125] F. Reinert and S. Hüfner, *New Journal of Physics* **7**, 97 (2005).
- [126] S. Suga and A. Sekiyama, *Photoelectron spectroscopy* (Springer, 2016).
- [127] M. Angst, T. Brückel, D. Richter, and R. Zorn, *Scattering methods for condensed matter research*, PreJuSER-136382 (Streumethoden, 2012).
- [128] B. Mahns, “Elektronische eigenschaften dotierter polyzyklischer aromatischer kohlenwasserstoffe”, dissertation (2015).
- [129] J. Braun, *Reports on Progress in Physics* **59**, 1267 (1996).

-
- [130] C. N. Berglund and W. E. Spicer, *Physical Review* **136**, A1030 (1964).
- [131] M. Seah and W. Dench, *Surface And Interface Analysis* **1**, 2 (1979).
- [132] F. R uckerl, “Photoemission spectroscopy at organic semiconductor systems”, dissertation (Technische Universit at Dresden, 2017).
- [133] A. Damascelli, *Physica Scripta* **2004**, 61 (2004).
- [134] S. Tougaard, *Physical Review B* **34**, 6779 (1986).
- [135] D. A. Shirley, *Physical Review B* **5**, 4709 (1972).
- [136] OriginLab Corporation, *Origin*, version 2021b.
- [137] S. Lindner, “Charge transfer at phthalocyanine interfaces”, dissertation (Technische Universit at Dresden, 2014).
- [138] U. Gelius, E. Basilier, S. Svensson, T. Bergmark, and K. Siegbahn, *Journal of Electron Spectroscopy and Related Phenomena* **2**, 405 (1973).
- [139] J. Chastain and R. C. King Jr, Perkin-Elmer, USA, 261 (1992).
- [140] M. Knupfer and H. Peisert, *Physica Status solidi (a)* **201**, 1055 (2004).
- [141] SPECS GmbH, *Manual for the phoibos hemispherical energy analyzer series* (Voltastrasse 5 D-13355 Berlin, GERMANY, 2008).
- [142] M. Koshino, H. Kurata, and S. Isoda, *Journal of electron spectroscopy and related phenomena* **135**, 191 (2004).
- [143] P. Borghetti, A. Sarasola, N. Merino-D iez, G. Vasseur, L. Floreano, J. Lobo-Checa, A. Arnau, D. G. de Oteyza, and J. E. Ortega, *The Journal of Physical Chemistry C* **121**, 28412 (2017).
- [144] R. Kuhrt, P.-Y. Ho, M. Hantusch, F. Lissel, O. Blacque, M. Knupfer, and B. B uchner, *RSC Advances* **10**, 43242 (2020).
- [145] N. Koch, S. Duhm, J. P. Rabe, A. Vollmer, and R. L. Johnson, *Physical review letters* **95**, 237601 (2005).
- [146] R. Kuhrt, M. Hantusch, M. Knupfer, and B. B uchner, *Surface and Interface Analysis* **52**, 953 (2020).
- [147] O. McDonald, A. Cafolla, D. Carty, G. Sheerin, and G. Hughes, *Surface science* **600**, 3217 (2006).
- [148] M. Eremtchenko, R. Temirov, D. Bauer, J. Schaefer, and F. Tautz, *Physical Review B* **72**, 115430 (2005).
- [149] G. M. Rangger, O. T. Hofmann, L. Romaner, G. Heimel, B. Br oker, R.-P. Blum, R. L. Johnson, N. Koch, and E. Zojer, *Physical Review B* **79**, 165306 (2009).
- [150] R. Otero, R. Miranda, and J. M. Gallego, *ACS omega* **4**, 16906 (2019).
- [151] L. Sch ottner, S. Erker, R. Schlesinger, N. Koch, A. Nefedov, O. Hofmann, and C. W oll, *The Journal of Physical Chemistry C* **124**, 4511 (2020).
- [152] H. F. Haneef, A. M. Zeidell, and O. D. Jurchescu, *Journal of Materials Chemistry C* **8**, 759 (2020).

- [153] B. S. Bhardwaj, T. Sugiyama, N. Namba, T. Umakoshi, T. Uemura, T. Sekitani, and P. Verma, *Scientific reports* **9**, 1 (2019).
- [154] H. Kleemann, C. Schuenemann, A. A. Zakhidov, M. Riede, B. Lüssem, and K. Leo, *Organic Electronics* **13**, 58 (2012).
- [155] E. Guo, S. Xing, F. Dollinger, R. Hübner, S.-J. Wang, Z. Wu, K. Leo, and H. Kleemann, *Nature Electronics* **4**, 588 (2021).
- [156] S. Yoshimoto, K. Kameshima, T. Koitaya, Y. Harada, K. Mukai, and J. Yoshinobu, *Organic Electronics* **15**, 356 (2014).
- [157] B. Mahns, F. Roth, A. König, M. Grobosch, M. Knupfer, and T. Hahn, *PHYSICAL REVIEW B* **86**, 35209 (2012).
- [158] M. Hantusch, R. Kuhrt, and M. Knupfer, *The Journal of Physical Chemistry C* **124**, 2961 (2020).
- [159] F. Otto, T. Huempfer, M. Schaal, C. Udhardt, L. Vorbrink, B. Schroeter, R. Forker, and T. Fritz, *The Journal of Physical Chemistry C* **122**, 8348 (2018).
- [160] N. Watkins and Y. Gao, *Journal of applied physics* **94**, 5782 (2003).
- [161] Y. Karpov, T. Erdmann, M. Stamm, U. Lappan, O. Guskova, M. Malanin, I. Raguzin, T. Beryozkina, V. Bakulev, F. Günther, et al., *Macromolecules* **50**, 914 (2017).
- [162] D. Waas, F. Rückerl, M. Knupfer, and B. Büchner, *Beilstein Journal of Nanotechnology* **8**, 927 (2017).
- [163] W. Chen, D.-C. Qi, H. Huang, X. Gao, and A. T. Wee, *Advanced Functional Materials* **21**, 410 (2011).
- [164] I. Salzmann, S. Duhm, G. Heimel, M. Oehzelt, R. Kniprath, R. L. Johnson, J. P. Rabe, and N. Koch, *Journal of the American Chemical Society* **130**, 12870 (2008).
- [165] R. Warren, A. Privitera, P. Kaienburg, A. E. Lauritzen, O. Thimm, J. Nelson, and M. K. Riede, *Nature communications* **10**, 1 (2019).
- [166] N. Koch, C. Chan, A. Kahn, and J. Schwartz, *Physical Review B* **67**, 195330 (2003).
- [167] A. Ruff, M. Sing, R. Claessen, H. Lee, M. Tomić, H. O. Jeschke, and R. Valentí, *Physical review letters* **110**, 216403 (2013).
- [168] D. C. Milan, A. Vezzoli, I. J. Planje, and P. J. Low, *Dalton Transactions* **47**, 14125 (2018).
- [169] K. E. Watts, B. Neelamraju, E. L. Ratcliff, and J. E. Pemberton, *Chemistry of Materials* **31**, 6986 (2019).
- [170] F. Zhang and A. Kahn, *Advanced Functional Materials* **28**, 1703780 (2018).
- [171] R. P. Shibaeva and E. B. Yagubskii, *Chemical reviews* **104**, 5347 (2004).
- [172] R. Kuhrt, M. Hantusch, B. Buechner, and M. Knupfer, *The Journal of Physical Chemistry C* **125**, 18961 (2021).
- [173] E. Demiralp and W. A. Goddard III, *The Journal of Physical Chemistry* **98**, 9781 (1994).

- [174] J. Shumway, S. Chattopadhyay, and S. Satpathy, *Physical Review B* **53**, 6677 (1996).
- [175] K. Mukai and J. Yoshinobu, *Journal of Electron Spectroscopy and Related Phenomena* **174**, 55 (2009).
- [176] H. Schamoni, M. Hetzl, T. Hoffmann, K. Stoiber, S. Matich, and M. Stutzmann, *Materials Research Express* **6**, 025903 (2018).
- [177] W. Gao and A. Kahn, *Journal of Applied Physics* **94**, 359 (2003).
- [178] S. Duhm, I. Salzmann, B. Bröker, H. Glowatzki, R. L. Johnson, and N. Koch, *Applied physics letters* **95**, 223 (2009).
- [179] J. Li, C. W. Rochester, I. E. Jacobs, S. Friedrich, P. Stroeve, M. Riede, and A. J. Moulé, *ACS applied materials & interfaces* **7**, 28420 (2015).
- [180] I. N. Stranski and L. Krastanow, *Monatshefte für Chemie und verwandte Teile anderer Wissenschaften* **71**, 351 (1937).
- [181] K. Akaike, N. Koch, G. Heimel, and M. Oehzelt, *Advanced Materials Interfaces* **2**, 1500232 (2015).
- [182] S. Lindner, M. Knupfer, R. Friedrich, T. Hahn, and J. Kortus, *Physical review letters* **109**, 027601 (2012).
- [183] Y. Krupskaya, F. Rückerl, M. Knupfer, and A. F. Morpurgo, *Advanced Materials Interfaces* **3**, 1500863 (2016).
- [184] F. Rückerl, D. Waas, B. Büchner, and M. Knupfer, *Journal of Electron Spectroscopy and Related Phenomena* **215**, 1 (2017).
- [185] F. Petraki, H. Peisert, J. Uihlein, U. Aygül, and T. Chassé, *Beilstein journal of nanotechnology* **5**, 524 (2014).
- [186] S. Lindner, U. Treske, M. Grobosch, and M. Knupfer, *Applied Physics A* **105**, 921 (2011).
- [187] T. Schwieger, H. Peisert, M. Golden, M. Knupfer, and J. Fink, *Physical Review B* **66**, 155207 (2002).
- [188] L. Ottaviano, S. Di Nardo, L. Lozzi, M. Passacantando, P. Picozzi, and S. Santucci, *Surface science* **373**, 318 (1997).
- [189] S. Lindner, U. Treske, and M. Knupfer, *Applied surface science* **267**, 62 (2013).
- [190] T. Lukasczyk, K. Flechtner, L. R. Merte, N. Jux, F. Maier, J. M. Gottfried, and H.-P. Steinrück, *The Journal of Physical Chemistry C* **111**, 3090 (2007).
- [191] F. Petraki, H. Peisert, F. Latteyer, U. Aygul, A. Vollmer, and T. Chassé, *The Journal of Physical Chemistry C* **115**, 21334 (2011).
- [192] A. Belser, K. Greulich, P. Grüninger, R. Karstens, R. Ovsyannikov, E. Giangrisostomi, P. Nagel, M. Merz, S. Schuppler, T. Chassé, et al., *The Journal of Physical Chemistry C* **125**, 8803 (2021).
- [193] M. Pörtner, Y. Wei, A. Riss, K. Seufert, M. Garnica, J. V. Barth, A. P. Seitsonen, L. Diekhöner, and W. Auwärter, *Advanced Materials Interfaces* **7**, 2000080 (2020).
- [194] D. Xiang, X. Wang, C. Jia, T. Lee, and X. Guo, *Chemical reviews* **116**, 4318 (2016).

- [195] Y. Wang, C. Yan, S.-Y. Cheng, Z.-Q. Xu, X. Sun, Y.-H. Xu, J.-J. Chen, Z. Jiang, K. Liang, and Z.-S. Feng, *Advanced Functional Materials* **29**, 1902579 (2019).
- [196] T. Li, V. K. Bandari, M. Hantusch, J. Xin, R. Kuhrt, R. Ravishankar, L. Xu, J. Zhang, M. Knupfer, F. Zhu, et al., *Nature communications* **11**, 1 (2020).
- [197] S. Steudel, K. Myny, V. Arkhipov, C. Deibel, S. De Vusser, J. Genoe, and P. Heremans, *Nature materials* **4**, 597 (2005).
- [198] J. Trasobares, D. Vuillaume, D. Théron, and N. Clément, *Nature communications* **7**, 1 (2016).
- [199] S. F. Tan, “Quantum plasmon resonances controlled by molecular tunnel junction”, in *Molecular electronic control over tunneling charge transfer plasmons modes* (Springer, 2018), pp. 51–67.
- [200] J. H. Cho, D. H. Kim, Y. Jang, W. H. Lee, K. Ihm, J.-H. Han, S. Chung, and K. Cho, *Applied Physics Letters* **89**, 132101 (2006).
- [201] A. R. Jalil, H. Chang, V. K. Bandari, P. Robaschik, J. Zhang, P. F. Siles, G. Li, D. Bürger, D. Grimm, X. Liu, et al., *Advanced Materials* **28**, 2971 (2016).
- [202] V. K. Bandari, L. Varadharajan, L. Xu, A. R. Jalil, M. Devarajulu, P. F. Siles, F. Zhu, and O. G. Schmidt, *Beilstein journal of nanotechnology* **8**, 1277 (2017).
- [203] C. C. Bof Bufon, C. Vervacke, D. J. Thurmer, M. Fronk, G. Salvan, S. Lindner, M. Knupfer, D. R. Zahn, and O. G. Schmidt, *The Journal of Physical Chemistry C* **118**, 7272 (2014).
- [204] R. Gould, *Coordination Chemistry Reviews* **156**, 237 (1996).
- [205] A. Babel, J. D. Wind, and S. A. Jenekhe, *Advanced Functional Materials* **14**, 891 (2004).
- [206] Y.-S. Hsiao, W.-T. Whang, S.-C. Suen, J.-Y. Shiu, and C.-P. Chen, *Nanotechnology* **19**, 415603 (2008).
- [207] C.-m. Kang, J. Wade, S. Yun, J. Lim, H. Cho, J. Roh, H. Lee, S. Nam, D. D. Bradley, J.-S. Kim, et al., *Advanced Electronic Materials* **2**, 1500282 (2016).
- [208] K. Lau, J. Tang, H. Sun, C. Lee, S. Lee, and D. Yan, *Applied physics letters* **88**, 173513 (2006).
- [209] P. F. Siles, T. Hahn, G. Salvan, M. Knupfer, F. Zhu, D. Zahn, and O. Schmidt, *Nanoscale* **8**, 8607 (2016).
- [210] J. M. Mativetsky, H. Wang, S. S. Lee, L. Whittaker-Brooks, and Y.-L. Loo, *Chemical Communications* **50**, 5319 (2014).
- [211] Z. Zhang and J. T. Yates Jr, *Chemical reviews* **112**, 5520 (2012).
- [212] S. M. Sze, Y. Li, and K. K. Ng, *Physics of semiconductor devices* (John wiley & sons, 2021).
- [213] M. A. Lampert, *Physical Review* **103**, 1648 (1956).
- [214] A. Carbone, B. Kotowska, and D. Kotowski, *Physical review letters* **95**, 236601 (2005).

- [215] G. Xu, N. Gao, C. Lu, W. Wang, Z. Ji, C. Bi, Z. Han, N. Lu, G. Yang, Y. Li, et al., *Advanced Electronic Materials* **4**, 1700493 (2018).
- [216] S. Munjal and N. Khare, *Scientific reports* **7**, 1 (2017).

Publication list

- M. Hantusch, R. Kuhrt and M. Knupfer, "*Photoelectron Spectroscopy on Polycyclic Hydrocarbon-F₆TCNNQ Interfaces*", The Journal of Physical Chemistry C 124, 2961 (2020)
- R. Kuhrt, M. Hantusch, M. Knupfer and B. Büchner, "*Charge transfer characteristics of F₆TCNNQ-gold interface*", Surface and Interface Analysis 52, 953 (2020)
- R. Kuhrt, PY Ho, M. Hantusch, F. Lissel, O. Blacque, M. Knupfer and B. Büchner, "*Synthesis and charge transfer characteristics of a ruthenium-acetylide complex*", RSC Advances 10, 43242 (2020)
- T. Li, V. K. Bandari, M. Hantusch, J. Xin, R. Kuhrt, R. Ravishankar, L. Xu, J. Zhang, M. Knupfer, F. Zhu, D. Yan and OG Schmidt, "*Integrated molecular diode as 10 MHz half-wave rectifier based on an organic nanostructure heterojunction*", Nature communications 11, 1 (2020)
- R. Kuhrt, M. Hantusch, B. Buechner and M. Knupfer, "*Photoemission Study of Charge Transfer between ET (BEDT-TTF) and Acceptors F₆TCNNQ and F₂TCNQ*", The Journal of Physical Chemistry C 125, 18961 (2021).

Danksagung

Bedanken möchte ich mich zunächst beim IFW Dresden und Prof. Bernd Büchner für die Möglichkeit in diesem interessanten wissenschaftlichem Umfeld zu arbeiten.

Prof. Martin Knupfer danke ich für die sehr gute fachliche Betreuung, die ansteckende Freude am wissenschaftlichen Arbeiten und die immer offene Bürotür.

Bei Dr. Martin Hantusch bedanke ich mich für die Einführung in die Bedienung der Spektrometer, die technische Unterstützung und die vielen guten Diskussionen über Messungen und Ergebnisse.

Dr. Roland Hübel, Marco Naumann und Frauke Thunig danke ich für die große Hilfsbereitschaft bei technischen Problemen im Labor.

Bedanken möchte ich mich auch bei den anderen Mitgliedern unserer Arbeitsgruppe, Louis Doctor und Lukas Graf, für die alltäglichen Mensabesuche und die immer gute Stimmung im Büro.

Erklärung

Hiermit erkläre ich, dass ich die vorliegende Arbeit ohne unzulässige Hilfe Dritter verfasst habe und alle verwendeten Quellen als solche gekennzeichnet habe.

Die Arbeit wurde bisher weder im Inland noch im Ausland in gleicher oder ähnlicher Form einer anderen Prüfungsbehörde vorgelegt.

Die Dissertation wurde am Leibniz-Institut für Festkörper- und Werkstoffforschung (IFW) in Dresden unter der wissenschaftlichen Betreuung von Prof. Martin Knupfer und Prof. Bernd Büchner angefertigt.

Ich erkenne hiermit die Promotionsordnung der Fakultät Mathematik und Naturwissenschaften der Technischen Universität Dresden vom 23.02.2011 an.

Ort, Datum

Unterschrift